Development and Properties Evaluation of Al_2O_3 and ZTA porous Ceramics produced by different Techniques

A dissertation work

submitted in partial fulfilment of the requirements

for the award of the degree of

DOCTOR OF PHILOSOPHY

in

METALLURGICAL AND MATERIALS ENGINEERING

by

VEMOORI RAJU

(Roll No.716036)

Under the guidance of

Dr. Asit Kumar Khanra
Associate Professor
Department of Metallurgical and Materials Engineering
National Institute of Technology Warangal.

Dr. Roy Johnson
Scientist-G & Associate Director
ARCI, Hyderabad
Telangana state, India

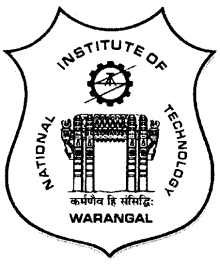

DEPARTMENT OF METALLURGICAL AND MATERIALS ENGINEERING

NATIONAL INSTITUTE OF TECHNOLOGY WARANGAL

SEPTEMBER – 2021

Dedicated to

My Family and Friends

Thesis Approval for Ph.D.

The thesis entitled **"Development and Properties Evaluation of Al_2O_3 and ZTA porous Ceramics Produced by different Techniques"** is submitted by **Mr. Raju Vemoori (Roll No.716036)** is approved for the degree of **Doctor of Philosophy** in Metallurgical and Materials Engineering.

Examiner

_____

Supervisors

_____

_____

Chairman

_____

Date: _____

DEPARTMENT OF METALLURGICAL AND MATERIALS ENGINEERING
NATIONAL INSTITUTE OF TECHNOLOGY
WARANGAL - 506 004 (T.S) INDIA

CERTIFICATE

This is to certify that the work presented in the thesis entitled **"Development and Properties Evaluation of Al_2O_3 and ZTA porous Ceramics Produced by different Techniques"** which is being submitted by **Mr. Raju Vemoori (Roll No.716036)** to the National Institute of Technology Warangal in partial fulfilment of the requirements for the award of the degree of **Doctor of Philosophy** in **Metallurgical and Materials Engineering** is a bonafide work carried out under my supervision**.** To the best of our knowledge, the work incorporated in this thesis has not been submitted to any other university or institute for the award of any other degree or diploma.

Dr. Asit Kumar Khanra
Associate Professor
Department of Metallurgical and Materials Engineering
National Institute of Technology Warangal.

Dr. Roy Johnson
Scientist-G & Associate Director
ARCI, Hyderabad
Telangana state, India

DECLARATION

This is to certify that the work presented in the thesis entitled **"Development and Properties Evaluation of Al_2O_3 and ZTA porous Ceramics Produced by different Techniques"** is a bonafide work done by me under the supervision of **Dr. Asit Kumar Khanra,** NITW **and Dr. Roy Johnson,** ARCI and was not submitted elsewhere for the award of any degree. I declare that this written submission represents my ideas in my own words and where others' ideas or words have been included, I have adequately cited and referenced the original sources. I also declare that I have adhered to all principles of academic honesty and integrity and have not misrepresented or fabricated or falsified any idea/data/fact/source in my submission. I understand that any violation of the above will be a cause for disciplinary action by the Institute and can also evoke penal action from the sources which have thus not been properly cited or from whom proper permission has not been taken when needed.

(Raju Vemoori)

Acknowledgements

I take this opportunity to express my deep sense of gratitude and heartfelt thanks to my research supervisors **Dr. Asit Kumar Khanra**, Associate professor, Department of Metallurgical and Materials Engineering, National Institute of Technology, Warangal and **Dr. Roy Johnson,** Scientist-G & Associate Director, ARCI Hyderabad for his wholehearted support, encouragement, guidance and patience during the research work. Without his untiring mentorship, constant inspiration, valuable discussions and suggestions, this thesis wouldn't have been possible. It was indeed a great honor and privilege to work under his supervision.

I am grateful to **Prof. N.V. Ramana Rao**, Director, NIT Warangal; **Prof. T. Srinivasa Rao,** former Director, NIT Warangal for giving me an opportunity to carry out research work in the institute.

My sincere thanks and appreciation to the Doctoral Scrutiny Committee members, **Dr. Asit Kumar Khanra** (Chairman & Head of the Department), **Dr. Brahma Raju Golla** (Assistant professor), **Dr. Ajoy kumar Panday** (Assistant professor), **Dr. V. Sridevi** (Assistant professor) Department of Metallurgical and Materials Engineering, and **Dr. M. J. Davidson** (Associate professor), Department of Mechanical Engineering, NIT Warangal for their helpful suggestions, remarks and periodical review of my research progress.

I am thankful to **Prof. N. Narasaiah**, former Head of the Department, for his continuous encouragement, valuable advice and support. I would also like to express my gratefulness to **Prof. M. K. Mohan**, **Dr. R. Arockia Kumar**, **Dr. C. Vanitha,** for their help in various ways during the research work. I sincerely acknowledge the financial support provided by the institute during the entire period of doctoral research study.

I thank technical staff **Miss. G. Ramya**, **Mr. G. Srinivasulu** for helping me to carry out X-ray diffraction and Scanning Electron Microscopy analysis**.** I also thank **Mr. G. Savvaiah**, Mechanic A grade (Retired) and **Mr. K. Balaswamy**, Mechanic A grade (Retired), **Mr. Fayaz**, **Mr. Prasad** and other technical and office staff of Metallurgical and Materials Engineering Department, NIT Warangal for their help during this research work.

I extend my sincere thanks to present and past lab mates, **Dr. K. Sai Mahesh Yadav**, **Mr. Katti Bharath**, **Mr. K. Rajesh**, **Mr. V. Ganesh, Mr. P. Raju** and **Miss. Shaik Mubina** for their assistance in experiments.

I also wish to thank all my friends, especially to **Dr. Rangadhara Chary Varayogi, Dr. Banda Mahesh, Dr. Shiva Bejugama, Dr. Prakash**, **Dr. Bheekya Naik**, **Mrs. Sony Priya, Mrs. Sravanthi Boda, Mr. Anvesh Turaga, Dr. Phanidra, Mr. C. Ravikanth Reddy**, **Mr. Venkateswara Reddy**, **Mr. K. Venkata Ashish Srivatsav**, **Mr. Siva Kumar Reddy**, **Mr. Shaik Mahammad Ali**, **Mr. T. Sravan, Mr. Vidhish Naik, Mr. Puli Anil Kumar, Mr. Vamshi** and for their valuable assistance and support.

Finally, I express my profound gratitude to my grandparents, my father **Sri. V. Yakub,** mother **Smt. Laxmi, brother Mr. Ravi kumar, spouse Mrs. Vineetha, daughter Meghana Raj,** mother-in-law Mrs. **K.Vijaya manohara**, father-in-law **Sri. K. Laxmaiah** and other family members for their patience, understanding, love, support and encouragement.

(RAJU VEMOORI)

September 2021

List of Abbreviations

YSZ – Yttria Stabilized Zirconia

3Y-TZP – 3 mol.% Yttria stabilized Tetragonal Zirconia Polycrystal

wt.% - Weight percent

vol.% - Volume percent

XRD – X-ray Diffraction

ICSD – Inorganic Crystal Structure Database

SEM – Scanning Electron Microscope

EDS – Energy Dispersion Spectroscopy

SE – Secondary Electrons

BSE – Back Scattered Electrons

nm – Nano meters

PSZ – Partially Stabilized Zirconia

FSZ – Fully Stabilized Zirconia

TZP – Tetragonal Zirconia Polycrystals

MPa – Mega Pascal

PVA – Polyvinyl alcohol

a.u. – Arbitrary units

KV – Kilo volts

mA – Milli amps

ASTM – American Society for Testing and Materials

ISO – International Organization for Standardization

List of Symbols

T – Tetragonal zirconia

M – Monoclinic zirconia

μ – Coefficient of friction

θ – Diffraction angle

d – Interplanar spacing

λ – Wave length

Å – Angstrom

°C – Degree celsius

ρ - Density

ϕ – Diameter

E – Youngs Modulus

P – Load

N – Newton

μm – Micro meter

Abstract

In recent years, porous ceramics have been widely explored for a wide range of applications due to their unique combination of thermal, structural and mechanical properties. However, these structures have not been adequately studied for their energy absorption properties due to their inherent brittleness. Several fabrication methods have also been developed during the last decades to control porosity, pore size distribution and pore interconnectivity in porous ceramics. In the present study, alumina (Al_2O_3) and zirconia toughened alumina (ZTA) ceramic foams were fabricated by three different methods i.e. sponge replication technique, thermoforming method, and sacrificial phase template (space holder). An attempt has been made to modify the brittle nature of ceramic foams by encapsulation, infiltration with polymers and metal (aluminium).

Al_2O_3 and ZTA foams with 10, 20 and 30 Pores Per Linear Inch (PPI) were initially prepared using a polymeric sponge replication technique (porosity <40%). Subsequently, foams were infiltrated and encapsulated with polymer and molten aluminium to make a composite and coated with nickel (Ni) by an electrolytic process. All the samples were subjected to the characterization of cellular and mechanical properties. 10 PPI infiltrated foams showing a significant increase in specific compressive strength and specific impact energy (SIE) were compared to bare and encapsulated foams.

Ni coating substantially enhanced compressive strength under static conditions for all foams irrespective of their pore density. An increase of 19 times was noticed for 10 PPI foams and around 14-15 times of enhancement was observed with 20 and 30 PPI foams. Plateau stress (σpl)**,** energy absorption density (EAD), densification strain (ε_{cd}), and energy absorption efficiency (EAE) were estimated and evaluated on a comparison basis. Under the dynamic impact, the maximum energy absorption property was 9 times that of bare foams. The introduction of metallic coating on cellular ceramics structures that enhance compressive strength and energy absorption properties will be useful for various applications.

Thermo- foaming method was used to fabricate Al_2O_3 and ZTA open-cell foam with porosity above 85% with a solid strut.

Al_2O_3 and ZTA foams (porosity >80%) were fabricated using a thermo-foaming method using varying powder to sucrose weight ratios. All the fabricated foams were characterized for their compressive strength, bending strength, and fracture toughness under static loading conditions. The compressive strength increases with an increase in a weight ratio from 0.4 to 1.2. The maximum compressive strength values were found to be 1.9 MPa, and 1.8 MPa for alumina

and zirconia toughened alumina foams, respectively. Further increase in powder to sucrose weight ratio led to a decrease in the compressive strength due to partial collapse of the cell walls during the foaming process. The 3-point bend test results revealed an improvement of bending strength and fracture toughness values of zirconia toughened alumina foams compared to alumina foam, which can be attributed to the transformation toughening mechanism.

Al_2O_3 and ZTA closed-cell foams (Porosity<70%) were fabricated through the space holder technique. Al_2O_3 and ZTA samples with varying porosity of 20% to 70% were investigated by control of porosity and micropore size. The micropore sizes of 10µm to 40µm can be easily fabricated by controlling the size of polystyrene beads. The samples with smaller micropores show higher compressive strength than those with larger micropores. Al_2O_3 foams showed higher compressive values compared to ZTA foams. Foams with 10µm micropores sample have higher compressive strength values when compared to 20µm and 40µm micropores samples. The compressive strength values obtained at 20Vol% and 80Vol% were 720MPa and 20MPa, respectively.

A theoretical model was developed and validated with experimental data to predict the properties of open-cell Al_2O_3 foam. The mechanical properties such as compressive strength and Young's modulus depend on Al_2O_3 foams' pore size and porosity. However, the strut thickness plays a role in the foams' strength. Al_2O_3 foam is collapsed layer-by-layer and the stress is highly concentrated at weak struts. The experimental results are divided into strut bending and slight densification categories. Finally, the numerical simulation results were slightly higher than the experimental results; however, the failure point matched at 0.0611 strain.

Keywords: Al_2O_3, ZTA, Porous structures, Foams, Pores per linear inch (PPI), Infiltration, Encapsulation, Compressive strength.

Index

LIST OF FIGURES

LIST OF TABLES

Chapter-1

Introduction

1.1 Introduction to ceramics

Ceramics are a class of materials with a long history and formed initially from natural materials such as clay and other aluminas. Humans have used ceramics for making utensils and artworks for thousands of years. Ceramics were found to be used before 5000 BC [1]. Ceramics are broadly classified into traditional ceramics and advanced ceramics. Traditional ceramics are clay-based; domestic wares, art objects, and building parts are examples of clay-based ceramics. The following process usually prepares ceramics: mixing of constituent powders with water or binder, pressing of the powders to form the desired shape, pre-firing for binder removal, and sintering at elevated temperature for full densification. The main drawback of these traditional ceramics is that they are very brittle, so attention has been paid to other advanced ceramics materials. Advanced ceramics are different from traditional ceramics. They are not generally clay-based; instead, they are made up of various oxides or non-oxides (Metal oxides, borides, nitrides, carbides, and silicates). As a result, ceramics used throughout the industry in technical applications require extreme hardness and stability of temperature [2].

1.1.1 Alumina ceramics

Alumina or aluminium oxide (Al_2O_3) is one of the most investigated ceramic materials due to the properties of tolerance to corrosion and high-temperature refractory design [3]. Alumina grades can be classified as 90% to 97% alumina purity and 98 % to 99.95% alumina purity. Alumina with a purity range of 90% to 97% is ideal for metallization (metal deposition that enables brazing) due to the wide grain structure. With a purity level of 98% to 99.95%, alumina is a typical range for isostatically pressed types, with extruded formulations and accessible at low prices. Alumina has various phases, such as alpha (α) phase, gamma(γ) phase, and beta (β) phase. α -Alumina is the most thermally stable form of alumina oxide, while other phases of alumina shift at a specific temperature. For example, at a temperature of 1000 °C, the γ -alumina-phase is converted to α -alumina phase. McColm (1983) stated that α -alumina is present in the corundum structure. As presented in Fig 1.1, it has a hexagonal shape and two alumina molecules per unit. With aluminium above and below the middle of the triangle, three oxygens shape an equilateral triangle. Each corner of a cube is placed in one of these classes, while another is placed at the cube's middle.

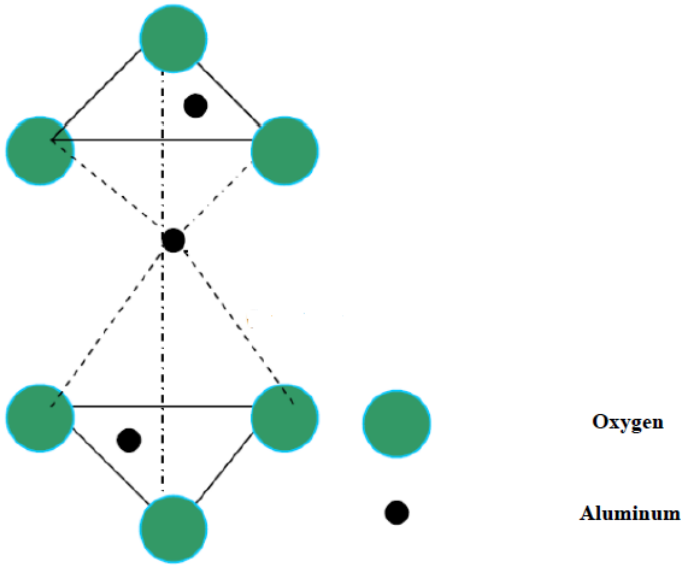

Fig 1.1 Schematic demonstration of oxygen arrangement around Al^{3+} ion in alumina [3]

Table. 1 Physical and mechanical properties of alumina [4]

Property	Value
Density	3.96 gm/cc
Melting Temperature	2072 ºC
Tensile Strength	373.3 MPa
Flexural Strength	351.6 MPa
Poisson's Ratio	0.23
Compression Strength	2537MPa
Fracture Toughness	4.3 MPa $m^{1/2}$

Polycrystalline α–phase alumina is used as a structural ceramic due to its good mechanical properties [5] and excellent thermal properties. The major fields of applications for alumina are:

- Abrasives, high-temperature refractories, ceramics and glass
- Aluminum sulphate or activated alumina (the product of alumina, or clay, or bauxite, with sulphuric acid) is important in paper manufacture as a colour binder and filler.
- The electric and electronic industries widely use alumina ceramics.
- For electronics, the main product is the insulating substrate on which conducting or resistive, even capacitive or inductive, circuits are deposited due to high resistivity. Jewelry (jewels, scratch-proof glass for watches), Lazer matrices, and substrates for specific electronic circuits and waveguides are the primary applications of single sapphire crystals, as well as abrasion-resistant optical windows: for military use, but also barcode readers in supermarkets. However, alumina has found the most widespread use in polycrystal state:

the internal, transparent tube of sodium vapor lamps used for street lighting. Transparent alumina has several applications, such as electromagnetic windows, transparent armor, envelopes of high-pressure metal halide lamps.

1.1.2 Zirconium dioxide ceramic

Zirconium dioxide (ZrO_2), usually known as zirconia, is a crystalline ceramic material identified in 1789. Zirconia has high strength and high fracture toughness than the other ceramics with this unique property; these ceramics are called ceramic steels [6]. Zirconia ceramics are used to fabricate for many engineering applications such as extrusion dyes, valves and port liners for combustion engines, biomedical implants, thermal shock resistant refractory liners or valve parts in foundries. Several reliable solutions (ZrO_2-MgO, ZrO_2-CaO, ZrO_2-Y_2O_3) were tested for biomedical applications in the early development stages. Zirconia is doped with stabilizers to attain high hardness and strength and fracture toughness to achieve structural application demands. The research focused on zirconia-yttria ceramics systems, characterized by fine-grained microstructures known as Tetragonal Zirconia Polycrystals (TZP). Zirconia is a well-known polymorph that occurs in three forms: monoclinic (M), cubic (C), and tetragonal (T) [7].

Zirconia is a polymorphic material and exhibits three temperature-dependent phases; at room temperature, it exists in monoclinic form (known as baddeleyite), which transforms to tetragonal (1170 – 2300 °C) and cubic crystal structure (2370 – 2680 °C) upon heating, as shown in Fig. 1.2.

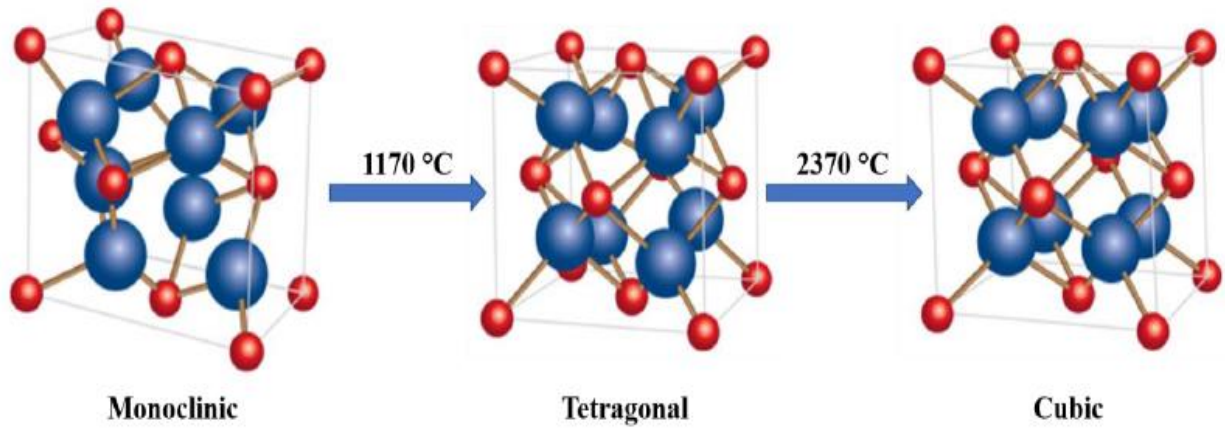

Fig. 1.2 *Polymorphs of Zirconia (Red spheres represent Zr, and blue represent O)[8].*

The reversible transformation of the tetragonal to monoclinic phase while cooling is thermal and martensitic. It is accompanied by a sudden crystal volume expansion of ~ 4%, making the sintering of monoclinic zirconia difficult [9]. The expansion while cooling creates internal stress and induces microcracks, which disintegrate the component. For successful sintering of zirconia, the volume expansion during cooling needs to be controlled to stabilize high-

temperature phases to room temperature. Early efforts of rapid quenching of monoclinic zirconia to obtain high-temperature phases didn't offer consistent results [9]. In 1929, Ruff et al. reported the tetragonal structure of zirconia at room temperature for the first time by adding different oxides (CaO, MgO, ThO_2, etc.) [10]. The addition of oxide dopants to zirconia changed the transformation temperature and stabilized the high-temperature phases at room temperature; it was estimated that a significant amount (> 15 mol.%) of CaO or MgO was required to stabilize the cubic phase of zirconia at room temperature [11]. These cubic stabilized solid solutions are known as fully stabilized zirconia (FSZ). Garvie et al., in their work, found that the dispersion of metastable tetragonal zirconia in cubic zirconia showed enormous improvement in mechanical properties compared to FSZ, and they are labeled partially stabilized zirconia (PSZ) [6,12].

1.1.2.1 Stabilization of zirconia by doping

Pure zirconia cannot maintain an 8-fold fluorite structure at room temperature because of Zr's smaller atomic size. It is overcrowded by oxygen atoms around it, which causes internal strain in the lattice [13]. These internal strains can be partially relieved by changing atom order to 7-fold monoclinic structure. Therefore, zirconia exists in the monoclinic structure at low temperatures. As discussed previously, zirconia's high-temperature phases can be stabilized at room temperature by doping them with certain aliovalent oxides (Y^{3+}, Gd^{3+}, Cr^{3+}, Ga^{3+}, Fe^{3+}, Ce^{4+}, Ge^{4+}, etc.). The addition of oxide dopants with a higher atomic radius and lower valency than Zr (example: Y^{3+}, Gd^{3+}) can reduce the internal strain by relieving oxygen overcrowding and generating oxygen vacancies lattice for charge compensation represented in Fig. 1.3.

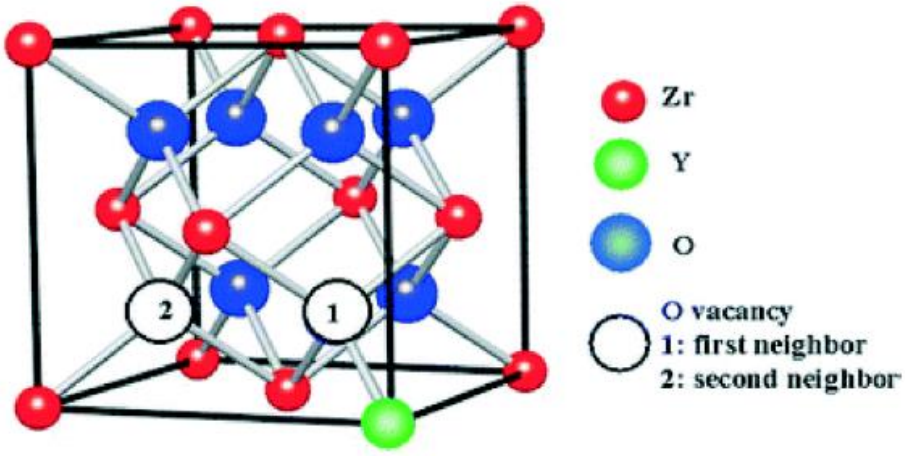

Fig. 1.3. *Position of oxygen vacancies in Yttria or Gadolinia stabilized zirconia [14].*

The addition of Y_2O_3, which has a higher cation (Y^{3+}) radius and lower valence than Zirconium ion, replaces Zr^{4+} with Y^{3+} ion, relieves oxygen crowing and creates oxygen vacancies for charge compensation as shown in **Fig. 1.4**, which favors 8- fold fluorite structure, this can be

understood better with the help of Kroger-Vink notation stated below. Where Y'_{Zr} represents Y^{3+} in cation site with a single negative charge, substituting Zr^{4+} ions. O_o^x indicates oxygen ions in anionic sites with neutral charge and $V_o^{\cdot\cdot}$ represents oxygen vacancies with a double positive charge.

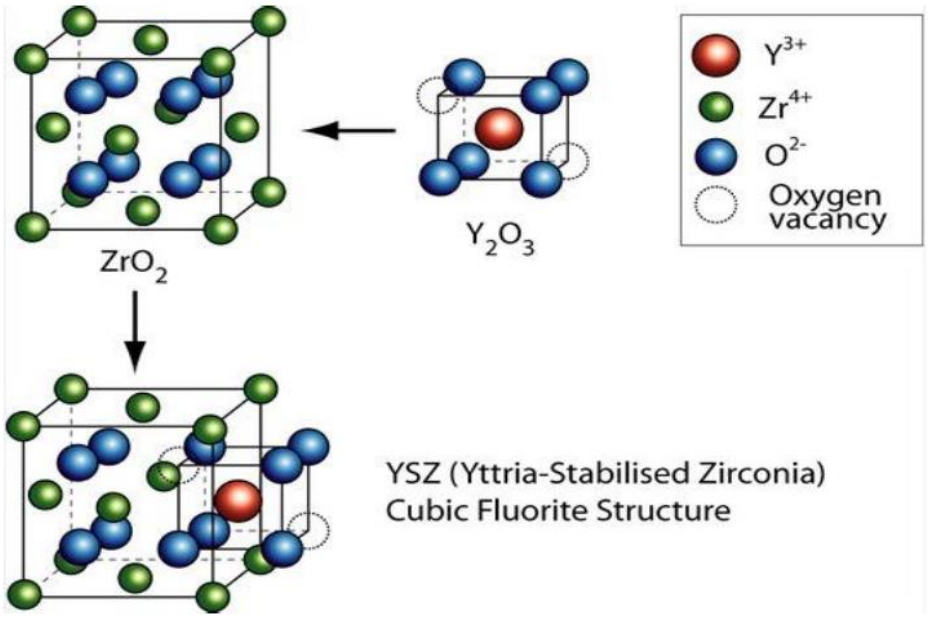

Fig. 1.4 *Stabilization of zirconia with yttria addition [9]*

As oxygen vacancies show preference to be closer to the smaller cation, oversized dopant vacancies will be closer to Zr ion. In contrast, in the case of undersized dopants, they will be bonded to dopant cations. Therefore undersized dopants cannot relieve oxygen overcrowding around Zr^{4+}. Hence, the stabilization mechanism explained with oxygen vacancies associated with Zr ions

1.1.2.2 Types of stabilized zirconia:

Depending on phases and their distribution, zirconia ceramics can be classified into three types:

1.1.2.3 Fully stabilized zirconia:

Fully stabilized zirconia (FSZ), also known as cubic stabilized zirconia, contains only a single cubic phase. These can be obtained by adding enormous amounts of stabilizers, and its microstructure contains large cubic grains. Generally, FSZ has limited structural applications because of its low mechanical properties and is mostly used in high-temperature applications as thermal barrier coatings, heat exchangers and solid electrolytes. Single-crystal cubic zirconia ceramics are popularly known as synthetic diamonds.

1.1.2.4 Partially stabilized zirconia

The Partially stabilized zirconia (PSZ) contains tetragonal or monoclinic precipitates in cubic grains, which can be observed in CaO, MgO stabilized zirconia. PSZ ceramics have better mechanical properties than FSZ and can be used in structural applications.

1.1.2.5 Tetragonal zirconia polycrystals

These are single-phase tetragonal zirconia ceramics and possess high fracture toughness due to a phenomenon known as stress-induced transformation toughening. TZP ceramics' microstructure contains finely distributed small tetragonal grains and has excellent mechanical properties. The improved mechanical properties of PSZ and TZP were due to the absorption of energy during tetragonal to monoclinic martensitic transformation. The increase in volume due to this transformation around the crack tip closes the crack and increases its propagation resistance, thereby increasing fracture toughness. Therefore the mechanism is referred to as transformation toughening.

1.1.2.6 Tetragonal (t) to Monoclinic (m) transformation in stabilized zirconia

The transformation from the tetragonal to the monoclinic phase in zirconia is martensitic. The martensitic transformation originated from steels. A hard phase called martensite forms when a high-temperature austenitic phase is quenched in steels, and this process is known as martensitic transformation. The martensitic transformation is diffusionless, athermal, and involves quick, simultaneous, and cooperative movement of atoms over a distance of less than interatomic spacing, which results in microscopic shape deformation in the transformed region. This change in shape is responsible for transformation toughening.

The factors responsible for t-m transformation in zirconia can be explained by the equation given by Lange [15], The total free energy per unit volume needed for the transition of the tetragon to the monoclinic phase can be defined as:

$$\Delta G_{t\rightarrow m}=(G_{cm}-G_{ct})+(U_{sem}-U_{set})+(U_{sm}-U_{st}) \quad (1.1)$$

Or

$$\Delta G_{t\rightarrow m}=-\Delta G_c+\Delta U_{se}+\Delta U_s \quad (1.2)$$

ΔGc is the difference in chemical-free energy between the tetragonal and monoclinic phases. It depends on temperature and composition; ΔU_{se} changes elastic strain energy associated with particle transformation. It depends on the modulus of the surrounding matrix and external stresses, and ΔU_s is the change in surface free energy of transformed particles or grain. If $\Delta G_{t\rightarrow m}<0$, then the tetragonal phase is unstable and turns into monoclinic and if $\Delta G_{t\rightarrow m}>0$, then the tetragonal phase retains in the particle or grain. The total free energy change $\Delta G_{t\rightarrow m}$ can be increased, and the tetragonal phase can be retained by decreasing ΔG_c, increasing ΔU_{se} or increasing ΔU_s. It is well known that with the help of stabilizers, one can strengthen δGc. ΔU_{se} can be improved by reducing external stress, and decreasing grain size can improve ΔU_s.

1.1.2.7 Transformation toughening of zirconia ceramics

The high toughness of zirconia ceramics is mainly due to its transformation to the monoclinic phase when subjected to stress. The transformation toughening in zirconia ceramics for the first

time and reported an enormous amount of strength and toughness improvement in PSZ [6]. Because of the stress developed by the crack propagation, metastable tetragonal zirconia transforms into a stable monoclinic phase; this transformation is accompanied by a volume expansion of ~4%. The volume expansion in the vicinity of crack propagation provides compressive stress, which reduces crack propagation, as shown in Fig. 1.5.

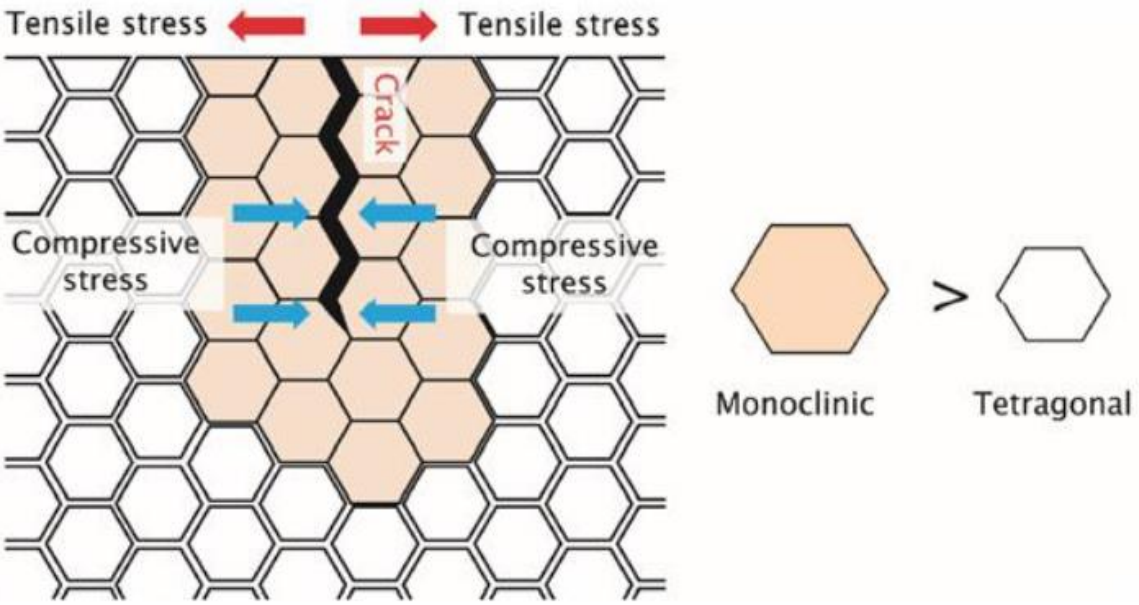

Fig. 1.5` *Schematic representation of transformation toughening in zirconia ceramics [16].*

In the presence of moisture, the transformation from tetragonal to monoclinic can occur without propagation of the crack, and this phenomenon is known as Low-temperature degradation. If the transformation is triggered by crack propagation, one can get enhanced toughness. On the other hand, the transformation may be triggered by a reaction with water molecules on the surface, resulting in surface roughening, microcracking, and grain pull-outs (known as low-temperature degradation).

1.2 Introduction to Porous structures

Porous materials are usually considered materials with more than 30% porosity, and their conventional dense equivalents cannot reach the unique characteristics and properties of materials with controlled porosity. Man has made use of porous materials for centuries [17]. Big Shigir is one of the ancient wooden artefacts that has been found in Russia (Fig. 1.6). Scientists have estimated the age of this artefact to be 11,500 years. Wood is a naturally porous material, and for ages, human civilization has made use of it for a wide range of applications. Due to their attractive combination of porous structure properties such as lightweight, high energy absorption, and low thermal mass, porous materials of different material systems (metals, polymers, and ceramics) can be found in a variety of applications in molten metal filters, hot gas filters, medical implants and catalysts [18]. Porous structures can be fabricated

from any materials such as metals, plastics, ceramic, glass, and even composites. Porous structures are classified into two porous primary structures groups; engineered honeycomb and reticulate ceramic foams. The foams can be classified into two types based on their pore structure: open-cell structured foams (also known as reticulated foams i.e. like a net) and closed-cell foams shown in Fig 1.7. A honeycomb's cells have square, hexagonal, and triangular, etc. On the other hand, foams are three-dimensional porous materials in which cells are interconnected and oriented randomly. Fig. 1.7 shows that various natural materials such as bone, wood, etc., have different porous structures. Bone (Fig. 1.7a) contains an open porous structure with interconnected pores. Bird feather rachis (Fig. 1.7b) and bamboo (Fig. 1.7c) have a closed-cell porous structure. One of the impressive porous structure of long, directional pores can be observed in honeycombs (Fig. 1.7d) and wood (Fig. 1.7e). Honeycomb consists of ordered hexagonal pores with no transverse connectivity, but they are open along hexagons' axes. Similarly, wood (Fig. 1.7f) contains elongated pores along the tree's trunk, and they are not connected in the direction of the ray. Among different porous architectures, the one which exhibits higher mechanical properties compared to other structures can be selected.

Fig. 1.6 *Big Shigir* [17]

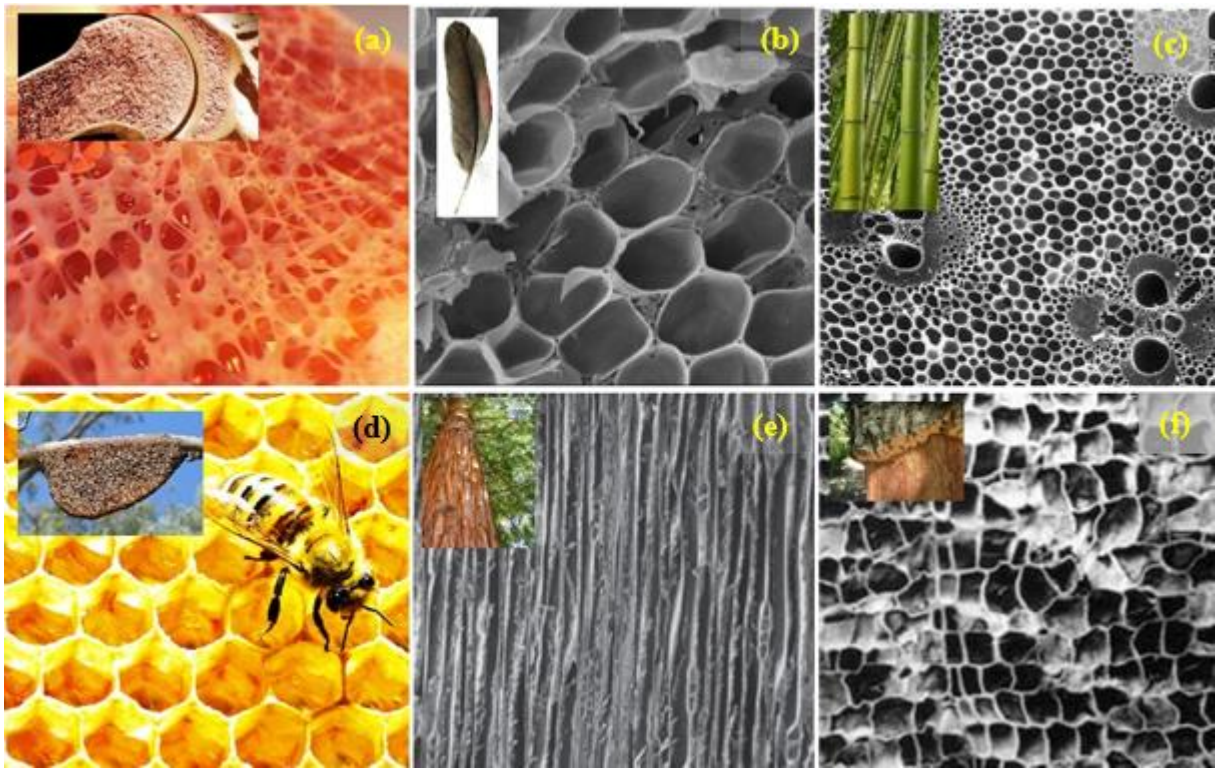

Fig. 1.7 *(a) Open pore structure of bone, (b) and (c) closed-cell structure of rachis and bamboo, (d) hexagonal pore structure of a honeycomb, (e) and (f) directional pore architectures of cedarwood and cork* [19–22].

Properties of these porous structures are a function of the material of fabrication and the structural parameter, namely size and shape of the cells, distribution of the between the cell edges and faces, and the relative density or porosity.

1.3. Ceramic porous structures

The porous structures can be fabricated out of metals, plastics, ceramics, glasses for a wide variety of engineering applications, e.g., polymeric and glass foams for thermal insulation, polymeric foams for packaging industries, metallic and glass sandwich panels for structural uses, closed-cell polymeric foams support for floating structures, etc. Ceramics materials have exceptional properties from the material property charts, typically known as Ashby charts Fig 1.8. With these special properties, ceramics is a natural choice for high-temperature applications compared to metal and polymers. Ceramic foams have numerous applications due to their low densities and high melting points, low thermal conductivity, and high corrosion resistance. Engineering foams are classified into two groups: open-cell and closed-cell. Open-cell ceramics foams have been studied for use as the molten metal filter in foundry application, hot gas filters and scaffolds in tissue engineering. [17,23–25]. Ceramic foams with closed cells are used for high-temperature insulation, including insulation for furnaces. All the alumina ceramic materials have superior mechanical properties and lower density, which is very

suitable for lightweight applications compared to other ceramics. Among all porous ceramics, porous alumina structures exhibit unique characteristics such as comparatively high intensity and improved thermal and chemical stability. Porous alumina ceramics, therefore, play an essential role in high-temperature systems. Alumina porous structures can be used as catalyst substrates for a catalytic converter, shock attenuating parts, molten metal filters, refractory linings of furnaces because of their high melting point, filtration of gases and porous scaffolds for tissue engineering in the case of biomedical applications. [26]. Zirconia-toughened alumina (ZTA) has been developed to replace alumina in applications where greater tolerance to fracture is needed. Zirconium Oxide (ZrO_2) ceramics had higher bending strength and fracture toughness when compared to Al_2O_3.

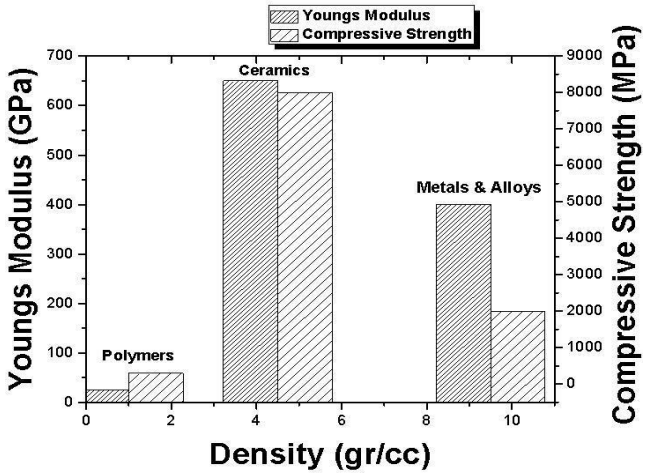

Fig. 1.8 *Young's modulus and Compressive strength vs density [1]*

1.4 Applications of porous ceramics

Porous ceramic structures (open cell/closed cell) used in different applications are shown in Fig 1.9.

- Energy-absorption devices such as antimine boots and automobile bumpers.
- Structural sandwich panels in lightweight building panels.
- Molten metal filters in foundries for removal of inclusions.
- Catalyst substrates for automobile applications and pollution control of health-hazardous gases emitting from stationary devices.
- Heat exchangers for energy conservation, energy-efficient air-heaters etc.
- Open-cell foams are used as porous scaffolds in tissue engineering; their interconnected porosity is essential for cells to penetrate the scaffold and migrate through it.
- Closed-cell foams excellent materials for thermal insulation

Fig. 1.9 *shows applications of porous ceramic (a)-(b) Energy Absorption devices, (c) Molten Metal Filters, (d) Catalyst Substrates (e) Porous scaffolds used in tissue engineering [27]*

1.5 CAD models through X-ray tomography

3D models were developed with the help of therapeutic imaging procedures, for example, Computed Tomography (CT) and Magnetic Resonance Imaging (MRI) or ultrasound scanning (US). The CT is mostly focused on hard tissue observations such as ceramics and bones etc. The CT data is observed as a pile of x-rays and this data is processed through commercial or open-source software to get final 3D models. Where additional alterations or adjustments are required, it can be made to 3D CAD model. The 3D CAD model is converted to an STL file, and this STL file is used as input to 3D printing machine. Finally, the 3D printing machine is used to manufacture the required 3D model. Subsequently, post-processing is required to get the final product. The post-processing contains surface finishing and support removal. The last advance in the work process is the medical application. The complete procedure is shown in Fig 1.10.

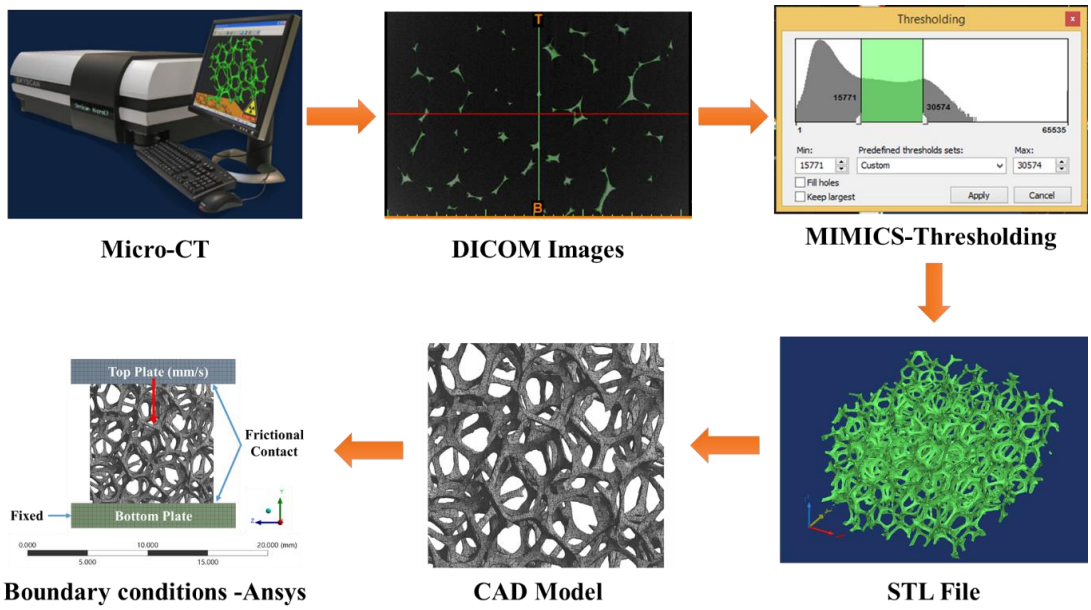

Fig.10 *Procedure to manufacture CAD models [28].*

With the help of Computer-Aided Design and Manufacturing technologies (CAD/CAM), the medical imaging techniques offer new possibilities for fabricating customized cranial implants. With the help of Computer-Aided Design and Manufacturing technologies (CAD/CAM), medical imaging techniques offer new possibilities for the fabrication of customized cranial implants. Now the object of the work is presented below.

1.6 Objectives of the work

- Fabrication of alumina and ZTA foams with different PPI levels through a sponge replication process
- Fabrication and properties evaluation of polymer encapsulated and infiltrated alumina and ZTA foams through sponge replication of technique
- Fabrication and properties evaluation of metal encapsulated and infiltrated alumina and ZTA foams through polymeric sponge replication of technique
- Effect of nickel coating on the mechanical behaviour of polymer replicated Al_2O_3 and ZTA foams.
- Microstructural and mechanical properties of alumina and ZTA foams prepared by the thermo-foaming technique
- Closed-cell alumina and ZTA foams prepared by sacrificial template method

1.8 Organization of the thesis

The thesis has been divided into nine chapters:

Chapter 1: Introduction

Chapter 2: Literature survey

Chapter 3: Experimental Methods

Chapter 4: Open-cell foams prepared through sponge replication method

Chapter 5: Study the effect of nickel coating on ceramic foam through electrolysis technique

Chapter 6: Open-cell foams prepared through thermo-foaming method

Chapter 7: Closed cell foams prepared through sacrificial phase template method

Chapter 8: Deformation study through simulation

Chapter 9: Summary, conclusions and scope for future work

A brief discussion of these chapters is given below:

Chapter 1 presents the background of ceramics, porous ceramics and their applications in various fields, alumina and ZTA ceramics used to fabricate porous ceramics in different applications, and the organization of the thesis.

Chapter 2 outlines a detailed literature review on the fabrication of porous structures by different fabrication techniques and mechanical behaviour of porous ceramics and their composite and studying the deformation behaviour of ceramic foams.

Chapter 3 deals with the details of raw materials used in the study and fabrication of open cell/ closed cell of alumina and ZTA foams (with 10, 20 and 30 PPI) through different methods i.e., polymeric sponge replication process, thermo- foaming, and sacrificial phase template method. Encapsulation and infiltration with polymers and metals to study the composite effect. Optimization of processing parameters and sintering schedule. Different equipment and techniques used for physical and mechanical characterization

Chapter 4 describes the fabrication of alumina and ZTA open-cell foams through sponge replication process. Optimization of processing parameters (i.e. solid loading, number coatings) and physical and mechanical properties evaluation of dip coating, dip+spary coating foams is described in detail.

Chapter 5 explains the effect of nickel coating on the alumina open-cell foam through the electrolysis technique. Optimization of bath composition and processing perimeters and physical and mechanical characterization for evaluating phase identification and compressive strength with respect to the coating thickness are discussed in depth.

Chapter 6 explains the fabrication of alumina and ZTA open-cell foams prepared through the thermo-foaming method. Optimization of processing parameters and physical, mechanical properties evaluation with respect to different powder to sucrose weight ratios range 0.6 to 1.4 are discussed in the chapter.

Chapter 7 explain the fabrication of alumina and ZTA closed-cell foams prepared through the sacrificial phase templated method. Physical and mechanical properties were evaluated with respect to the pore size and porosity of the sample.

Chapter 8 describes the deformation behaviour of the foam under quasistatic compression through simulation. X-ray tomography studies were used to design the CAD model for simulation. The simulation study reveals the foam's crack initiation and propagation. These simulation values were compared with experimental values.

Chapter 9 brings out significant findings, concludes the research work's outcome, and presents scope for future research.

Chapter-2

Literature Review

2.1 Porous structures

In the last few years, there has been an increase in interest in developing and using extremely porous ceramic materials due to their various uses and applications in many fields [29]. Dense materials processed by powder metallurgical routes usually contain defects in the form of pores or voids. Porosity, in general, is not desirable in engineering solids because of the detrimental effects on the mechanical and functional properties in the end applications [30]. However, most engineering solids such as metals, ceramics, and polymers contain small percentages of processing-induced porosity, which is inevitable. Interestingly, there are numerous natural solids such as bones, cork, wood, leaves, sponges, and coral where the constituent materials are arranged in a fashion that leads to forming a two or three-dimensional arrangement of pores creating highly porous architectures. The superior structural and biological functionalities of such natural porous solids are attributed to both the constituent material(s) and the porous structure. As nature continues to inspire the development of modern materials and structures, engineered porous structures emerged as a special class of materials with unique structures that contain a specific arrangement of the micro/macroscopic pores and a porosity level of 30 vol.% or higher [31,32]. Both natural and engineered porous structures find extensive use in lightweight structures, load-bearing components, thermal insulations, filters, packaging materials, solid-state battery electrodes, solid oxide fuel cells, and impact energy-absorbing structures. The low density of porous structures aids in designing lightweight but mechanically tolerant structures such as sandwich panels widely used in automobile, aerospace, and military applications. The low thermal conductivity of porous structures facilitates the fabrication of reliable, efficient, and economical thermal insulations that can only be matched in performance by expensive vacuum-based insulations. The architecture of the pores has a significant influence on the choice of a specific area of application for porous structures. In this respect, Fig 2.1 shows that porous structures with open-pore architecture were considered to be more suitable for functional than structural requirements. In contrast, those with closed pore architecture were more appropriate for structural than functional applications. Then, porous structures with partially open-pore architecture had a wider scope of application because they tend to meet structural and functional requirements [33,34]. Accordingly, porous structures are defined as natural or artificial solids with closed or open pores, voids, cavities, channels, or interstices with varying shapes [35].

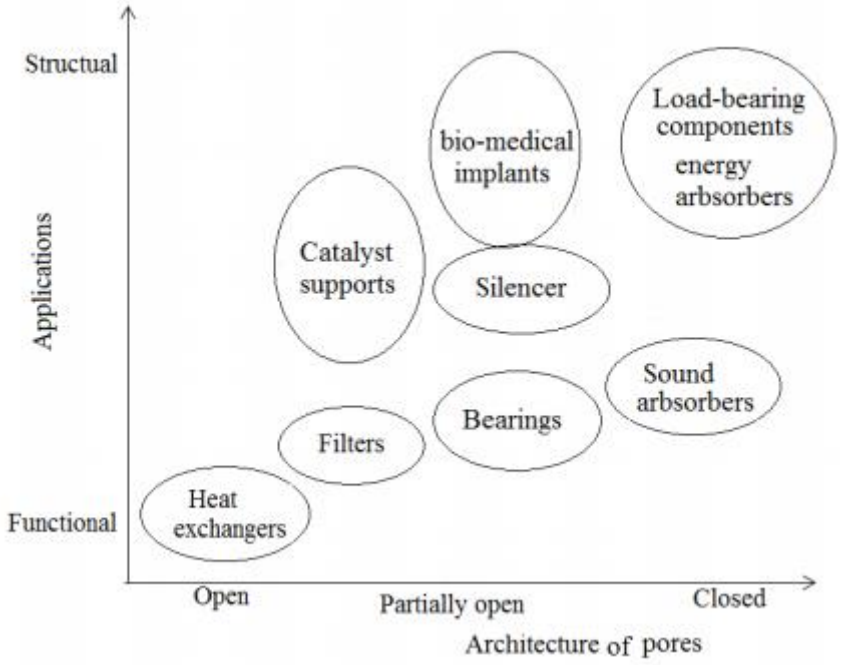

Fig 2.1 *Application Vs. pore architecture. Source [33].*

The morphology and architecture of the pores determine their properties and areas of application [33,36–41]. Structurally engineered porous structures can be broadly categorized into honeycombs and foams. A typical porous honeycomb structure consists of a two-dimensional array of hexagons/polygons that are elongated along the third dimension. On the other hand, foams are porous structures containing polyhedral-shaped cells packed in three dimensions to occupy the entire available space. Foams can be fabricated as both open-cell and closed-cell structures; if the constituent material of the foam is contained only in the cell edges, then the foam is said to be an open-cell foam. If the edges and the faces are both solid so that each cell is isolated from its adjacent cells, the foam is said to be a closed-cell foam. If the pores are open on both sides, without definite shapes, and arranged as a random network of bubbles, the structure is described as a reticulated pore [42]. In the isotropic pore structure, the pores are oriented so as to give the same physical properties in all directions.

In contrast, in an anisotropic pore, the pores are oriented to give varying physical properties in all directions [43,44]. All these are illustrated in Fig 2.2. Finally, porous structures are categorized as porous if their porosity varies between 20 % and 70 %, and as foamed or cellular if their porosity varies between 70 % and 95 % [37,45].

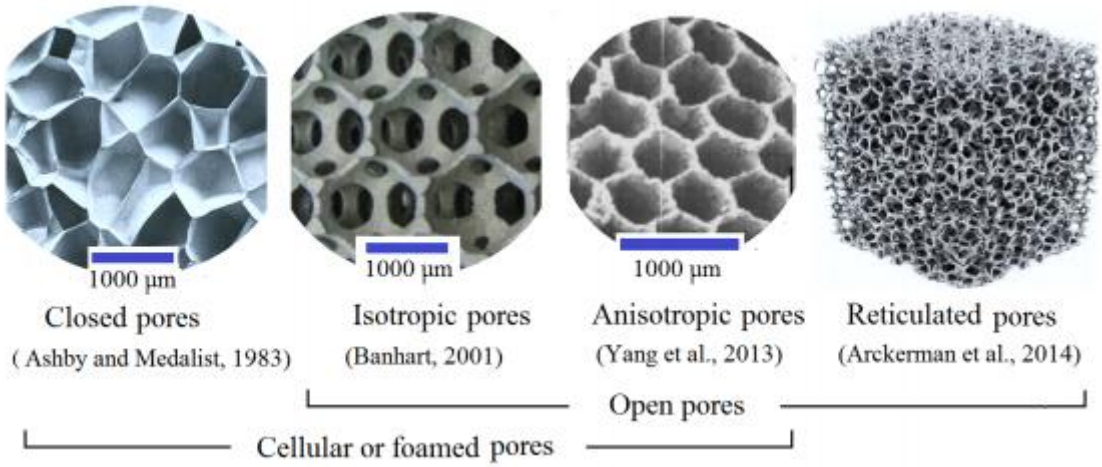

Fig.2.2 Different morphology of p*ore structures*

2.1 .1 Properties porous structures

The porous structures properties depend on the following parameters [46,47]. Those are

- The properties of solid of which the porous structure is made
- Processing route that is used for the fabrication of cellular materials
- The interconnectivity of the struts and shape of the cells
- The porous structure's relative density is a solid cellular density ratio to the solid's density.

2.1.2 Applications of porous ceramics

2.1.2.1 High-temperature thermal insulation applications

The need for thermal insulation is critical for technological development, but many industrial processes would not be possible without adequate thermal insulation [48]. The use of thermal insulation helps to reduce power consumption during the processing of materials at high temperatures and protects the surrounding spaces from the heat produced by the processing environment. The properties of ceramic foams, such as low density, low thermal conductivity, chemical inertness, high-temperature stability, and thermal shock resistance, make them ideal for thermal insulation applications [49]. The use of ceramic foams with closed pore morphology is preferred since it prevents the convective component of heat transfer. Alumina, zirconia, SiC and mullite foams are used as insulating materials due to their stability at very high-temperatures.

2.1.2.2 Acoustic absorbing materials

The mechanism of sound absorption by ceramic foams is as follows: when sound waves enter a porous ceramic body, the air in the pores vibrates and creates friction with the strut [1]. Due to the viscous effect, the sound waves are converted into thermal energy and absorbed. The

requirements of a ceramic foam used for acoustic absorption application are small pore sizes (20–150 μm), high porosity (above 60 vol.%), and high mechanical strength [50]. Their good fire and weather resistance are added advantages for them to be used as sound-absorbing materials in high-rise buildings, subways, tunnels, TV emission centers, and cinema centers.

2.1.2.3 Molten metal filtration

In most molten-metal processing, undesirable nonmetallic inclusions are introduced into the melt during the acts of melting, transporting, and alloying the metal before casting them into molds [29]. Once the metal is cast, these inclusions can result in defects that render the product unusable. Reticulated ceramic foams are used for the filtration of molten metal before casting [51]. To act as filters for molten metal, ceramic foams should have appropriate pore size and pore interconnectivity, sufficient strength, high-temperature stability, good thermal shock resistance, and good erosion resistance. The selection of the ceramic foam as a filter material depends on the molten metals which have to be filtered. For filtration of ferrous metals and alloys with high chemical activity and high casting temperatures, alumina and silicon carbides with great chemical stability are usually selected. The multi compositional ceramics are also used to form a filtration system. For example, ceramic foam filters made from a composition containing alumina, SiC, cordierite and zirconia are used for the filtration of molten Al, Cu, Zn, and bronze.

2.1.2.4 Catalyst support

Ceramic foams are extensively employed as a support for metal catalyst particles used in multiphase catalysis. Alumina, titania, zirconia, silica, and silicon carbide foams are used for this purpose [29]. Supports play a major role in the promotion of the reaction. The tortuous channels in ceramic foams can generate turbulence and then ensure good mixing of the reactants. Compared to the reactor-filled with stacking particles, the reactor with a ceramic foam core can reduce drop in pressure [52]. A large surface area is needed to achieve good contact between the catalysts and the flowing reactants. The ceramic foams have a relatively high surface area and the surface area can be further increased by coating them with other microporous materials such as zeolites or aerogels [53]. Some of the specific examples in which ceramic foams are used as catalyst support include oxidation of ammonia, decomposition of organics by photo catalysis, and destruction of volatile organic compounds (VOCs) by incineration.

2.1.2.5 Bio-implants

Bio-scaffolds are utilized for bone tissue engineering applications to facilitate the repair of bone damaged due to illness, injuries, or deterioration. The scaffold structure must be three-dimensional and facilitate cell interaction by providing an avenue to transport nutrients and oxygen and to allow tissues and capillaries to develop [54]. Additionally, the materials used to fabricate the scaffold must be biocompatible, bioactive, or biodegradable. Hydroxyapatite and tricalcium phosphate have similar chemical compositions as that of natural bones. The development of porous bone replacement materials from hydroxyapatite is addressed to mimic the micro and macroporous architecture of the mineral phase of living bone. This prevents interference of connective tissue formation, which will obstruct the long-term stability of the implant. For bone repair strategies, macroporous hydroxyapatite ceramics with highly interconnected pores are required to provide in-growth access of surrounding host tissues, facilitating the further deposition of newly formed tissue in the spherical cavities. When used as implants, hydroxyapatite (HA) foam becomes filled with mature new bone tissue and osteoid without any immune or inflammatory reactions after the implantation period. This is attributed to the high biocompatibility of HA and the suitability of foam networks in providing good osteointegration. Porous hydroxyapatite ceramics with gradient porosity [55] and bimodal pore structure have also been studied for bone graft applications. In addition, porous hydroxyapatite ceramics are used as drug-releasing agents [56–58].

Porous ceramics structures can be manufactured with a range of microstructures with regulated properties using many flexible and easy methods (Fig. 2.3).

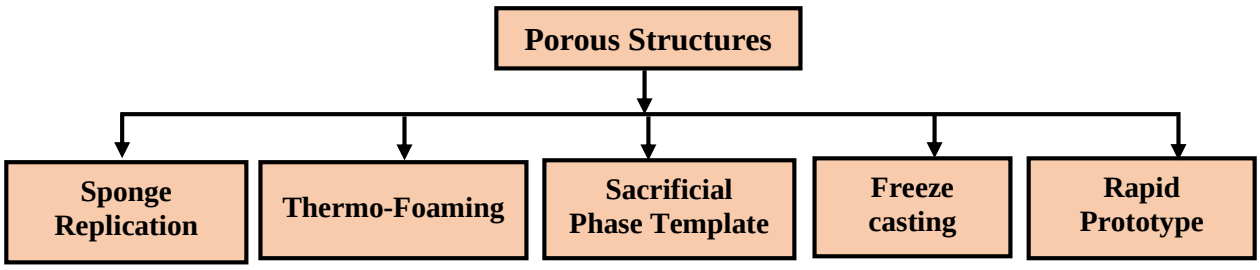

Fig 2.3 *Different fabrication methods for the fabrication of porous ceramics* [27,59]

2.2 Replica Method

The polymeric sponge replication process is the most widely used conventional procedure for creating open-cell foams. In this process, polymeric organic template impregnated in a ceramic slurry, accompanied by thermal treatment, resulted in the organic template's combustion and followed by sintering of a pore skeleton to produce porous ceramics with the same morphology

as the original porous material. This approach's most essential steps are impregnating suspension's rheology and its adhesion to the polymeric sponge. These techniques provide an easy alternative for developing 20% to 90% porosity macroporous ceramics and an average pore size ranging from 1-700 micrometers [60,61]. The properties of the ceramic foam formed by this route can be varied by varying the rheological properties of the slurry, such as characteristics of the viscosity and polymer foam, such as the PPI (number of pores per linear inch), the size of the pore, the shape, its distribution and foam density [62]. The sponge replication method was the first process to developed to manufacture porous ceramic structures. The fundamental theory for this methodology is depicted in Fig.2.4 [60]. The replication process can be separated into two separate forms: the synthetic template (synthesis template) and the natural template. Schwartzwalder and Somers started utilizing polymer sponges to manufacture porous ceramics in 1963. After that, the sponge replica technique has become one of the most common methods for producing porous ceramics. A high porosity polymeric sponge (usually polyurethane) is used in this technique.

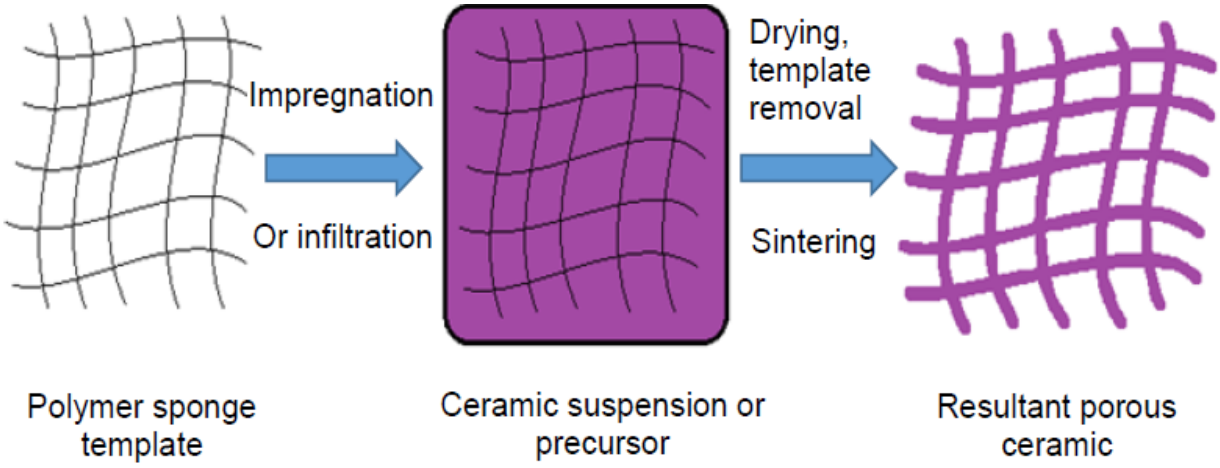

Fig 2.4 *Schematic of the replica method illustrating all the steps involved in the fabrication of ceramic foam [17].*

Fabrication of porous ceramic structures through the polymer sponge replication process is usually a polymeric sponge first submerged in ceramic suspension. The excess slurry is then extracted by moving the impregnated sponge through the rollers, and a ceramic slurry covering is built over the struts of the original polymeric sponge. The ceramic-coated polymer template is subsequently dried and pyrolyzed by cautious heating between 300ºC and 800ºC. Heating rates that are usually less than 1ºC/min are expected. This step allows for progressive decomposition and polymeric diffusion content. Finally, the coating is densified by temperatures between 1100ºC and 1700 ºC based on the slurry composition. Dispersants were

used to achieve suspensions with appropriate rheology. Binders and plasticizers are also typically used to improve the ceramic coating strength by avoiding cracks on struts preventing pressure build-up during pyrolysis. Binders play an essential role in the fabrication of porous ceramics by adding strength to the green body [63]. Binders of powder are combined with ceramic products and liquid to create a viscous solution. They can be used to connect particles, provide plasticity, and assist in regulating slurry flow properties. Popular binders and dispersants are used in ceramic suspension. i.e. Darava-C, colloidal orthophosphate aluminium, potassium and sodium silicates, magnesium orthoborate, and colloidal silica hydratable alumina, polyvinyl butyral with polyvinyl butyral plasticizer-like polyethylene glycol, and polymerizable monomers. Polyvinyl alcohol (PVA) [64], potato, corn cassava [65], poppy seed, and wheat have all been used as binders in the production of porous ceramics[66–68]. Table 2.1 depicts the different examples provided by this approach documented in the literature. In addition to that, porous ceramics structures developed through this method usually have interconnected open porosity with a range of 40% to 95%. The pore size between 100 μm and 3.5 mm is shown in Fig. 2.5(a). However, there may be a separate form of defect in this production process, as shown in Fig. 2.5(b). The possibility of cracks and flaws formation during the polymer template's pyrolysis from the ceramic foam and such flaws can significantly harm the final mechanical features of porous ceramic.

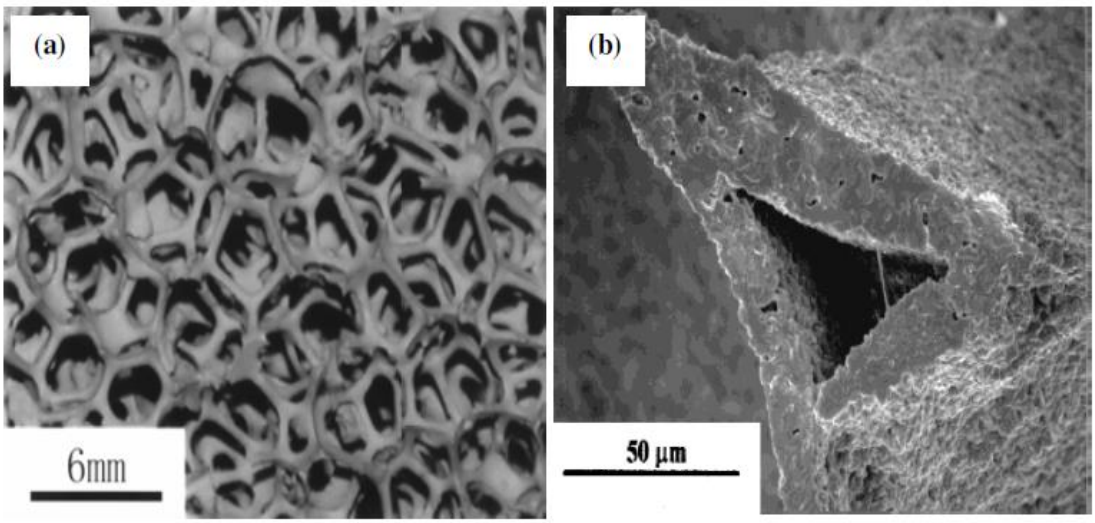

Fig. 2.5 *Images of porous ceramics prepared through the sponge replication method (a) ceramic foam with reticulated porous structure (b) strut defect after sintering [68,69].*

Many steps have been developed to address this drawback by utilizing polymer precursor solutions[70] and adding fibers to boost slurries' wetting on the polymer sponge. Nangrejo and

Bao developed a process to create polymeric precursor solutions for silicon carbide (SiC) foams and demonstrated the absence of holes in the middle of the struts'

The impact of recoating slurry viscosity on the properties of reticulated porous SiC ceramics was investigated by Xiumin Yao et al. [71]. It has been discovered that the recoating of the polymeric sponge includes a high viscosity slurry with a thixotropic loop. The improvement in viscosity caused by the increase in solid loading results in a decrease in cell size and increased strut thickness in SiC replicated porous ceramics. The decrease in cell size and rise in strut thickness contribute to an increase in solid loading. Compressive intensity improved from 0.78MPa to 1.59MPa as coating viscosity increased from 0.07Pa.s to 1.44Pa.s. The microstructure of the samples has been observed to have both large and small pores. Small pores were caused by sintering, whereas entrapped air bubbles caused large pores. The air bubbles were removed in part through the roller process of removing excess slurry. The polymeric sponge process [72] was used to make hydroxyapatite porous ceramics.

Zivcova et al. investigated the synthesis of porous alumina ceramics utilizing various foaming agents such as rice starch, lycopodium, coffee, flour, semolina, and poppy seed. Many of the formation agents were granular (5m – 1 mm) and had a low density (1.1-1.5 g/cc) [73]. Standard slip casting (TSC) and starch consolidation techniques were used to prepare the samples (SCC). But for poppy seed, which displayed thermal effects up to 600 °C, all pore formers exhibited burning activity between 250-550 °C. Since the starch needed to create pathways for exhaust gasses during pyrolysis to prevent stress and cracking of the samples, using poppy seed as a pore formed by conventional slip casting was not effective. According to the results, both starch-containing pore formers may be used in starch consolidation casting as both pore-forming and body forming agents.

Schwartzwalder et al.[59] discovered that ceramic cellular structures with varying porosities and pore sizes were processed through a polymeric sponge replication technique. After that, the sponge replica method became the most widely used method for developing high porosity open-pore ceramics. Polymer sponge, such as polyurethane foam (PUP), is the most commonly used template for porous ceramics fabrication.

Fitzgerald et al. [74] fabricated silicon carbide fine open-cell foam by using sodium chloride compact. Silicon carbide was infiltrated with Poly Carbo Silane (PCS). Water was used to leach out the salt, which contributed to the formation of PCS foam accompanied by the air's heating, and a brittle structure was finally formed after pyrolysis. The system, thus formed, had a

uniform open cell network with cell sizes varying from approximately 10 μm to 150 μm and having controlled densities.

White et al. [75] also used an innovative approach to maintain the composition of corals and other aquatic invertebrate skeletons by duplicating them. Under low pressure, the coral is first infiltrated with wax in this process. The mechanism culminated in a negative type of cellular structure. The leach out of the calcium carbonate-based coralline skeleton was used in a strongly acidic solution. Thus, the negative template was impregnated with a ceramic suspension, and a macro-porous ceramic was obtained by extracting the organic material by pyrolysis.

Table.2.1 Examples of Replica Methods Reported in the Literature

Type of template		Method& Precautions	Composition
Synthetic Templates	Polymer foams	Impregnation with ceramic Slurry	Alumina [37][43][44], Alumina fiber-reinforced [77], zirconium Oxide[52], SiO_2 , MgO [67] silicon carbide [67][78], Si_3N_4 [79], Titanium diboride [67], Alumina –ZrO_2 composite [80] Mullite [81][67][82][76][83] , Li_2O–ZrO_2–SiO_2–Al_2O_3 ceramic [84] SiC–Al_2O_3–SiO_2 composites [85], calcium phosphate-based composites [68][86], $La_{0.84}Sr_{0.16}Co_{0.02}MnO_3$ [87]
	Carbon foam	Chemical vapor deposition & infiltration	Silicon carbide, SiO_2, Si_3N_4, TiC, TiN, Titanium diboride, Titanium dioxide, ZrC, ZrN, Zirconium Oxide, Cr_2O_3, Alumna, among others [88]
Natural Template	Wood	Sol-gel process by using metal salts, hydroxides,	Iron Oxide [89], Alumna, Titanium Oxide [90–92], Silicon carbide, ZrC-C [93–95]
		Metal infiltration	Silicon carbide [94][96][97] , Si- Silicon carbide composites [97–99]
		Vapor infiltration and reaction with gaseous metals or metal precursors (CVI)	Silicon carbide [100] , Alumna [101] , Titanium dioxide [102] Titanium Carbide [102,103]
		Impregnation with ceramic Slurry	Silicon carbide [104]
		Impregnation with preceramic polymers	Silicon carbide composites [105]
		Liquid precipitation of precursors	Zeolite porous structures [106], Calcium phosphate composites [107]
	Coral	Impregnation with ceramic Slurry	Alumina [75] , PZT [108]
		Hydrothermal Reactions	Hydroxyapatite [109,110]

2.3 Sacrificial phase method

The sacrificial template technique is commonly used in the industry to process porous ceramics with different chemical compositions. Other pore formers (space holders) have been used to make a porous structure for various applications in this process. To obtain a two-phase composite mixture, the sacrificial phase is first homogeneously mixed with the ceramic powder or precursor(s). Homogeneous dispersion of the sacrificial phase within the matrix is critical to developing a uniform porous structure. Next, the sacrificial phase is removed from the mixture by pyrolysis, sublimation or evaporation, followed by sintering to obtain the final porous ceramic structure. The final porous structure is thus a negative replica of the initial sacrificial phase, as opposed to a favorable cellular structure that is achieved in the replica method [111–113]. Next, the sacrificial phase is removed from the mixture by pyrolysis, sublimation or evaporation, followed by sintering to obtain the final porous ceramic structure. The final porous structure is thus a negative replica of the initial sacrificial phase, as opposed to a positive cellular structure that is achieved in the replica method [29]. A schematic representation of the overall process is depicted in Fig. 2.6, and Fig. 2.7 shows the typical porous microstructures developed using the sacrificial phase technique [114–117]. The following routes are employed to develop the two-phase perform that after pyrolysis (or sublimation/evaporation) and sintering lead to the final porous structure: (i) dry mixing of the component phases followed by pressing [60], (ii) forming a two-phase colloidal suspension followed by slip, tape or direct casing [118], and (iii) impregnation of a previously consolidated preform of the sacrificial material with a pre-ceramic phase or a ceramic suspension [74]. Various pore formers were used to manufacture porous ceramics in these processes, such as synthetic and natural organic materials, chemicals, and salts. Table 2.2 represents the list of pore formers reported in the literature. By properly selecting the sacrificial phase, it is possible to vary the pore size from 1-700 μm and total porosity from 20-90 vol. %. Since the final porous structure is a negative replica of the sacrificial phase, defects in the ceramic walls can be avoided, resulting in improved mechanical strength of the porous ceramics [17]. The sacrificial phase technique has more advantages over other methods. It is feasible to modify the structure and different pore sizes with varying porosities using appropriate space holders (sacrificial phase). The pore former's pyrolysis is very time-consuming and emits a massive exhaust gas volume that can cause environmental issues. During pyrolysis, the volume of gas produced is the key downside of using organic material as a pore type which may trigger tension, cracking, and deformation. The disadvantages of burning plastic and natural organic products are partially overcome by using water and oils (volatile oils) as a sacrificial phase [114].

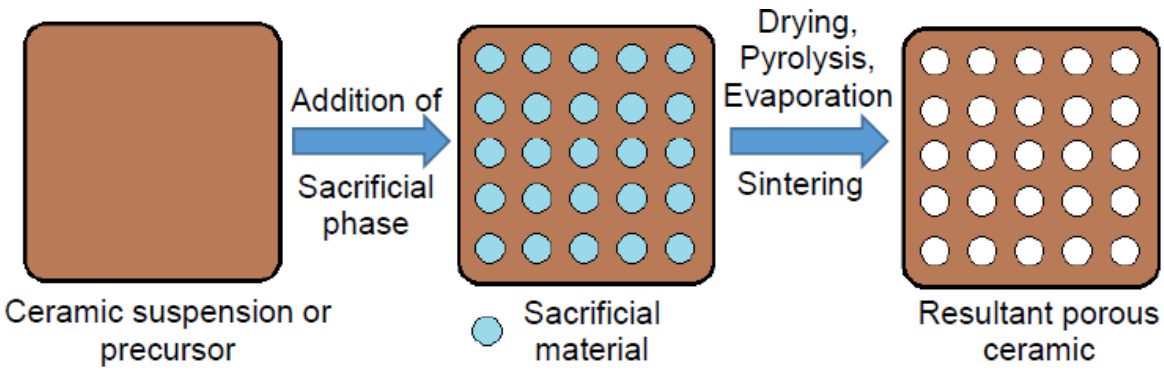

Fig 2.6 *A schematic representation of the sacrificial phase technique [17].*

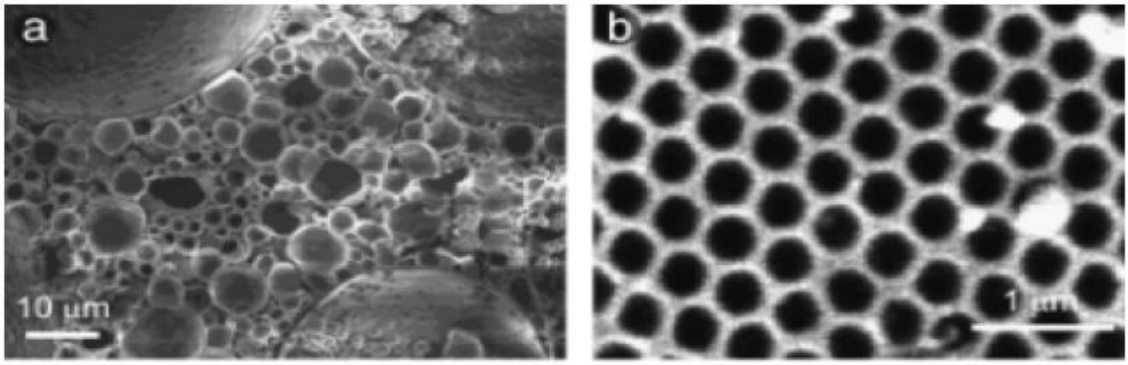

Fig 2.7 *Microstructures of macroporous ceramics produced using the sacrificial template method: (a) a TiO_2 foam* [114] *and (b) an ordered macroporous SiO_2 foam [115].*

Li et al.[119] used naphthalene powder particles as a pore-forming agent to silicon nitride to fabricate β-grain porous silicon nitride porous structures high-temperature sintering at 1700 °C in a high-pressure inert atmosphere. The flexural strength of the fabricated foam attributed between 50–120 MPa and 160-220Mpa in the porosity range 42–63% and 50-55%, respectively. Microstructural differences (equiaxed versus fibrous) affect the strength of the fabricated foam.

Diaz et al.[120] utilized rice flour (particle size: 5–18 µm) as a pore former to manufacture porous silicon nitride ceramics. The mix was placed under-stimulation for proper distribution of the pore former. The mixture was then frozen and vacuum-dried. Phosphoric acid (H_3PO_4) was used as a pore-forming agent for the fabrication of α-grained Si_3N_4 foams at a low sintering temperature (1000-1300°C) without gas pressure [121]. Porous alumina with directional pores produced by using mercerized cotton threads as pore-forming agents. By utilizing these cotton threads, different sizes of the diameter of pores were obtained [122].

Table.2.2 Examples of Sacrificial Template Methods Reported in the Literature

Sacrificial template		Material Composition
Synthetic organics	PVC beads	Alumina, $(Ca_{1-x,}\ Mg_x)Zr_4(PO_4)_6$ [86]
	Polystyrene beads	SiO_2 [115,123,124], Titanium dioxide- SiO_2 [124], Zeolite [125], Alumina [126][127]
	Polyethylene oxide (PEO) beads	Lead Zirconate titanate (PZT) [128]
	Polymethyl methacrylate (PMMA)	SiC [129], SiOC [60][130–132], Lead Zirconate titanate (PZT) [128] Hydroxyapatite [133][134]
	Phenolic resin	Si_3N_4 [135]
	Nylon	Silicon carbide [136]
	Polymer gels	Titanium dioxide, SiO_2 [137]
Natural organics	Seeds	Alumina [126]
	Cellulose/cotton	Alumina [138], Mullite [139]
	wax	Hydroxyapatite [140]
	Alginate	Alumina [141]
	Starch	Alumina [142][143][62][144], Lead Zirconate titanate (PZT)[145] , SiO_2–Na_2O–CaO–MgO glass, Hydroxyapatite [140][118,146], Mullite [147], Si_3N_4 [148], $CaCO_3$ [149], Diatomite [150] , Cordierite [151][152]
Liquids	Freeze -drying	Alumna [117]
	Emulsion Oils	Alumina [153], Titanium dioxide [154][155], SiO_2 [156]
Salts	Sodium chloride (NaCl)	Silicon carbide [74],
		Alumina [157]
		$PbTiO_3$, $La_{1-x}Sr_xMnO_3$[158]
Metals and ceramics	Nickel	Alumina, YSZ [159]
	Carbon	Silicon carbide [136], Mmullite [160]
	SiO_2 Particles	Silicon carbide [136]
	Zno	NiO, Silicon carbide composites [105]

2.4 Ice-templating process

Ice-templating is a processing technique to develop macroporous ceramic materials with characteristic features such as anisotropic pore architecture, hierarchical structural organization, and low pore tortuosity [161]. This is a relatively inexpensive technique for producing porous ceramics, which provides a means for bioinspired designs. In this process, ceramic powder is taken and suspended in the water. Then, the ceramic suspension is frozen unidirectionally under an applied thermal gradient. During the freezing process, the ice crystals start growing in the thermal gradient direction. Ice crystal has a unique feature: it grows 100 times faster in prismatic plane direction than its basal plane direction [162]. During the ice growth process, the growing ice crystals eject the particles in front of them, and the ejected particles are aligned between the two successive growing ice-crystals. This process makes a structure that consists of alternate layers of ice and ceramic particles. The frozen structures are taken to the sublimation process, in which ice crystals are removed to create the porous structures. After the sublimation process, the sample contains alternate layers of ceramic particles and pores. Finally, these freeze-dried samples are sintered to strengthen the porous structure. These steps are schematically shown in Fig. 2.8.

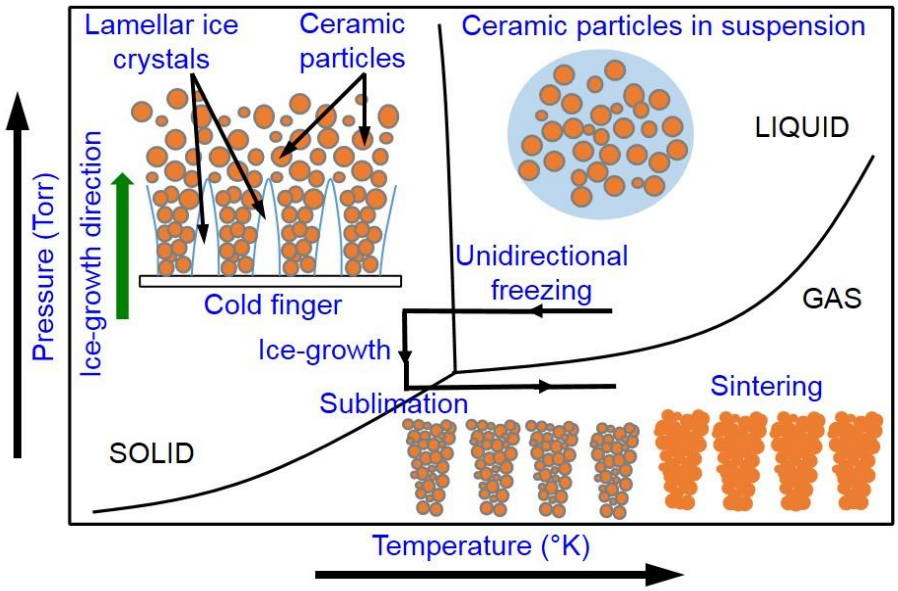

Fig. 2.8 *Schematic of various steps involved in the ice-templating process [162].*

2.5 Direct foaming method

In the direct foaming technique, a ceramic suspension is first foamed by introducing gas bubbles into the suspension. Next, the suspension is polymerized to retain the porous architecture induced through gas bubbles, followed by demolding, drying, and sintering in order to develop a porous ceramic structure. Finally, the sintered foams are glazed to improve

the mechanical properties. This technique focuses on introducing gas bubbles into ceramic slurries to prepare ceramics that are porous. Fig 2.9 schematically shows the various steps of the direct foaming technique. In general, this technique can produce highly porous green bodies that are relatively stronger and can withstand forces during machining. The porosity of the resultant foams depends directly on the amount of gas supplied to the suspension during the foaming process. In contrast, the stability of the wet foam dictates the pore size. Two different methods are employed for the stabilization of the wet foam. One utilizes biomolecules such as proteins, liquids, and surfactants, which are adsorbed on the surfaces of the gas bubbles thereby decreasing the interfacial energy between gas and media, thus preventing the coalescence of the gas bubbles. However, the stabilization through surfactants lasts only several minutes, whereas protein stabilization can last several hours. The other effective method to stabilize the wet foam is to utilize ceramic particles with modified surface chemistry to enhance the ability of the particles to adsorb the long-chain amphiphilic molecules on the surface. Such a process has been observed to stabilize the foamed ceramic suspensions for several days [31]. Fig 2.10 shows typical microstructures of ceramic foams developed using the direct foaming technique [163–165]. The direct foaming technique provides a relatively fast and environmental-friendly way to produce cellular ceramics with a wide range of porosity. Due to defect-free cell struts, cellular ceramics fabricated by the direct foaming technique tend to be relatively stronger than those manufactured by the replica method [27]. In this method, ceramic or precursor solution is foamed with physical or chemical blowing agents such as volatile liquids for stabilized foam production, dried and subsequently sintered for the production of macroporous ceramics. The final porosity of porous ceramics developed by this technique is calculated by the gas's quality incorporated in the suspension during the foaming process. Despite its benefits over the replica process, the pore size is also one of its disadvantages since it is challenging to manufacture ceramics with a small pore size distribution. Otherwise, the pore size is strongly influenced by the wet foam's stability before setting [111]. Destabilizing processes raise gas bubbles by coalescence and result in large pores of final porous ceramic. It is then essential to regulate the bubbles in the wet foam [31].

Here, we only address the surfactant with long chains and biomolecules identified as amphiphilic molecules. The surface of gas bubbles will absorb it and decrease the interfacial energy between suspension and gas, thus slowing coalescence. The foaming technique is a quick and straightforward, environmentally safe way to prepare porous ceramic with more porosity. Many efforts to develop this method have been made. On the other side, Tomita et al.

utilized mechanical approaches to prevent harmful ingredients while utilizing surfactants. Pradhan and Bhargava applied sucrose (improve foam stability) to the ceramic suspension to minimize the brittleness of green bodies [111].

Lyckfeldt et al.[142] established a unique forming method for porous ceramics. As both a consolidator/binder and pore former, starch was used. In wet conditions, various porous alumina components were fabricated and de-molded. The sample porosity was considered to be in 23-70% range, but the samples exhibited outstanding mechanical properties.

Han et al. [166] researched the manufacture of highly porous ceramics with regulated pore structure by foaming and agar gelling. The foaming phase was caused by the forming of macropores and window pores, and by adding agar, the formation of micropores was encouraged. However, the macropores and window pores' scale decreased as agar content increased. There was also a narrower size distribution of macropores in the ceramic foams prepared with higher agar content due to faster stabilization of foams through more rapid gelation.

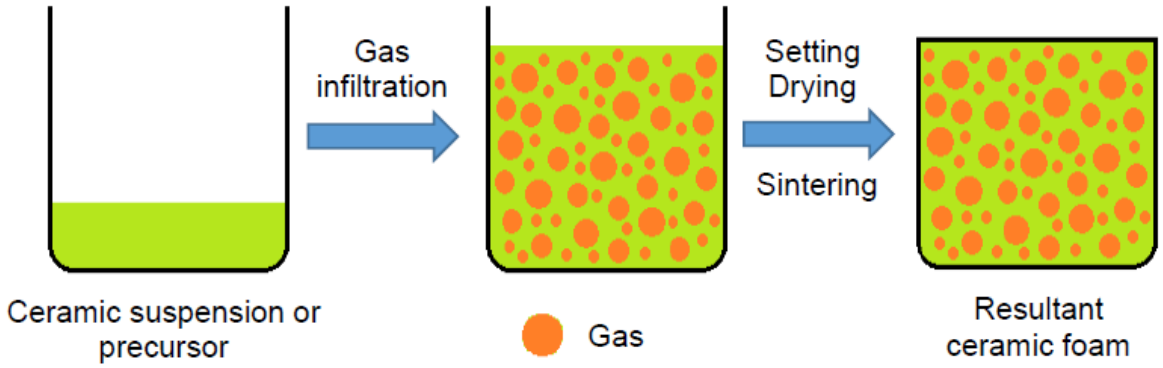

Fig 2.9 *Production of ceramics by using direct foam technique [17].*

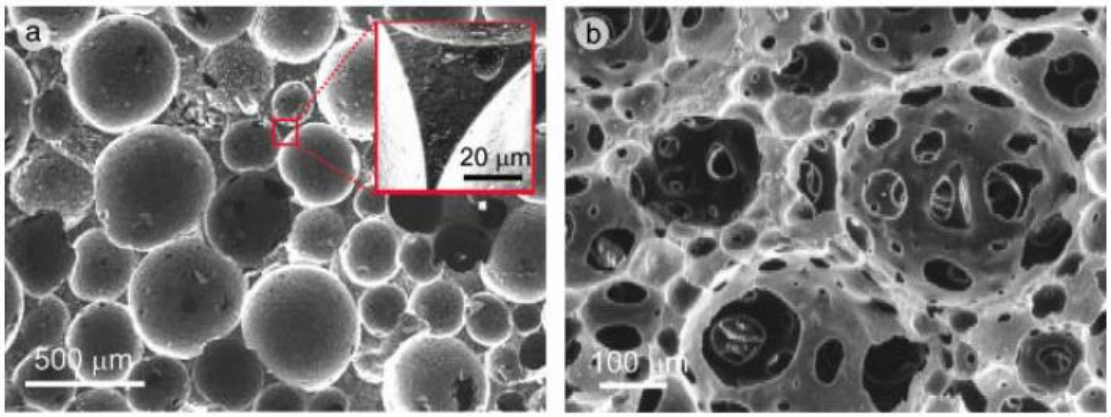

Fig 2.10 Representative microstructures of (a) closed-cell and (b) open-cell ceramic foam fabricated employing the direct foaming technique *[163,165]*.

2.6 Paste extraction

Paste extrusion is a conventional technique generally employed to manufacture honeycombs mainly used for catalysts and filters. In this technique, a paste of ceramic powder, binders, and a lubricating agent is prepared using high-shear mixing. An extrusion ram forces the paste through a die, resulting in an extruded product of the desired shape, which can be further molded into the required shape and length. It is considered a classical route and is used to produce honeycombs for various applications, such as filters. The first paste should be prepared by high-shear mixing and utilizing this technique, so specific components such as ceramic powders with lubricant agents are required. After mechanical extrusion, the green body is produced, followed by heat treatment for drying, debinding and densification. An example of the Honeycombs achieved by this strategy is provided in this document. A schematic representation of the paste extrusion process in shown in Fig. 2.11(a). Next, the extruded green bodies go through a typical ceramic processing route of drying, binder burnout, and sintering to produce the final macro porous ceramics [31]. The main advantage of this technique is that, the honeycomb porous structures can be extruded with unidirectional channels of desired cross-sectional shapes such as square, circular, and triangular [167]. Fig 2.11(b) shows a honeycomb structure produced using paste extrusion process.

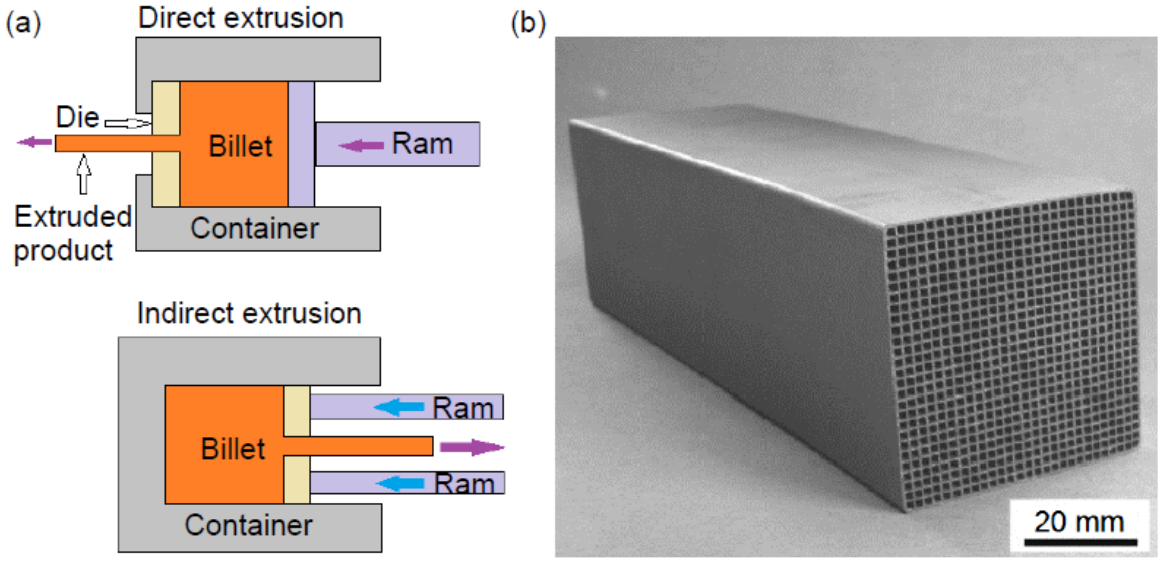

Fig. 2.11 *(a) A schematic of the extrusion process and (b) a honeycomb structure produced using the process [167].*

2.7 Rapid Prototyping method

Rapid Prototyping (RP) technique, also known as solid free-form fabrication, is employed to produce a scaled or full-sized prototype from complex datasets, in which three-dimensional (3D) objects are assembled by point, line or planar addition of the material [168]. Molds or dies which usually carry the ceramic suspension are not required in this processing route. A number of RP techniques are currently commercially available including stereolithography (SLA) [169], selective laser sintering (SLS) [36], laminated object manufacturing (LOM) [170,171], fused deposition modeling (FDM) [172], solid ground curing (SGC), and ink jet printing [171,173]. In all of the RP techniques, 3D architectures are built directly by layer by layer deposition of materials [171]. Fig. 2.12(a) shows a schematic representation of the processing steps involved in rapid prototyping and Fig. 2.12(b) depicts an ESEM micrograph of sample produced by rapid prototyping, revealing smooth horizontal and textured vertical surfaces as well as semi-spherical surface pores. Porous ceramics with both the cellular and periodic structures can be fabricated with a relatively higher level of accuracy in comparison to other fabrication techniques. Compared to all other techniques discussed for fabrication of porous ceramics, a distinct advantage of this is the ability to create highly complex porous architectures with well-controlled pore morphology. However, the manufacturing cost associated with the RP techniques are considerably higher relative to the other techniques [31].

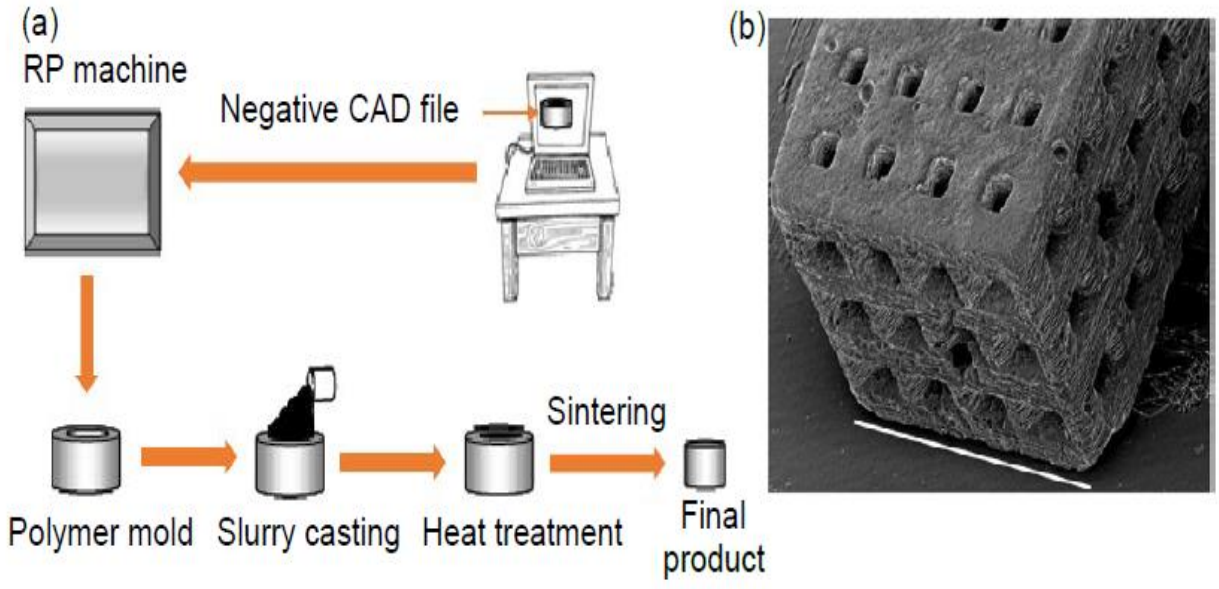

Fig 2.12 *(a) Schematic representation of the steps involved in rapid prototyping for fabrication of porous ceramic parts and (b) SEM micrograph of a typical scaffold processed by RP technique (length of the white bar is approximately 3.6 mm) [174,175].*

2.8 Mechanical behaviour of cellular structures

Properties of foams are influenced by three factors: (i) relative density ($\rho_r = \rho^*/\rho_s$), where ρ^* and ρ_s are the apparent density of the porous structure and constituent material, respectively, (ii) properties of the solid of the porous structure which is generated, and (iii) the topology (connectivity) and shape of the cells [32,176–184]. Variation of , constituent material, pore morphology and connectivity strongly affect the properties of porous structures. Total porosity (p_t) of porous structures is estimated as $p_t = (1 - \rho_r) * 100$. Porous structures typically undergo progressive failure at a relatively constant stress and exhibit large compressive strain before complete densification, making them ideal structures for high energy-absorbing applications under impact loading conditions [31]. Typically, porous structures are considered as structures and most of the available materials can be processed into porous structures possessing a porous architecture. As a result, porous structures have been fabricated from various metals, ceramics, polymers, and composites. For example, clay (alumino silicates), alumina (Al_2O_3), silicon carbide (SiC), partially stabilized zirconia (ZrO_2), titania (TiO_2), silica (SiO_2), and glass are commonly employed materials that are utilized for the fabrication of open-cell and closed-cell ceramic foams [62,180,181]. Since porous structures' load-bearing capacity is crucial for most of the applications, the mechanical response of porous structures has been investigated extensively. Fig 2.13 shows the representative uniaxial compressive stress-strain curves of porous structures as well as the critical parameters such as the stiffness (slope of the linear part of the stress-strain curve), peak stress, plateau stress, densification strain, and total energy absorption (area under the stress-strain curve up to densification strain), which are extremely important to understand the load-bearing characteristics of porous structures. For each stress-strain curve, three distinct zones can be observed that are characteristics of porous structures [185–188] (i) an elastic region (ii) a plateau region (plateau stress) up to a large strain value, and (iii) a densification stage. Stiffness, peak stress, plateau stress, and densification strain are strongly influenced by ρ_r. In general, stiffness, peak stress, and plateau stress increase with increasing ρ_r whereas densification strain shows an inverse relationship with (Fig. 2.13). Such variations with ρ_r also significantly affect the energy absorption capacity of porous structures.

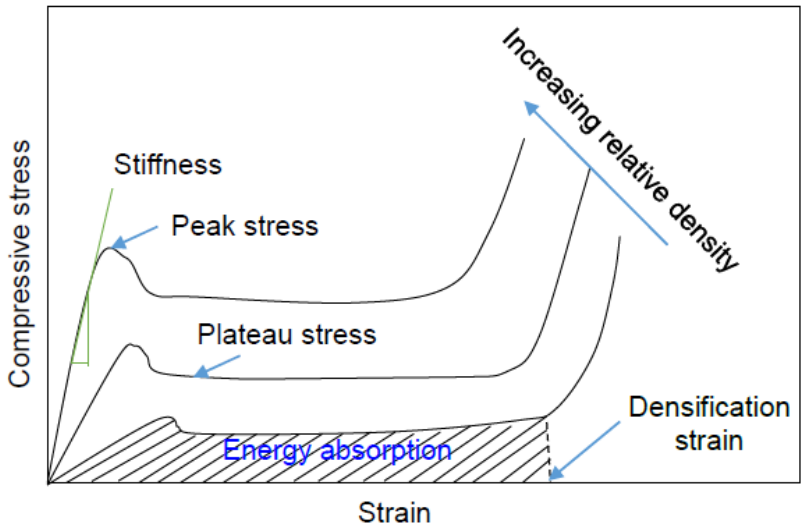

Fig 2.13 *A Schematic of uniaxial compressive stress-strain curves of porous structures with different relative densities [186,189].*

The cell collapse mechanism also relies on the cellular material's relative densities. In elastomeric materials, with a relative density below 0.3, the cell walls buckle elastically. The cell walls yield or crush at higher densities since they are too short and dense to buckle elastically. In the case of metals and many polymer foams, on the other hand, cell wall plastic buckling is true for relative densities of less than 0.3. The cell edges are too small and dense to bend plastically at greater densities; they shear instead. In the end, the flow stress rises rapidly, known as densification to high strains. The cellular solid failure mechanism is shown in Fig 2.14 below.

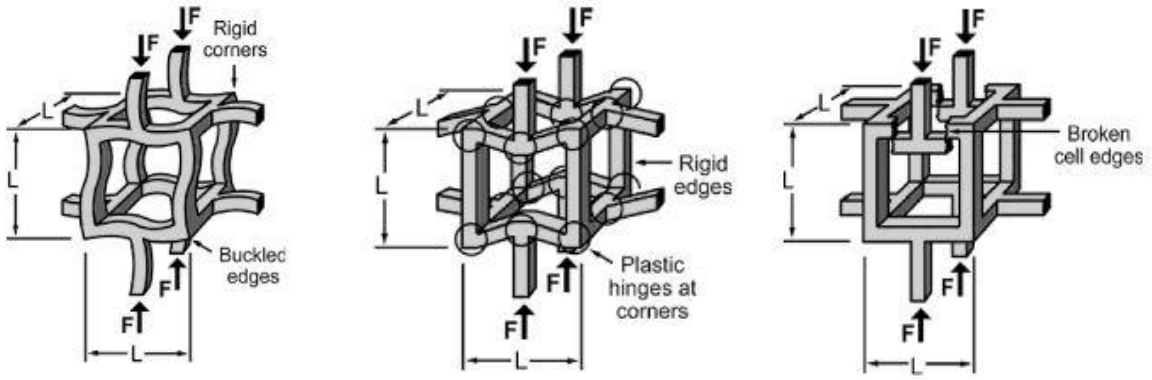

Fig.2.14 *Failure behaviour of cellular solid [190].*

It has also been documented that ceramic foams follow the same stress-strain behaviour pattern. However, cells fail in this situation due to the brittle weakening of the cell walls [191]. The quasi-static fracture behaviour of the porous alumina structure has been compared to that of Al-alloy in a recent analysis. The study emphasized that the densification area is absent in porous ceramic structures because of high strains (almost 25%). Because of their intrinsic

cellular nature, a large amount of energy absorption capacity under compression test is essential for porous structures. The amount of energy absorption capacity under compression is mostly dependent on the cell structure i.e. honeycomb and foams with interconnected 3D structures based on materials used for fabrication (metal, polymer). While choosing a material system for a specific application is often less critical, developing porous structures with the desired microstructure and properties is extremely challenging. This is because for a given material system and porosity, properties are significantly influenced by the type of porosity (open-cell vs. closed-cell), pore connectivity, pore size and morphology, cell wall structure, and pore anisotropy. For example, closed-cell foams typically exhibit better mechanical and thermal properties relative to open-cell foams. Similarly, anisotropic porous structures exhibit improved properties compared to isotropic porous solids. Therefore, the fabrication of porous structures is a complex topic and there is no single processing technique that can address all the microstructure variables which control their properties and performance.

As a result, numerous processing techniques have evolved to develop a wide variety of porous structures with different micro-/macrostructures and properties. A brief description of various techniques employed to fabricate porous structures is provided further. Improved and revolutionary porous ceramic processing has led to personalized microstructural features. Porosity and average pore distribution in a low-density structure may be well regulated to determine the proper combination of strength, low thermal conductivity, large specific surface area, and high permeability [17]. Porous ceramics' final characteristics can be adjusted by regulating the microstructures and the volume fraction for each use. Porous ceramics' processing significantly influences the microstructural properties. The most direct way of manufacturing porous ceramics is to partially sinter powder compacts or sinter powder mixtures, forming pores by reactions to the solid-state [17,142]. Unfortunately, this technique typically indicates a low porosity of porous ceramics (<40 %). In addition to this, several production methods have been developed to satisfy the desired properties' specifications for various applications. Metal and polymer's porous structures have been studied extensively, but porous ceramic structures' data is limited.

There has been a substantial rise in the production and use of highly porous ceramic materials over the past few years. This is primarily due to the material properties provided, such as high permeability, low density, high surface area, low specific heat, and high thermal insulation. For applications such as catalyst substrates or supports, molten metal filters, and refractory furnace linings, thermal insulation, heat exchangers, and in the case of biomaterials, as porous scaffolds, these are the essential aspects. The cell size and its diffusion across the structure also

play a significant role in affecting the structure and mechanical properties. Closed-Porous structures are often used for thermal insulation, and open-porous structures are used as fluid transfer filters and catalyst support. Porous structures' requisite properties often depend on production, and no single route is successful in producing all the structures needed. Thus, various production routes are being developed and patented worldwide.

Amin et al. [192] showed that ceramic foams can be produced using polymeric foam duplication. They claimed that ceramic foam properties greatly influence the density of ceramic slurry. A rise in ceramic slurry density increases the foam's strength and density, making it denser.

Yan et al. [193] find that the ceramic foam's compressive strength depends primarily on the strut's thickness and the foam's relative density. The unstable fracture of ceramic foam struts is due to the weakest frame faults, further contributing to crack initiation and crack propagation.

Han et al. [194,195] reported that the idea was to increase foam strength by adequately regulating the sintering process's temperature. It is possible to examine the impact of foam strength by sintering temperature by discussing three things: shrinkage, porosity, and grain size. The shrinkage of alumina foams greatly improved as the sintering temperatures increased from 1400 to 1600 ^{o}C due to the tiny gaps in the middle of the webs and the alumina particles being close together and touching each other. Owing to this increase in shrinkage, the sintering temperature rose, leading to a reduction in porosity. A lower porosity at 1550 ^{o}C resulted in a higher strength of up to 1.3 MPa. There will be a decrease in porosity even though we sinter at a temperature of 1600 ^{o}C, and there will also be a negligible decrease in compressive strength due to grain growth at this temperature.

Hadi et al. [196] showed that alumina's foam's compression strength can depend on the overall porosity and suspension properties. For corresponding forms of 10, 17 and 27 PPI, compression strengths of 0.7, 1.1, and 1.5 MPa were observed. A considerable improvement in compressive strength can be achieved for alumina foams by decreasing the struts' defects.

Dhara et al. [197] suggested that the most significant parameter affecting the foaming of slurries and the final microstructure of sintered ceramic foams is slurry viscosity. The characteristics of slurries are a high viscosity feature that impacts the microstructure of foams of sintered alumina.

Konopka et al. [198] found that polymerize-urethane elastomer (PNUU) penetration into porous SiO_2 results in a composite that displays a high compression strength and retains large deformations. The ceramic can reinforce the elastomer during cycle filling. On the other hand, the elastomeric presence stops the plastic material from quickly collapsing.

Jens Bauer et al. [199] claimed that one should attempt to increase the strength-to-weight ratio of a substance or lower the density, or both, to improve the strength-to-weight ratio. The lightest solid materials mostly have a drop density of 1000 kg / m^3. Cellular materials, such as foams, can achieve an immense lower density value. They were refining the micro-architecture of the polymer cell structures through 3D laser lithography and alumina layer coating thickness through deposition of the atomic layer on the polymer cell structure leads to ceramic-polymer composites exceeding the compressive strength of all engineering materials with a density far below 1000 kg / m^3. A compressive power of 280 MPa at a density of 810 kg / m^3 results in an optimized honeycomb cellular structure and a 50 nm alumina layer coating thickness.

Colombo et al. [200] claimed that armour systems require composite materials to provide sufficient ballistic protection and weight saving, based on a mixture of different materials of a different nature. A sheet pattern structure was developed and composed of ceramic tiles of armor alumina bound to ceramic foams infiltrated with a polymer. Two types of polymer were used to penetrate the ceramic foams for testing and evaluating an armor device's performance for the first time. The ceramic-polymer composites were manufactured. A significant increase in mechanical properties is seen by the composites made of SiC foams and thermosetting polyurethane (cross-linked). Armour systems based on 6 mm alumina ceramic tiles bonded with SiC polyurethane thermosetting used as backing lead to composites that can resist NATO Ball FMJ bullets for vehicular and structural applications for vehicular and structural applications ballistic and blast safety. NEN NATO Ball FMJ projectiles have not been prevented by elastomeric polyurethane. It cannot be used for ballistic and blast defense systems due to low projectile impact resistance.

Yu et al. [201] reported that polymer interpenetration in the shape of a 3D network, i.e. foam, culminated in a new category of composite materials possessing improved combinations of mechanical and physical properties. The study was carried out on a metal porous polymer composite (MPPC) with an interpenetrating network structure they announced that polymer interpenetrating into the form of the 3D network, i.e., foam, resulted in a new class of composite materials exhibiting enhanced combinations of mechanical and physical properties. The study was carried out on a metal porous polymer composite (MPPC) with an interpenetrating network structure. By infiltrating the polymer in the aluminium foam, aluminium-polypropylene (AI-PE) and aluminium-epoxy resin (AI-Ep) composites were manufactured. Using SEM observation, the composite microstructures were characterized. MPPC 's compressive behaviour and energy absorption properties have been studied in relation to aluminium foams; compared with pure aluminium foam, the composites demonstrate improved compressive

behaviour and enhanced energy absorption ability to build a new Interpenetrating Composite material,

Cree et al. [202] showed how silicon carbide foam infiltrated with aluminium alloy and became composite material. SiC had been vacuum-infiltrated with aluminium alloy A356 in the form of a foam network. Typical fibrous fracturing and brittle cleavage are shown on the matrix fracture surface, while the supporting struts show signs of de-bonding of the layer from the SiC layered structure.

Jain et al. [203] suggested that square cell Cordierite/mullite honeycombs were fabricated using the extrusion method. The honeycomb's mechanical behaviour with and without rubber encapsulation was contrasted with industrial ceramic foam. Interestingly, the foam demonstrated increased energy absorption levels and enhancement in rubber encapsulation's essential stress compared to honeycombs' behaviour.

Peroglio et al. [204] found that foam replication process, alumina scaffolds were sintered. An open-porous structure was accomplished with a porosity of 70 % and a mean pore size of 150 micrometers. SEM studies showed that toughening is caused by the crack bridging of polymer fibrils. Different models and experiments have been conducted to analyse cellular materials' mechanical behaviours and the cell walls' failure behaviour under an applied load to detect and analyse the process of failure of cell walls under load. Material characteristics were examined for cellular structures widely and found in several detailed surveys [205].

2.5 Deformation study by simulation

Early models exist on what a uniaxial elastic activity looks like, but they only considered axial loading for the cell walls [206,207]. Ideally, this may be the optimal scenario. Still, the data is obtained with various instruments in the modern world, which changes how the experimenter collects the elastic properties. Later experiments find that the biological systems experience bending deformations in their walls, and deformation of the cell walls play a secondary function in mechanical building blocks [208–213]. The cells' failure under the influence of uniaxial strain is elastic buckling, plastic yielding, or brittle crushing [1,209,221,222,212,214–220].

Moreover, their exact findings have been verified in experiments on elastic and elastic-plastic honeycombs with a broad variety of geometries [211]. This analysis may be applied to the uniaxial breakdown of papers [205]. Different materials have also been investigated in the context of anisotropic cellular materials in previous research. The cells in a honeycomb system can be organized into three distinct cell geometries. The configuration of such cells and their volume fractions can be monitored by studying geometry and the cell walls' properties [210,211]. The degree of anisotropy in the mechanical properties can be pointed out by

considering the cell's geometry. Harrigan and Mann [223] demonstrated that the form and properties can be derived from anisotropy tensor on the cell's surface. Investigations on the anisotropy in Young's modulus have concluded that it is due to the cell walls' uniaxial deformation [224–226]; this overlooks the significant contribution of the curvature of the cell walls bending. Huber and Gibson [227] studied the influence of the type of anisotropy on the substance's properties in a comprehensive fashion and considered a cell wall's bending. Using a statistical formula, they developed relationships for Young's modulus, elastic-plastic and the hardness stresses, contrasting the measured values with cell structure and mechanical properties. This study looks at the effect of various forms of small "mistakes" in porous structures on the lattice's elasticity. A finite element process analysis was conducted to study the impact of cracks on the modulus of elasticity and yield strength of standard honeycomb. Morphologies with incomplete or broken cell walls were studied for the infinite regular hexagonal honeycomb and the voronoi planar honeycomb [218,221,228,229].

Chapter-3

Materials and Experimental Methods

This chapter supplies details of the raw materials used in this study for fabrication of alumina (Al_2O_3) and zirconia toughen alumina (ZTA) foams and their composites through different fabrication methods, followed by description of different equipments and techniques used for physical and mechanical characterization.

3.1 Raw materials used:

Raw materials used for the preparation of Al_2O_3 foam, ZTA foams and their composite foams are represented in **Table 3.1**. The raw materials of the required quantities were measured using an electronic balance with 0.1mg precision.

Table 3.1 *Raw materials used for the preparation of Al_2O_3 foam, ZTA foams*

Raw material	Chemical formula	Purity	Source
Alumina	Al_2O_3	99.9	Rohini industries, Mumbai, India.
Yitria stabilized zirconia	YSZ	99.5	Alfa Aesar, Russia
Polyurethane foam	$C_{27}H_{36}N_2O_{10}$	-	Rohini industries, Mumbai, India.
Daravan C	$C_3H_4O_2$	99.9	Alfa Aesar, Russia
sucrose	$C_{12}H_{22}O_{11}$	99.9	Loba Chemie, India
Resin	$C_{21}H_{25}ClO_5$	99.5	Loba Chemie, India
Polysterin beads	$(C_8H_8)_n$	99.9	Alfa Aesar, Russia

3.2. Open cell foams

3.2.1Fabrication of alumina and ZTA foams with different PPI levels through sponge replication process

3.2.1.1 Fabrication of Al_2O_3 and ZTA Foams through Dip Coating

Fig 3.1 shows a process flow chart to fabricate alumina/ZTA ceramic foams through dip coating.

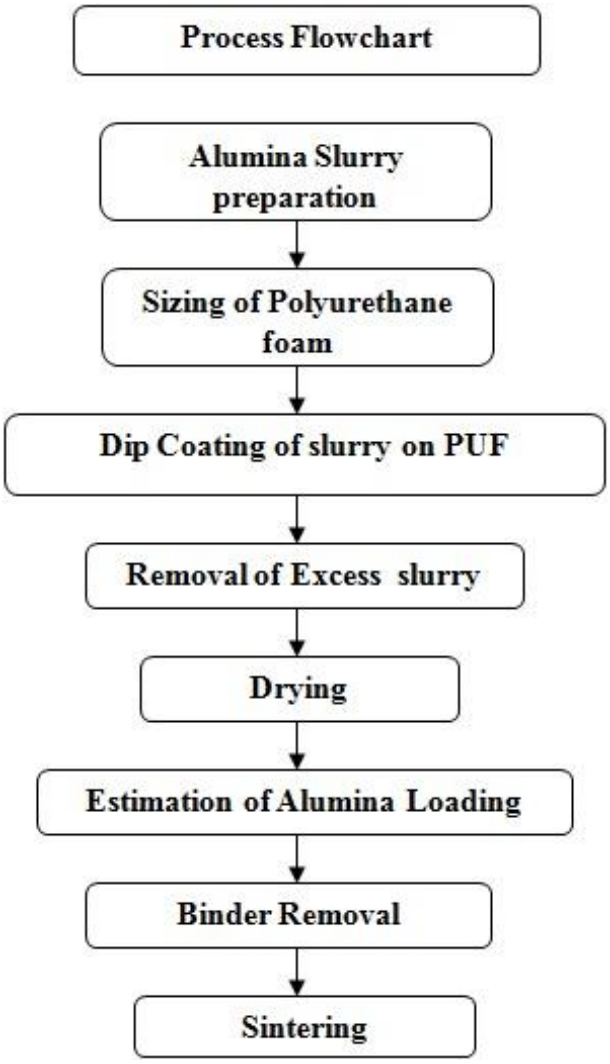

Fig.3.1 *Process flow chart for fabrication of ceramic foam through dip coating.*

3.2.1.1.1 Alumina/ZTA Slurry Preparation

The slurry preparation involves choosing a suitable chemical composition of slurry with the required solid loading (wt%). The solid loading of the slurry is the amount of solid present in the slurry. The formulation of slurry for 55% solid is given in Table 3.2.

Table *Error! No text of specified style in document.**.1** Formulation of alumina/ZTA slurry*

Powder (grams)	De Ionized(DI) water (gm)	Daravan (2% of Powder) (gm)	Methyl Cellulose Ether (2% of Alumina) (gm)
100	81.82	2	2

Alumina/ZTA slurry was prepared as per Table 3.2. Daravan821A is the dispersant to disperse the powder particles uniformly in the slurry, and methylcellulose ether is the binder to provide green strength. Alumina balls were used for mixing the slurry during ball milling. To prepare the slurry, 100 grams of alumina balls were loaded in polypropylene bottles, and DI water was poured along with Daravan 821A. High purity alumina/ZTA powder and Methyl Cellulose

Ether were added and mixed properly without agglomeration. The formulation was pot jar milled for 4hrs to ensure proper mixing and dissolution of methylcellulose ether in slurry. Fig 3.2 shows the pot jar milled used in the present experiment.

Fig 3.2 *Image Pot-Jar milling.*

3.2.1.1.2 Sizing of PUF

Polyurethane Foam (PUF) with 10,20 and 30 PPI (Number of Pores per inch) was cut into the required dimensions considering a shrinkage of 15% after sintering with the help of foam cutting machine, shown in Fig 3.3 The foam after cutting was cleaned in isopropalene alcohol to remove dust etc., before coating.

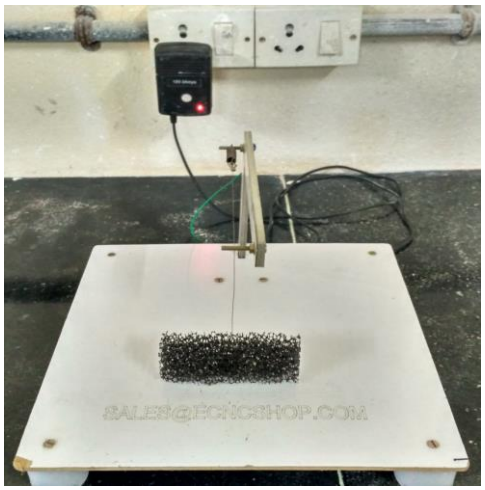

Fig 3.3 *Image of foam Cutting Machine.*

3.2.1.1.3 Coating of PUF with Alumina/ZTA Slurry

The dipping process does the coating. In dip coating, the slurry was taken in the beaker, and PUF was dipped in slurry to ensure the coating of each strut uniformly throughout the PUF. The process was repeated until the foam coated was 10 times the PUF weight.

3.2.1.1.4 Removal of Excess Slurry

After coating the PUF with alumina slurry, the excess slurry must be removed from the foam and this was done in two steps. The first step was that by squeezing the coated foam when excess slurry can be taken out of the foam. In the second step, the compressed air was blown through the polyurethane foam to remove the remaining slurry stuck inside the foam. Fig 3.4 shows the compressor used for blowing compressed air.

Fig 3.4 *Compressor.*

3.2.1.1.5 Drying of Foams

The coated foam was subjected to drying. In the drying process, the moisture content present in the foam was removed by a hot air gun. Fig 3.5 (a) shows the hot air gun used in the present study for drying coated foams.

Fig 3.5 *Drying Equipment a) Hot Air Gun b) Hot Air Oven.*

Final drying of the foams is carried out by keeping the foams inside a hot air oven at 45 ^{o}C for 3 hrs so that further moisture content inside the foam can be taken out. Fig. 3.5 (b) shows the hot air oven used in the present study. Dried foam coated with alumina slurry with solid

loadings of 50%, 55%, 60% estimates for the ceramic formulation for alumina/ZTA coating is shown in Table 3.3.

Table 3.2 *Weight of alumina/ZTA foam with respect to the solid loading*

Solid Loading	Weight of Alumina Coated Foams (gm)	Weight of ZTA Coated Foams (gm)
50%	2.00	4.1
55%	2.54	4.4
60%	2.60	4.5

It is evident from Table 3.3 that by increasing the solid loading of alumina/ZTA slurry from 55% to 60% solid loading, there is not much change in alumina/ZTA loading. Hence 55% of solid loading is considered optimum. Dried foam samples were coated with slurries with solid loadings and their respective alumina/ZTA loading, also as recorded, are shown in Table 3.4.

Table 3.3 *Weight of foams with respect to solid loading*

Solid Loading	Weight of Alumina Coated Foams (gm)	Weight of ZTA Coated Foams (gm)
40%	3.20	4.5
45%	4.17	4.8
50%	4.19	5.2
55%	4.55	5.9

3.2.1.2 Fabrication of alumina ceramic foam through Dip + Spray coating process

Fig 3.6 shows a process flow chart to fabricate alumina ceramic foams through dip + spray coating. In the dip + spray coating process, the first coating of alumina slurry on polyurethane foam was by dip-coating. Polyurethane foam was dipped in alumina slurry with 55wt% solid loading followed by spray coating on an ordinary paint spray gun for spraying the alumina slurry with 45% solid loading. Fig 3.7 shows the ordinary paint spray gun which was used for dip + spray coating process. The excess slurry was removed and dried. The sample was subjected to heating to remove the organics and densify under identical conditions described in the session (3.2.1.2).

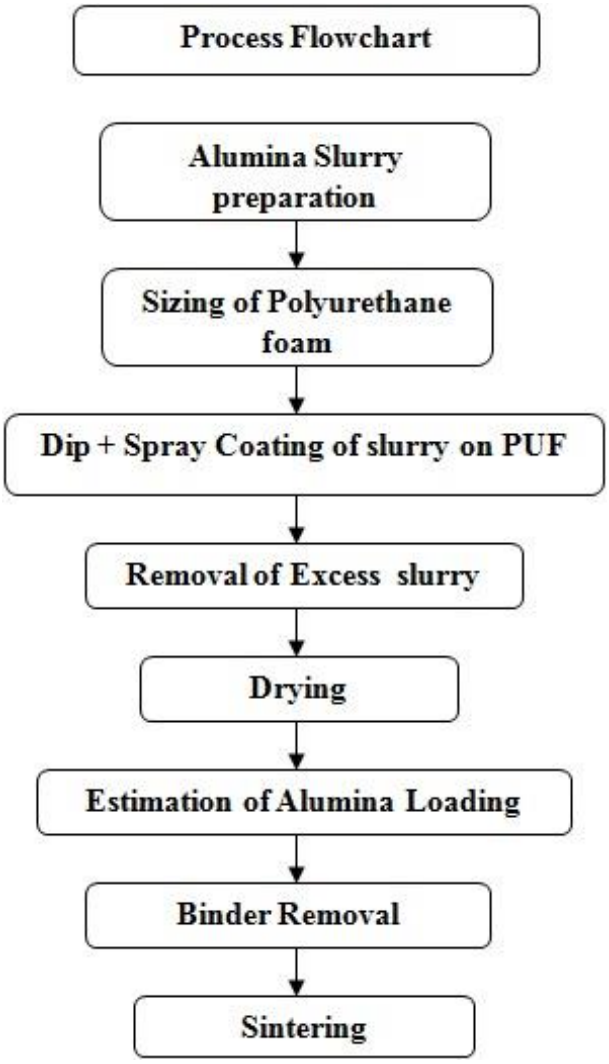

Fig 3.6 *Process Flow Chart For fabrication of alumina foams through dip + spray coating process.*

Fig 3.7 *Spray Coating Gun.*

3.3 Fabrication of Cellular Ceramic Composites

3.3.1 Epoxy Encapsulation of Alumina/ZTA foams

15×15×15 mm^3 notched specimen and unnotched specimens 55×20×20 mm^3 were encapsulated by wrapping the aluminum foil around the ceramic foam to avoid insertion of polymer solution into the pores. During the testing, the effect of aluminum was considered negligible. After wrapping the foam in the foil, the wrapped foams were dipped in polymer solution which consists of epoxy resin and hardener with definite propitiations such as 20 parts of epoxy and 6 parts of hardener by weight. After dipping the foam, it was subjected to 70 ^oC temperature for one and half an hour so that polymerization reaction takes place and forms epoxy encapsulated alumina/ZTA ceramic foam. Fig 3.8 shows the fabrication of epoxy encapsulated foam.

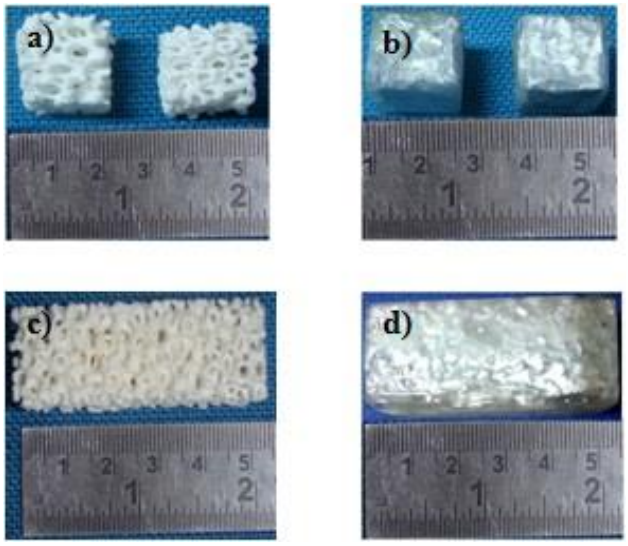

Fig 3.8 *Epoxy-encapsulated foams a) Bare b) Epoxy Encapsulated for Compressive test c) bare foam for Charpy test d) Epoxy Encapsulated for Charpy test.*

3.3.2 Fabrication of Polymer Infiltrated Alumina/ZTA Foams

3.3.2.1 Vacuum Infiltration setup Design

For vacuum infiltrating the alumina ceramic foam, we have fabricated vacuum Infiltration design equipment. A design of vacuum infiltration facility setup was prepared in AutoCAD with the required dimensions. The vacuum infiltration facility mainly consists of a cylinder with a gas septum used to prevent the leakage of air, a foam holder, a glass beaker, and a vacuum pump used for creating the vacuum inside the beaker. A vacuum infiltrator aims to prevent the formation of air bubbles during the polymerization of polymer because of air trapped inside the foam's pores. Fig 3.9 shows the schematic representation of VID Equipment.

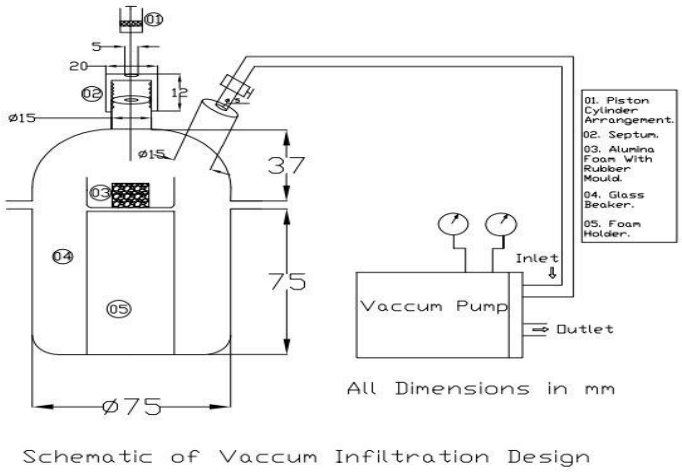

Fig 3.9 *Vacuum Infiltration Design facility.*

3.3.2.2 Vacuum Infiltration of Alumina/ZTA foams

Alumina/ZTA foams were placed within the holder and the polymer solution consists of 20 parts of epoxy and 6 parts of hardener by weight. The polymer was thoroughly mixed without generating bubbles in the syringe. Vacuum generation using the vacuum pump and polymer solution was injected into the foams. Foams of dimensions 15×15×15 mm^3 and unnotched specimens 55×20×20 mm^3 were infiltrated. After infiltration, the vacuum infiltrated alumina foam was placed in the oven at 70 ^oC for one and half an hour in order to effect polymerization. Fig 3.10 shows the vacuum infiltrated alumina/ZTA foams used for compression and Charpy impact test.

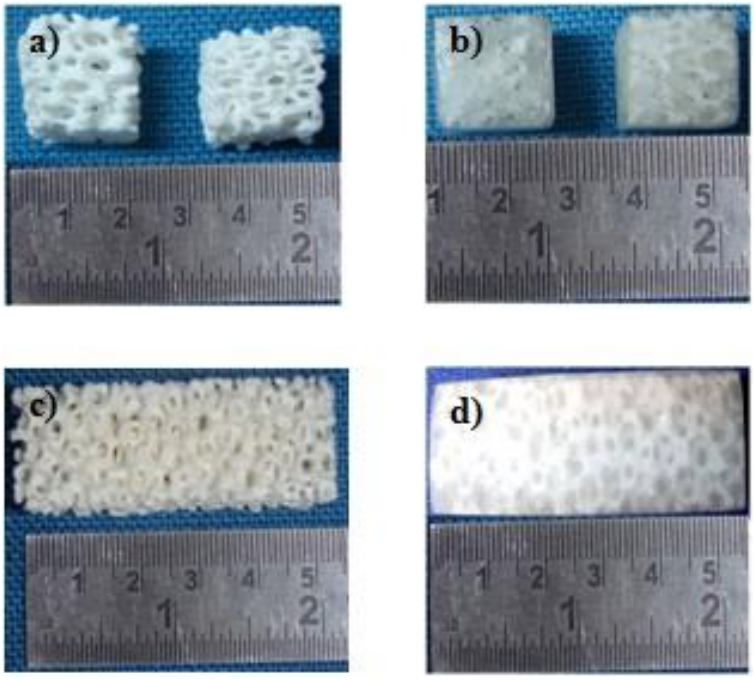

Fig 3.10 *Vacuum Infiltrated foams a) Bare b) Epoxy Infiltrated for Compressive test c) bare foam for charpy test d) Epoxy Infiltrated for charpy test.*

3.3.2.3 Metal Infiltration of Alumina/ZTA foams

Alumina/ZTA foams were placed within a specially designed holder and molten aluminum metal was poured into the foams. Before infiltration of molten metal, simples were preheated to avoid thermal shock failure. Foams with dimensions 15×15×15 mm^3 and unnotched specimens 55×20×20 mm^3 were infiltrated.

3.4 Fabrication of nickel-plated alumina foams through an electrolysis process

Alumina foams were coated with nickel through electrolysis technique. In this process, alumina foam was coated with plasma for obtaining conductivity. Plasma coated alumina sample placed in bath composition shown in Fig. 3.11. Bath composition and processing parameters are shown in Table 3.5.

Fig. 3.11 *Image of an electrolytic cell.*

Table3.5 *Details of bath composition with operating condition*

Details	Values
$NiSO_4 \cdot 6H_2O$+ $NiCl_2 \cdot 6H_2O$ concentration (gm/l)	350
Boric acid concentration (gm/l)	20
Sodium sulphate (ml/l)	15
Omni additive (ml/l)	992:8
Magnum brightener (ml/l)	437:10
Operating Conditions	
Current (Amp):	7-8.5
Voltage (V):	10-12
Deposition Rate: µm/min	2.85

3.5 Thermo foaming method for fabrication of Alumina/ZTA foams

The Al_2O_3/ZTA powder to sucrose weight ratios ($W_{P/S}$) was mixed in a pot jar mill in acetone medium for 5h using zirconium balls as grinding media. Alumina/ZTA powder to sucrose

weight ratios, powder mixture to acetone, and sucrose to zirconia balls weight ratios are shown in Table 3.6. The mixed slurry (Alumina/ZTA powder + sucrose + acetone) was poured in 2-liter borosilicate glass trays and heated at 185 ºC in a hot air oven for the sucrose to melt. Powder dispersed molten sucrose was appropriately stirred with a glass rod for homogenous mixing of Alumina/ZTA powders in sucrose melt. The Alumina/ZTA powder dispersed molten sucrose was heated at different temperatures ranging from 120 ºC- 180 ºC for foaming and setting.

Table 3.6 *Weight ratio values of powder to sucrose, powder mixture to acetone and powder mixture to zirconia balls*

Details	Weight ratio
Powder to sucrose weight ratio ($W_{P/S}$)	0.6-1.4
Powder mixture to acetone	1:3
Powder mixture to zirconia balls	1:6

3.6 Closed cell foams

3.6.1 Uniaxial compaction for fabrication of closed cell foams

Polystyrene beads of different sizes (10,20 and 40µm) were added to Al_2O_3/ZTA powder with different volume fractions. The powder mixture was compacted to cylindrical pellets of different diameters (10 mm to 20 mm) at a pressure of 600 MPa using compaction dies and a uniaxial hydraulic press shown in Fig.3.12. Zinc stearate was applied to the die walls as a lubricant to reduce the die wall friction and 1 wt. % PVA (Poly Vinyl Alcohol) solution was added to the powder before compaction as a binder to increase the green strength of the pellet.

Fig. 3.12 *Uniaxial hydraulic press.*

3.6.2 Sintering of compacts

Fabricated foams were sintered in a box-type electric resistance furnace equipped with $MoSi_2$ heating elements (OKAY, Bysakh & Co., India) shown in **Fig.3.13.** Initially, samples were heated to 550 °C with a slow heating rate of 1 °C/min and 30 min holding was provided to remove organic removal, then the remaining schedule was carried out at a heating rate of 5 °C/min.

Fig. 3.13 *Box type electric resistance furnace.*

3.7 Characterization methods used

After sintering, samples were subjected to physical, phase, microstructural, and mechanical characterization. The details of the characterization techniques and equipment used are discussed below

3.7.1 Physical characterization

3.7.1.1 Density measurement

Sintered density of the foams was calculated from Archimedes principle as per ASTM C373 procedure using. A balance with density measuring kit (LA 120S, Sartorius AG Germany). The initial weight of the samples was first taken in the air (Dry weight) followed by boiling in distilled water for 1 hour and cooled to room temperature for 2 hours. The saturated weight was measured immediately and the suspended weight was measured in water accurately. The sintered density and foam density were calculated using equations (1) and (2), respectively. The density measurement setup is shown in Fig.3.14.

$$\text{Sintered Density} = \frac{\text{Dry weight}}{\text{saturated weight} - \text{suspended weight}} \qquad (3.1)$$

$$\text{Foam Density} = \frac{\text{Weight of foam}}{\text{volume of foam}} \qquad (3.2)$$

Fig.3.14 *Density measurement setup*

3.7.1.2 Particle Size Analysis by Dynamic Light Scattering

Fig 3.15 shows the Photon Correlation Spectroscopic measuring method was used to identify the particle size of powders. The velocity of moving particles diffusing owing to Brownian motion is the basis for Photon Correlation Spectroscopy. Brownian motion is the uneven movement of particles in liquid media caused by inter-particle collisions. This results in a Rayleigh scattering spectrum with a line width T (defined as the half-width at half-maximum) proportional to the particle diffusion coefficient D:

$$T=DK^2 \qquad (3.1)$$

Where $k = \sin(\theta/2)(4\pi n/\lambda)$, λ the laser wavelength, n is the refractive index, and θ the scattering angle. Assuming the particles are spherical and non-interacting, the mean radius 'r' can calculated from the Stokes-Einstein equation,

$$D = \frac{K_B T}{6\pi\eta r} \qquad (3.2)$$

KB-Boltzmann constant, D – Diffusion coefficient, T-absolute temperature, r –radius, and η – Coefficient of viscosity of the medium.

Fig 3.15 *Image of Particle Size Analysis.*

3.7.2 Phase and microstructure analysis

3.7.2.1 X-ray diffraction analysis

Phase analyses of the as-received powders were performed by x-ray Diffractometer (XRD: X'Pert PRO, PANalytical, The Netherlands) shown in Fig. 3.16. Diffraction peaks were obtained using CuKα radiation (wavelength λ = 0.15406 nm) operated at 45 kV, 30 mA, taking a step size of 0.02°. The patterns were then analyzed using X'Pert Highscore Plus (PANalytical, The Netherlands) software for phase identification and quantification equipped with ICDD (International Center for Diffraction Data) and ICSD (Inorganic Crystal Structure Database). The as recorded XRD profiles were normalized to 100% in each case. The background correction as well as $K\alpha_2$ strippings using Rachinger's method was performed prior to the phase analysis using a search-match program with ICDD-PDF4+ database. Identification of a crystalline phase was based on a comparison of the observed d-spacing and relative intensities with those of a reference material pattern compiled in the ICDD database.

Fig. 3.16 *X-ray diffractometer used for phase analysis.*

3.7.2.2 Microstructural analysis

The microstructure of the samples was examined with a Scanning Electron Microscope shown in **Fig. 3.17** with a tungsten filament electron source (SEM: VEGA 3LMV, TESCAN, Czech Republic) using Secondary Electron (SE) and Back Scattered Electron (BSE) imaging modes. Before observing SEM, the samples were sputter-coated with an ultra-thin coating (2-8 nm) of electrically conductive gold/palladium. Sputter coating makes the sample surface conductive and prevents the charging effect. The cellular structure samples were placed inside the vacuum chamber to record the stud and microstructure images at different magnifications.

Fig.3.17 *Scanning Electron Microscope.*

3.7.3 Thermo Gravimetric – Differential Thermal Analysis (TG-DTA) of PUF

Thermal analysis is a group of techniques that measure the physical property as a function of temperature while the material is subjected to a controlled program Fig 3.18 shows the TG-DTA Equipment. The thermal gravimetric analysis (TGA) and the differential thermal analysis (DTA) investigate the thermal characteristics of materials. TG is a quantitative technique for measuring weight change with respect to time and temperature due to decomposition or dehydration. TG curves are characteristic curves for a given compound because of the unique sequence of physico-chemical reactions, which happens over a fixed temperature range and at rates expressed as a molecular structure-function. Weight changes result from forming or rupturing various physical or chemical bonds at higher temperatures, leading to volatile or heavier reaction products. The data obtained from such curves concern the kinetics and thermodynamics of the various chemical, intermediate and final reaction products. The temperature range of temperature usually is from ambient to 1500 ^{o}C with an inert atmosphere. The sample is commonly heated under a controlled atmosphere (nitrogen or argon) with a

constant heat input rate, while the difference in mass during this process is recorded. A mass loss indicates that degradation and mass gain indicates oxidation. The DTA device is used to compare sample and reference temperatures. In a furnace, a sample and a control are arranged symmetrically. The difference in temperature between the sample and the reference is measured by two thermocouples, one of which is in contact with the specimen holder's bottom (also called the crucible). The other is in contact with the underside of the reference holder. When a thermal event occurs in the sample, a temperature difference will be generated. An endothermic event makes the sample temperature lower than the reference temperature that follows the heating program closely. On the other hand, an exothermic event makes the sample temperature higher than reference temperature.

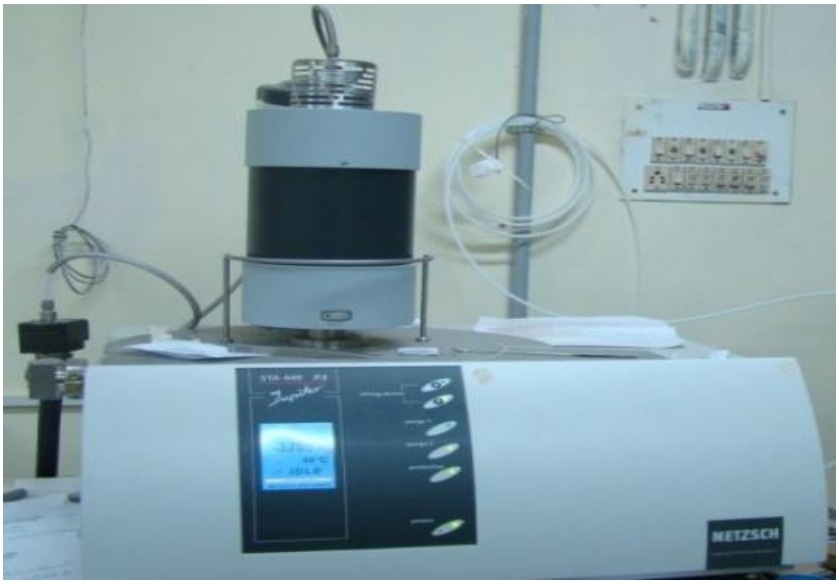

Fig 3.18 *TG-DTA equipment.*

3.7.4 Mechanical properties evaluation

Mechanical properties such as compression test, 3-point bent test and impact properties of sintered samples were analyzed as described in the following sections:

3.7.4.1 Compression Test and 3-point bent test

Under static condition, the compression test and 3-point bent test were performed on all foams using Universal Testing Machine (UTM). Fig 3.19 shows the UTM. The UTM consists of upper and lower flat steel plates. Where the upper flat steel plate is connected to the ram and the ram moves up and down. The lower flat steel plate is fixed. The sample was placed between two flat steel plates. The compression test was performed with a ram speed of 0.5 mm/min corresponds to the strain rate of 1.66×10^{-3} S^{-1} maintained during the test.

Fig 3.19 *Universal Testing Machine.*

3.7.4.2 Charpy Impact Testing of Foams

All the fabricated foams were characterized to evaluate the energy absorption values at higher strain rates (10^2 to 10^4 S^{-1}). The sample dimensions of 55×20×20 mm^3 were prepared. The machine used for performing impact tests is illustrated schematically in Fig 3.20. The load is applied as an impact blow from a weighted pendulum hammer released from a fixed height h. The drop angle of a pendulum for Charpy is 140^o. Also, the initial potential energy for Charpy is 300 joules with a least count of 2 Joules.

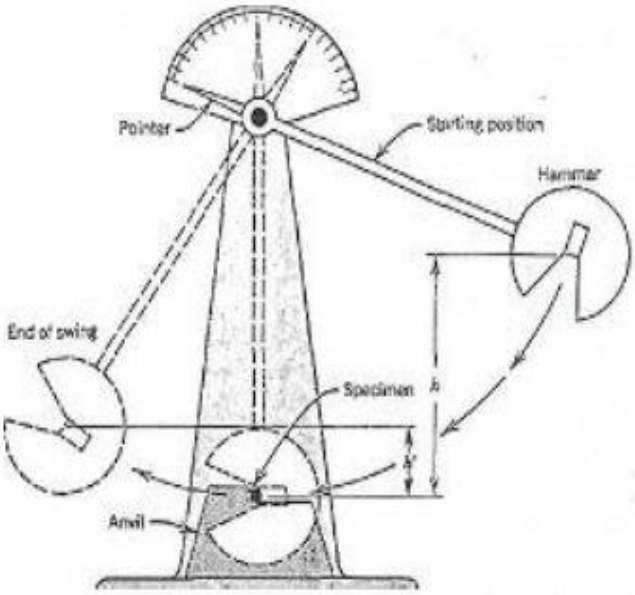

Fig. 3.20 *Charpy Impact Testing.*

3.7.5 X-ray tomography

The micro-CT technique generally consists of many phases, including (i) specimen preparation and mounting, (ii) scanner setup and parameter selection, (iii) scanning operation, (iv) image reconstruction, and (v) image visualization. On a translation and rotation stage, alumina samples were placed between the source and the detector to be scanned. The sample must be rotated in order to be imaged at multiple angular locations. Translation (in the axis of the beam) allows control of the distance between the sample and the source, which in turn controls the size of the image that is projected onto the detector for successful scanning of the sample, the below steps were followed to construct a CAD model.i.e.scanning the specimen in Micro-CT, reading DICOM images, thresholding, converting the images to STL file, STL to CAD model, and performing Finite Element Analysis.

Open-cell Foams Prepared Through Sponge Replication Method

This chapter mainly deals with the fabrication of alumina and alumina stabilized zirconia (ZTA) open-cell foams through a polymeric sponge replication process with different pore sizes. In this method, polyurethane foam is used as a template. The foams were fabricated with different PPI (Pore per linear inch), i.e.,10PPI, 20PPI, and 30PPI. Fabricated foams were infiltrated and encapsulated with polymer and metal for cellular composite materials. The effect of cellular properties (pore size, density, strut thickness) and composite effect on physical and mechanical properties alumina and ZTA were also described. The fabricated foams were sintered at optimized conventional sintering schedules. The details of the characterization techniques used are described in chapter 3.

Fig 4.1 shows the process flow chart to fabricate alumina and ZTA foams through dip coating, dip+spray coating.

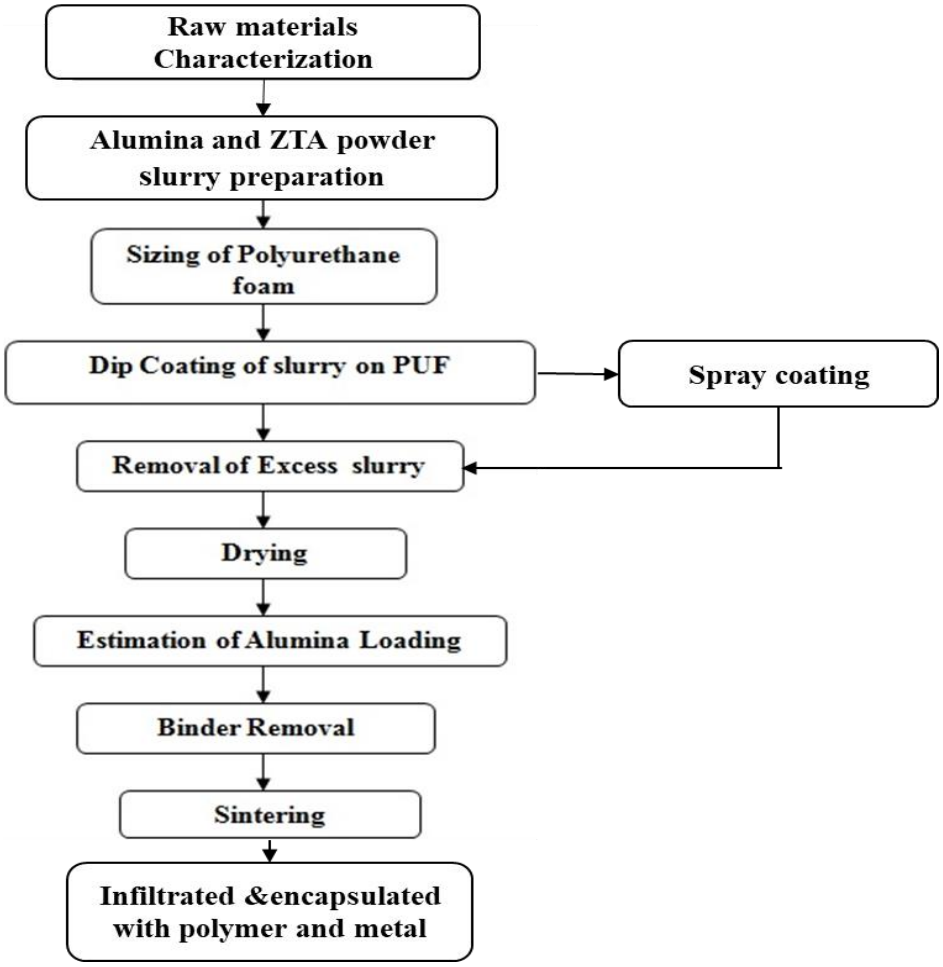

Fig 4.1 *Process flow chart for fabrication of ceramic foam.*

4.1 Raw materials characterization

4.1.1 Powder characterization

Fig 4.2 shows the SEM images of alumina and yttria-stabilized zirconia (YSZ) powder. Particle size distribution curves of as received and alumina and YSZ were shown in Fig 4.3. The average particle size of alumina and YSZ powders are 296 nm and 300nm, respectively.

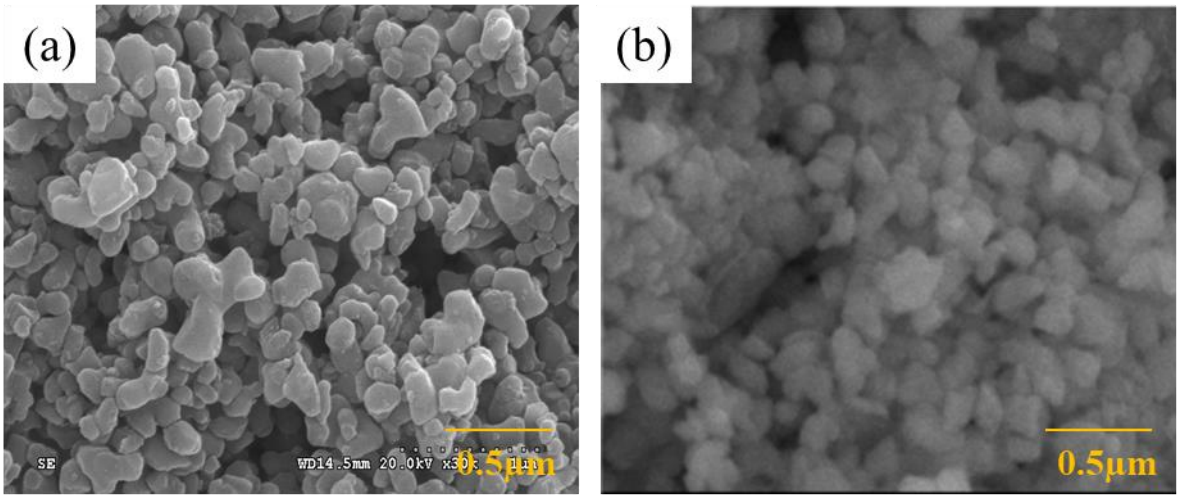

Fig. 4.2 *SEM images of a) alumina b) yttria-stabilized zirconia (YSZ)*

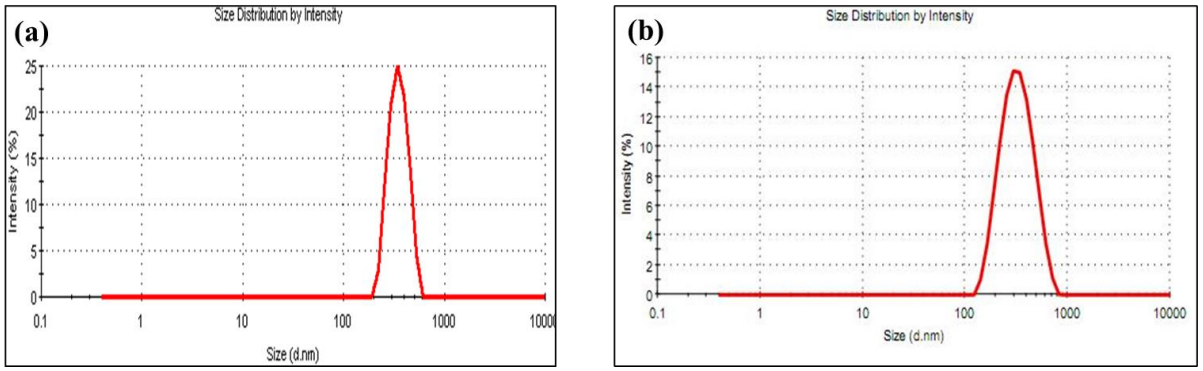

Fig 4.3 *Images of Particle Size Analysis curves a) alumina b) YSZ.*

4.1.2 Phase analysis

The X-ray diffraction patterns of as-sintered Al_2O_3 and ZTA forms are presented in Fig. 4. The analysis of XRD patterns revealed that Al_2O_3 powders contains only α -Al_2O_3 phase (ICSD: 98–003-2923) and ZTA contains tetragonal zirconia phase (ICSD: 98–003-0698), monoclinic zirconia phase (ICSD 98-007-1839), and α -Al_2O_3 phase (ICSD: 98–003-2923) as indexed in Fig. 4.4.

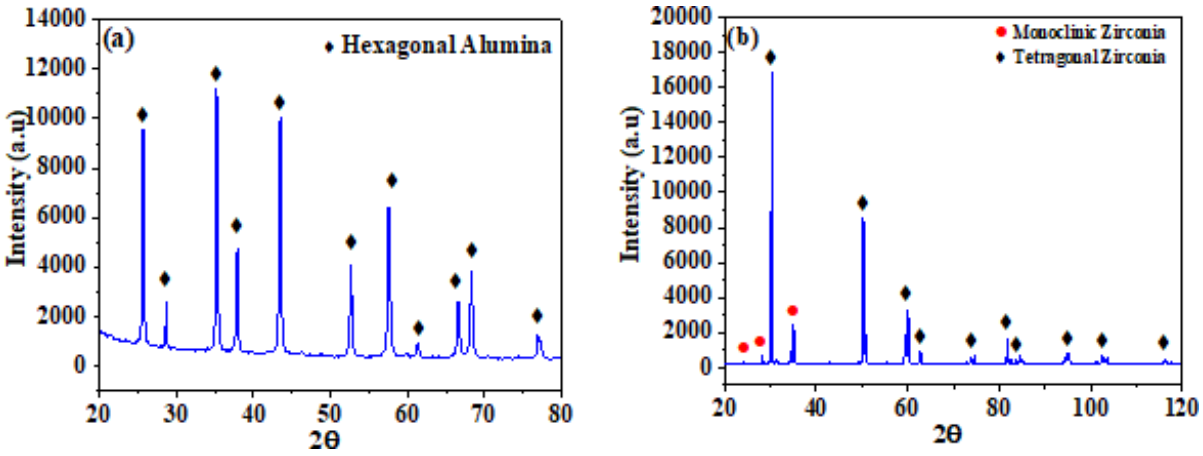

Fig. 4.4 *XRD analysis of a) alumina b) yttria-stabilized zirconia (YSZ).*

4.1.3 Characterization of Polyurethane Foam (PUF)

The cellular structure of PUF was studied by scanning electron microscope (SEM). PUF strut and cell size were recoded at different magnifications. The images are shown in Fig 4.5. It is evident from the SEM micrograph that the structure of the cell can be considered a random distribution of 3dimensional polyhedral cells.

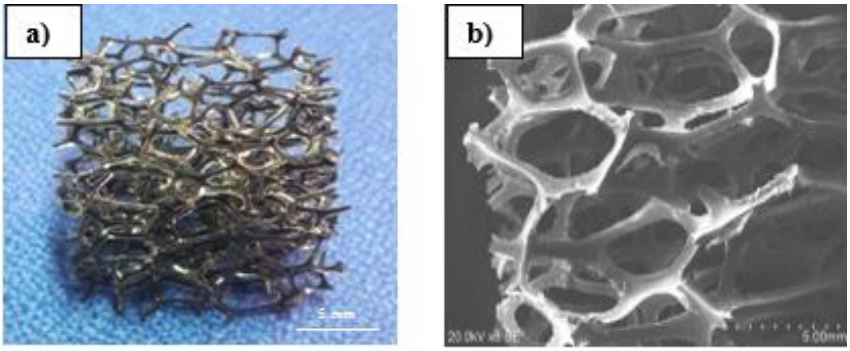

Fig 4.5 *Images of PUF a) PUF b) Scanning Electron Microscope Image of PUF.*

4.1.3.1 Cellular Properties

The cellular properties such as cell diameter, strut thickness, and distance between two adjacent cells can be measured using image analysis software. All cellular properties are determined and tabulated in Table 4.1.

Table 4.1 *represent the cellular properties of polyurethane foam*

Foam condition	Cell diameter (mm)	Strut thickness (mm)	Distance between two adjacent cells (mm)	Density (gm/cc)
10 PPI	3.49	0.50	2.73	1.20
20PPI	2.3	0.4	2	1.20
30PPI	1.9	0.36	1.1	1.20

4.1.3.2 Thermo Gravimetric – Differential Thermal Analysis (TG-DTA) of PUF

Thermal analysis is a group of techniques that measure the physical property as a function of temperature while the material is subjected to a controlled program. The thermal gravimetric

analysis (TGA) and the differential thermal analysis (DTA) investigate the thermal characteristics of materials. Fig 4.6 shows the TG –DTA Curves of PUF.

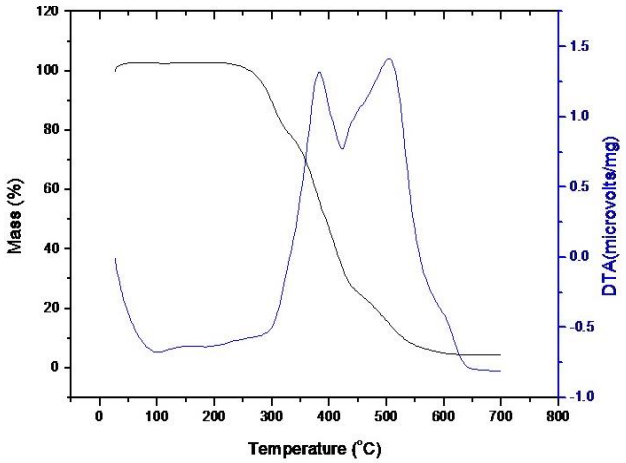

Fig 4.6 *TG –DTA Curves.*

TG/DTA plot of the PUF is shown in **Fig. 4.6.** It is evident from the TG plot that weight loss is started at around 260 °C and proceeds through major thermal exo events indicated by two broad DTA peaks leading to the complete loss in the range of 550-600 °C. This corresponds to the thermal degradation of the urethane structure which is the inherent chemistry of polymeric foams [25]. As decomposition of the polymer occurs through the formation of mainly gaseous products, a lower heating rate is preferred to avoid the sudden release of gaseous products, creating stresses in the alumina coatings leading to minor cracks. However, a longer soaking time will ensure reaching equilibrium to ensure close to complete loss of organic formulations. An optimum heating schedule followed in the current study is depicted in **Fig. 4.7.**

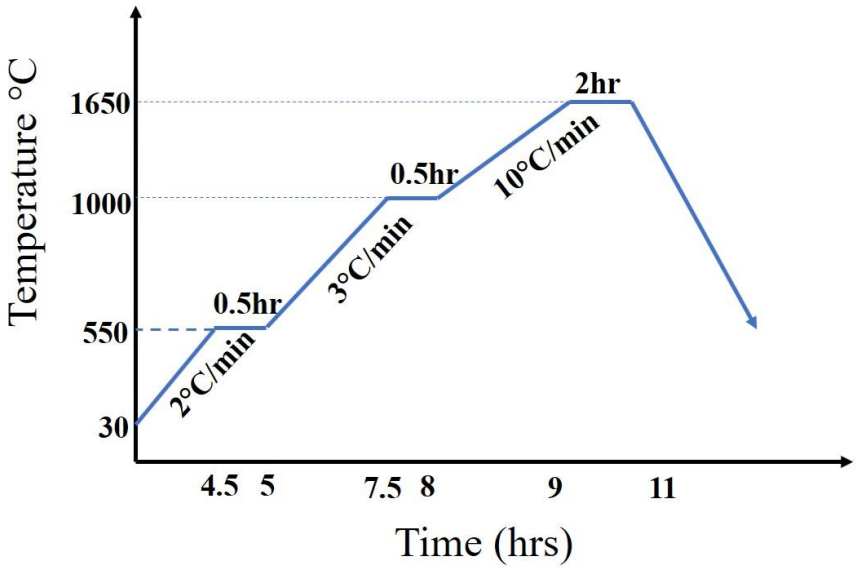

Fig 4.7 *Sintering schedule for alumina and ZTA.*

4.2 Slurry preparation

The slurry preparation involves choosing the right chemical composition of slurry with the required solid loading (wt%). Solid loading of the slurry is the amount of solid present in the slurry. The formulation of slurry for 55% solid is given in Table 4.2.

Table 4.2 *Formulation of alumina slurry*

Powder (grams)	De Ionized(DI) water (gm)	Daravan (2% of Alumina) (gm)	Methyl Cellulose Ether (2% of Alumina) (gm)
100	81.82	2	2

4.2.1 Viscosity measurement

Viscosity measurement of alumina and ZTA powder suspension with a solid loading of 55% is depicted in Fig.4.8. The viscosity vs shear rate plot shown in Fig. 4.6 shows that it isn't easy to achieve percentage loading on the foam and a uniform coating. The slip has exhibited a pseudoptotic behaviour in the lower shear rate. Shear-thinning behaviour is preferred for retaining the slip on the polymer studs after coating and thixotropic over a period to adhere uniformly while the excess slip is removed. This can be attributed to the optimized binder (2 wt% methylcelluloses) and dispersant (Darvan 821A, 2wt%) concentration which added to the slip formulation and ball milling process.

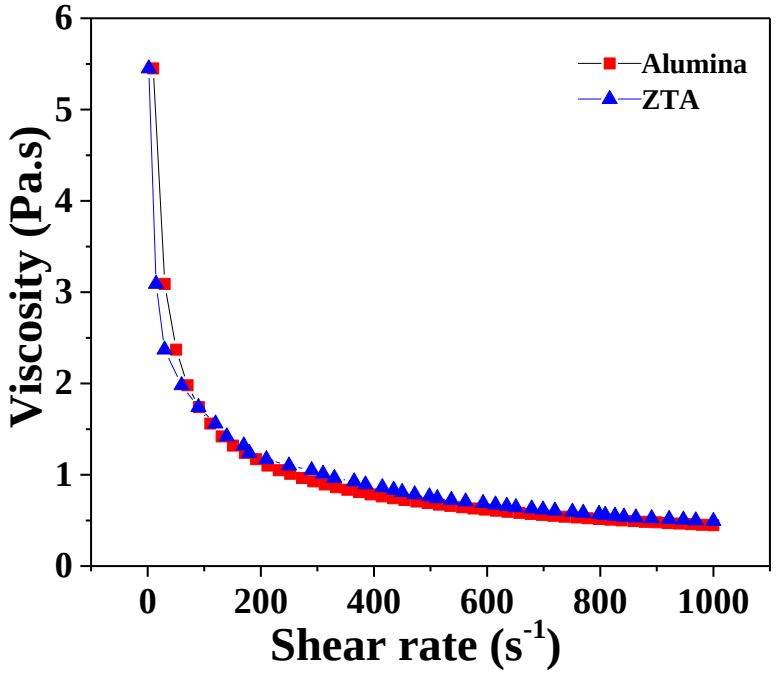

Fig.4.8 *Image viscosity vs. shear rate.*

4.3 Microstructure and mechanical properties

4.3.1 Microstructure characterization of bare foams

The sintered alumina ceramic foam derived from polyurethane foam is depicted in **Fig 4.9 (a)-(c).** Dip+sparay coated foam having a higher strut thickness with uniform coating than dip-coated foam. The dip + spray coating process was adopted to fabricate all the foams to achieve superior properties. **Fig. 4.9 (d) –(f)** shows the SEM images of dip+sparay coated 10PPI, 20PPI and 30PPI alumina foams taken at different magnifications and analyzed. In dip-coated alumina foam, strut shows non-uniformity with strut thickness, and dip+sparay coated alumina foam offering a uniform coating than dip-coated foam.

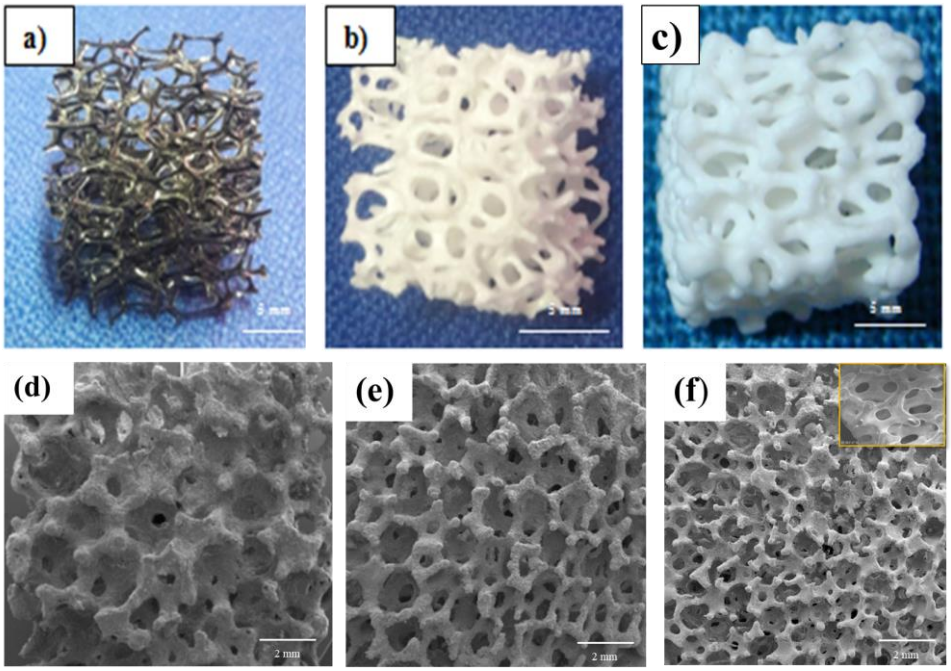

Fig 4.9 *Images of a) PUF b) Sintered dip-coated alumina foam c) Dip + Spray coated foam d) SEM image of 10PPI foam e) SEM image of 20PPI foam f) SEM image of 30PPI foam.*

4.3.2 Mechanical characterization

All the fabricated foams were characterized under static and dynamic conditions to evaluate their mechanical properties. Fabrication of bare and composite foams (infiltrated & encapsulated with polymer and metal with different PPI levels) is discussed in chapter 3.

4.3.2.1 Compression Test

Figs. 4.10 and Fig 4.11 (a)-(c) shows the stress-strain compression behaviour of bare, encapsulated, and infiltrated Al_2O_3 and ZTA foam samples, respectively. All the samples were tested at a strain rate of 0.003 s^{-1} at room temperature. Al_2O_3 and ZTA foam showed the same failure behaviour; all the mechanical values are listed in **Table. 4.3**. The fracture proceeds by breaking weaker struts by stress concentration without focusing on any distinct region, leading

to failure as in a typical porous ceramic sample. However, due to the foam's cellular nature, several kinks extend the energy absorption region. 10PPI foam shows higher compressive values than 20PPI and 30PPI due to increased strut thickness in 10PPI foams. Fig 4.11 shows the stress-strain curves of encapsulated and infiltrated foams with polymer/metal. Al_2O_3 and ZTA. On encapsulation, there was a substantial increase in compressive strength when compared to bare foams. This can be attributed to the uniform distribution of stresses due to the epoxy flexible polymer encapsulation over irregular ceramic foams leading to effective load transfer to all struts. This is also evident from the absence of several kinks in a stress-strain curve observed in bare foam. Al_2O_3 and ZTA foam on infiltration with polymer and aluminium metal have remarkably enhanced compressive strength compared to bare foam and encapsulated foams. The stress-strain curve also exhibited a transformation of fracture behaviour from brittle fracture to ductile due to infiltration. The stress-strain curve shows distinct regions such as increasing stress with strain and a plateau showing the constant load-bearing region and a region of decreased compressive stress with strain. This behaviour can also be attributed to the epoxy polymer/metal fraction, which partially bears the load in combination with ceramic strut reinforcements. Fig. 12 shows the comparison of compressive strength values of Al_2O_3 and ZTA foams.

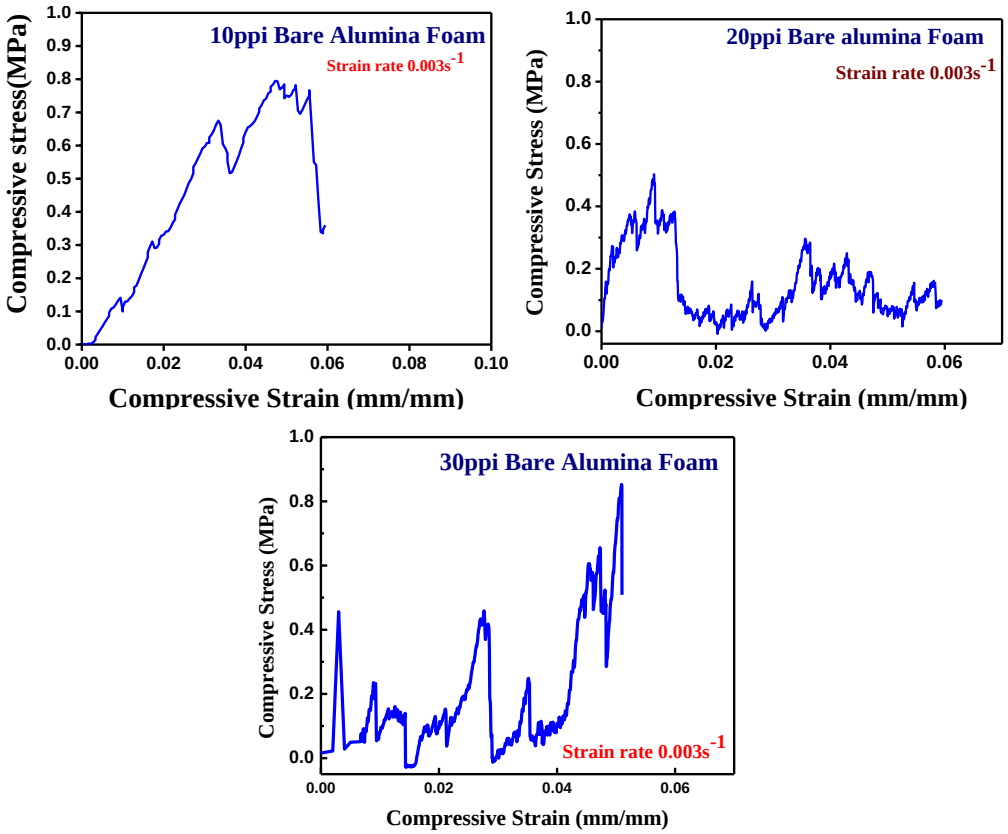

Fig. 4.10 *shows the compressive Stress-strain curves of* Al_2O_3 *foam (a)10 PPI (b)20PPI(c)30PPI.*

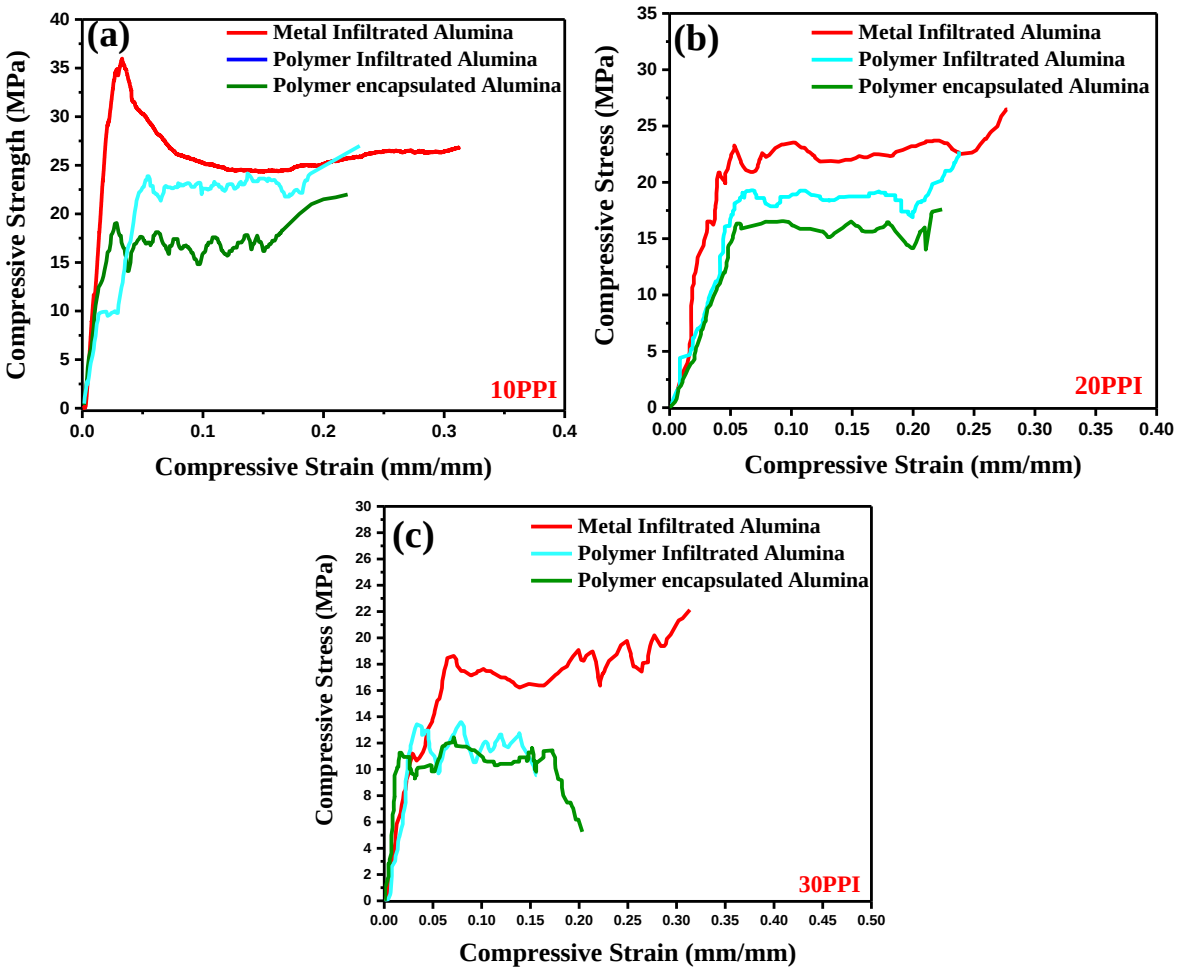

Fig. 4.11 *shows the compressive Stress-strain curves of infiltrated and encapsulated with polymer and metal (a) 10 PPI (b) 20 PPI (c) 30PPI.*

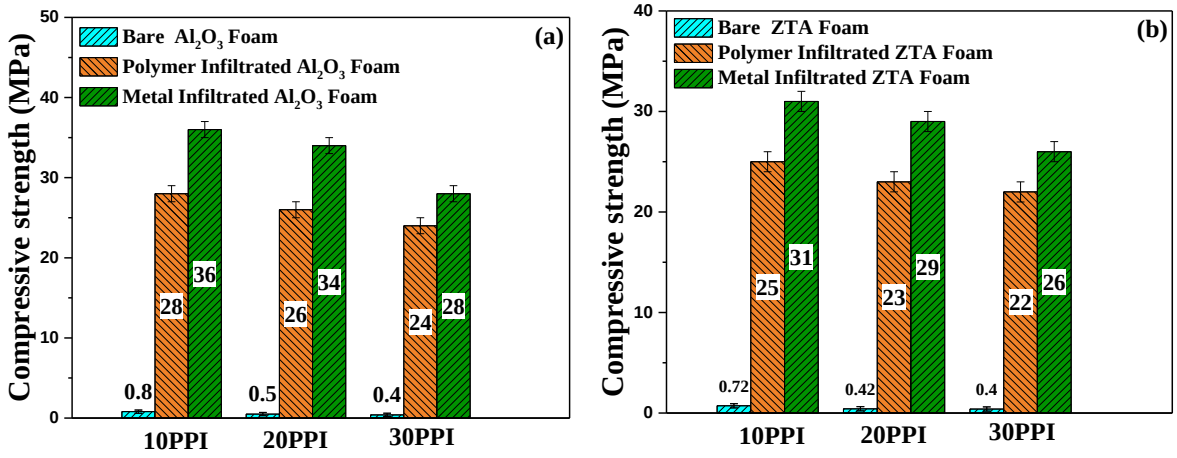

Fig. 4.12 *shows the comparison of all the compressive values (a) Alumina foam (b) ZTA.*

4.3.2.2 Impact Test

All the fabricated foams (bare and composite) with different pore levels are characterized under the dynamic condition to evaluate specific impact energy (SIE). The results of SIE values are shown in Fig. 4.13. Metal infiltrated 10PPI foams showed higher SIE values when compared to polymer composite and bare foams. All the values are represented in Table. 4.3. In the case

of foams with metal infiltration, molten metal fraction in the foam contributes to enhancing the energy absorption through the mechanism of composite failure.

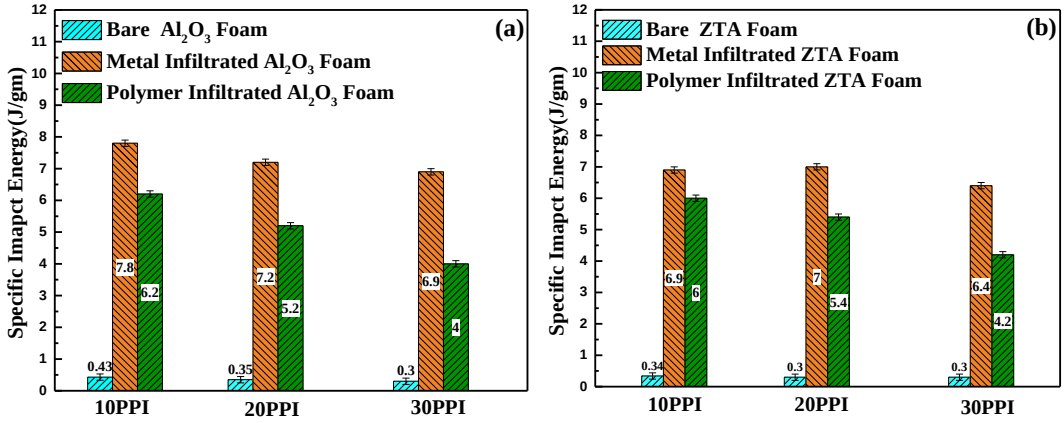

Fig. 4.13 *shows the comparison of all the specific impact values of (a) Alumina foam (b) ZTA foam*

Table 4.3 *represent the mechanical properties of* Al_2O_3 and ZTA foams

			Alumina			ZTA		
Foam condition (PPI)			10	20	30	10	20	30
Strut Thickness(mm)			0.85±0.2	0.69±0.2	0.41±0.2	0.84±0.2	0.63	0.4
Cell Diameter (mm)			1.35±0.2	1.21±0.2	1.11±0.2	1.30±0.2	1.20	1.0
Porosity (%)			80	82	85	82	84.3	86
Compression (MPa)	Bare foams		0.8	0.5	0.4	0.72	0.42	0.4
	Encapsulation with polymer		6.32	6	5.2	5	5.5	6.1
	Infiltration	Polymer	28	26	24	25	23	22
		Metal	35	34	28	31	29	26
Plateau stress (σ_{pl} (MPa))			1.2	0.95	0.6	1.2	0.8	0.5
Energy absorption efficiency (EAE (%))			60.2	40	34	58	38	33
Energy absorption density (ε_{cd})			4	2.1	0.7	1.8	2	1.6
Porosity (%)			94.5	93.9	93.5	92	90	89.5

4.4 Summary

Alumina and ZTA foams (10PPI, 20PPI, 30PPI) were successfully prepared using a polymeric sponge replication process. The samples are subjected to infiltration with molten aluminium and encapsulate & infiltrated with polymer in order to make a metal and polymer composite. 10PPI metal infiltrated foam with 36MPa shows better mechanical properties with respect to all other foams

Study the Effect of Nickel Coating on the Mechanical Behaviour of Al_2O_3 Foams

The effect of Nickel coating on the mechanical behavior of Al_2O_3 foams under quasi-static and dynamic conditions was studied. Initially, Al_2O_3 foams with 10, 20 and 30 Pores Per Linear Inch (PPI) were prepared by polymeric sponge replication technique and subsequently, foams were coated with nickel (Ni) by an electrolytic process. The effect of nickel coating on cellular properties (pore size, density, strut thickness) and composite effect on physical and mechanical properties of alumina were also described. The fabricated foams were sintered at an optimized conventional sintering schedule. The details of the characterization techniques used are described in chapter 3.

5.1 Raw material characterization

XRD pattern for alumina powder is shown in **Fig. 5.1.** The XRD data confirmed Phase pure alpha-alumina. Thermogravimetric curve and DTA indicating thermal events are shown in **Fig. 5.2**. It is evident from TG curves that degradation of polyurethane foam starts at 270 ^oC and reaches a plateau at 400 ^oC, the complemented DTA peaks indicating exothermic reactions due to polymer burnout during heating.

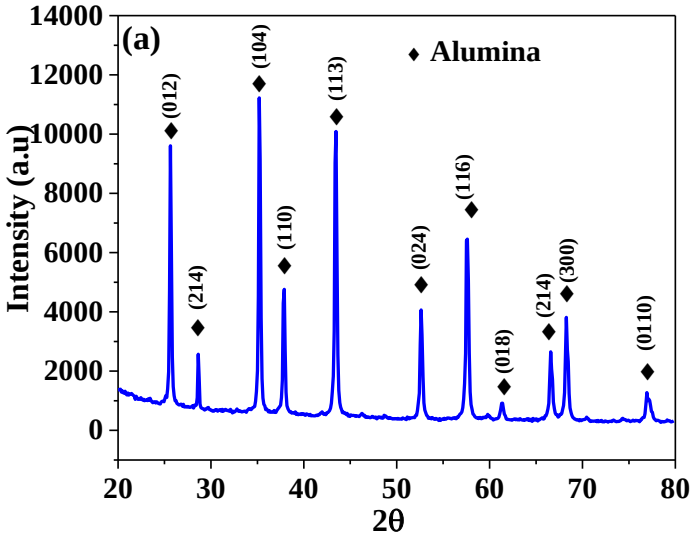

Fig.5.1 *XRD pattern of the as-received alumina powder.*

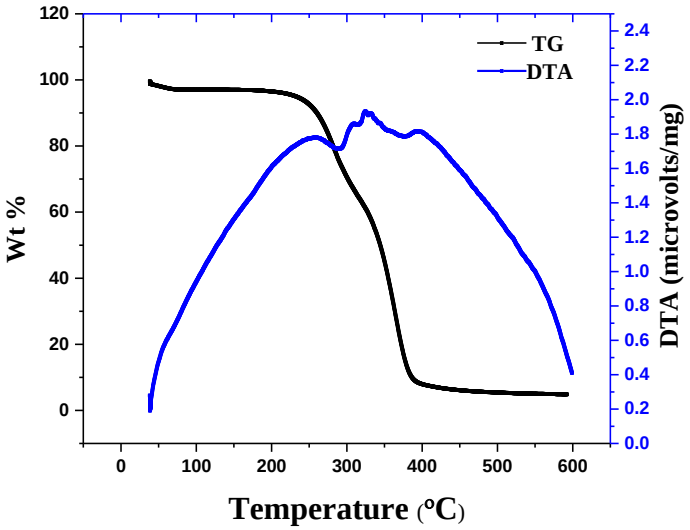

***Fig.5.2** TG-DTA curves of polyurethane foam.*

5.2 Mechanism of Electroplating of Nickel

Under the direct current's influence, a process occurs at anode and cathode (Al_2O_3 foam with conducting coating), respectively.

$$\text{Anode: } Ni \longrightarrow Ni^{+2} + 2e^{-} \qquad (5.1)$$

$$\text{Cathode: } Ni^{+2} + 2e^{-} \longrightarrow Ni \qquad (5.2)$$

Positively charged nickel ions (Ni^{+2}) produced at the anode will be attracted to alumina foams coated with a conductive coating that acts as the negative electrode [230]. The positively charged nickel ions (cations) get deposited as Ni, and the coating process continued until the desired thickness is achieved on alumina foams. The deposition rate was found to be 2.85µm/min at an equilibrium point.

5.3 Effect of number of coating on cellular properties

A plot of porosity, pore size and strut thickness vs number of coatings is shown in Figs. 5.3 (a)-(c), respectively. A significant reduction in porosity from 84 % to 18 % is observed on increasing the coating 4 times. Accordingly, a marginal decrease in pore size and a complementary increase in strut thickness are also observed in general in foams. However, it is evident from Fig. 3(b) that the final pore size and strut thickness are a function of the initial pore size of the templates. Fig. 3(c) shows the pore per linear inch increases from 10 to 30 PPI. At the same time, strut thickness decreased from 0.7 mm to 0.2 mm, which can be attributed to the flow constraints associated with the slurry of high solid loading under identical conditions.

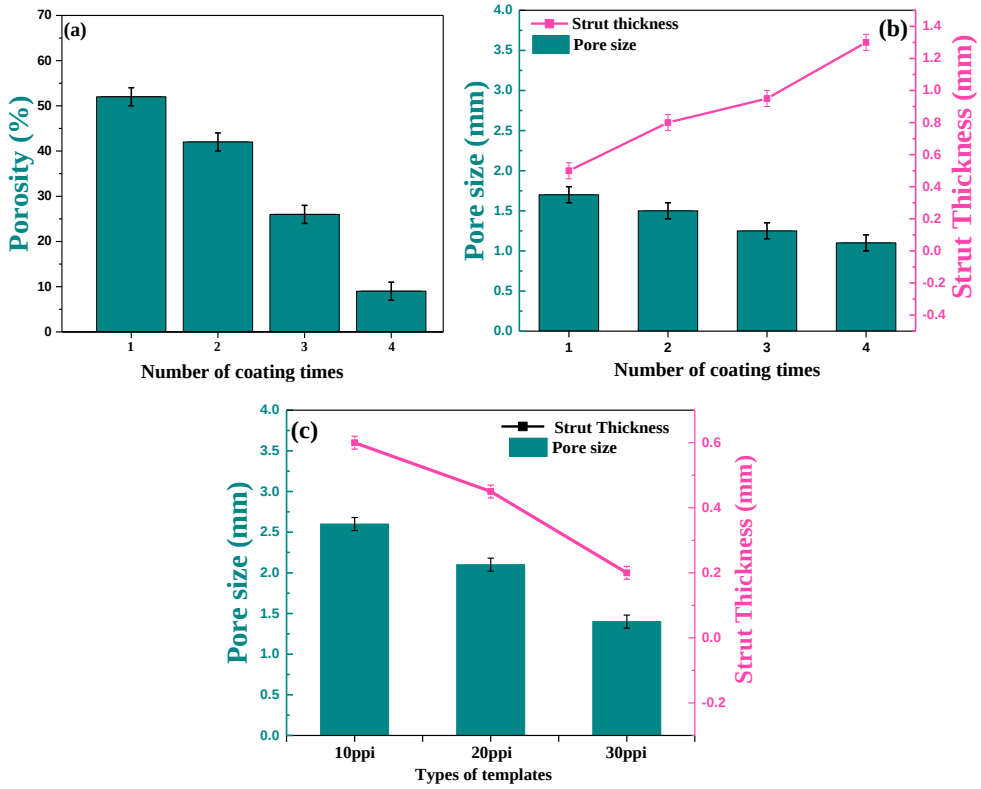

Fig. 5.3 *Images of a) Porosity vs coating times b) Pore size vs number of coatings vs strut thickness c) Pore size vs types of template vs strut thickness.*

5.4 Sintering

All the foams were subjected to a slow heating rate of 1 ^{o}C/min up to 400 ^{o}C to ensure the free escape of residual burnout gases without creating any micro-crack on the struts resulting from excess gas pressure within the escape channels. The heating schedule also provided soaking to ensure removing all organic materials without any ashes before heading to the peak temperature of 1650 ^{o}C. A typical SEM picture of AF sample sintered at 1650 ^{o}C is shown in **Fig. 5.4 (a)** and the XRD diffraction pattern recorded on the sample AF and ANF are shown in **Fig. 4(b).**

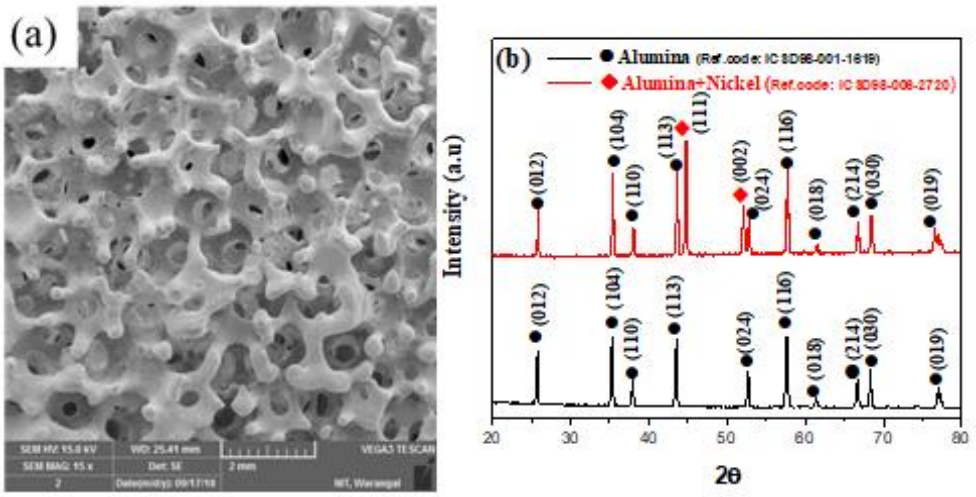

Fig.5.4 *a)SEM micrography of as-sintered and b) XRD patterns of AF and ANF samples.*

5.5 Microstructural and Mechanical characterization

5.5.1 Microstructural characterization.

A plot of coating thickness of Ni vs coating time is shown in **Fig. 5.5**. There is a strong correlation between thickness and coating duration. A typical micrograph showing the coating thickness of 13.3 µm after coating for 3 min, which increased to 51.4 µm after 18 min, is shown in Figs. **5.5 (a)** and **(f)**. Beyond 18 minutes, the coatings were delaminated, resulting in peeling off, and the coatings were also found to be brittle. SEM pictures of the interfacial features showing adhesion due to heat treatment without any delamination. Though there is a difference in the thermal expansion of alumina substrate and nickel, the stress did not result in delamination or micro-cracking along with the interface due to the inherent porosity that existed in the substrate as the deposit.

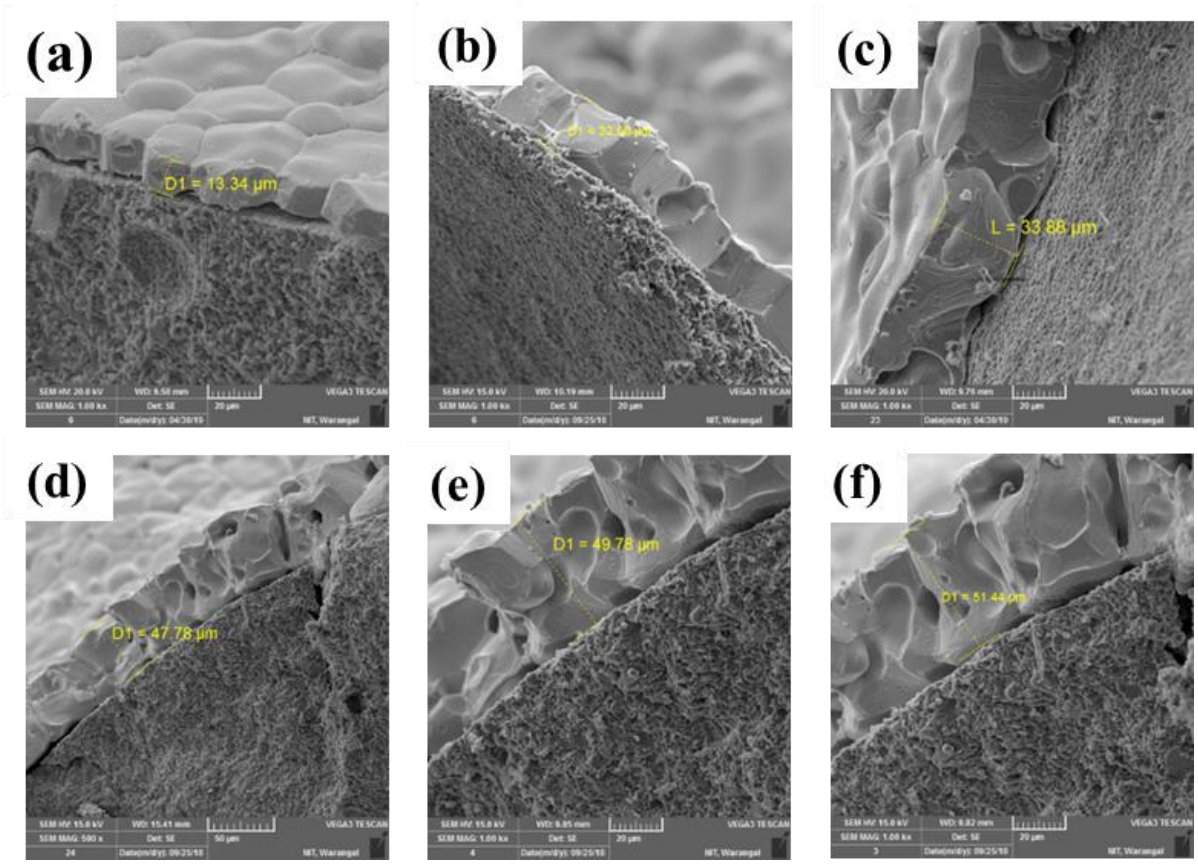

Fig. 5.5 *SEM Image of Cross section of ANF with different time intervals (a) 3min (b) 6min (c) 9min (d) 12min (e) 15min (f) 18min.*

5.5.2 Mechanical characterization

Stress-strain curves recorded on AF and ANF foams are shown in Fig.5.6. It is evident from the stress-strain curves that AF specimens showed 0.8, 0.52 and 0.4 MPa for 10, 20 and 30 PPI, respectively and this was complemented by solid supporting the load. All the foam samples, irrespective of their cell density, exhibited similar failure behaviour, showing a steep increase

initially to a peak stress value followed by a sudden drop exhibiting typical brittle failure. In case of ANF specimen, Ni coating resulted in a substantial increase in compression strength, as is evident in Figs 5. 6(a)-(c). The compressive strength of ANF specimens was 16.2, 8.3 and 6 MPa for 10,20 and 30PPI, respectively.

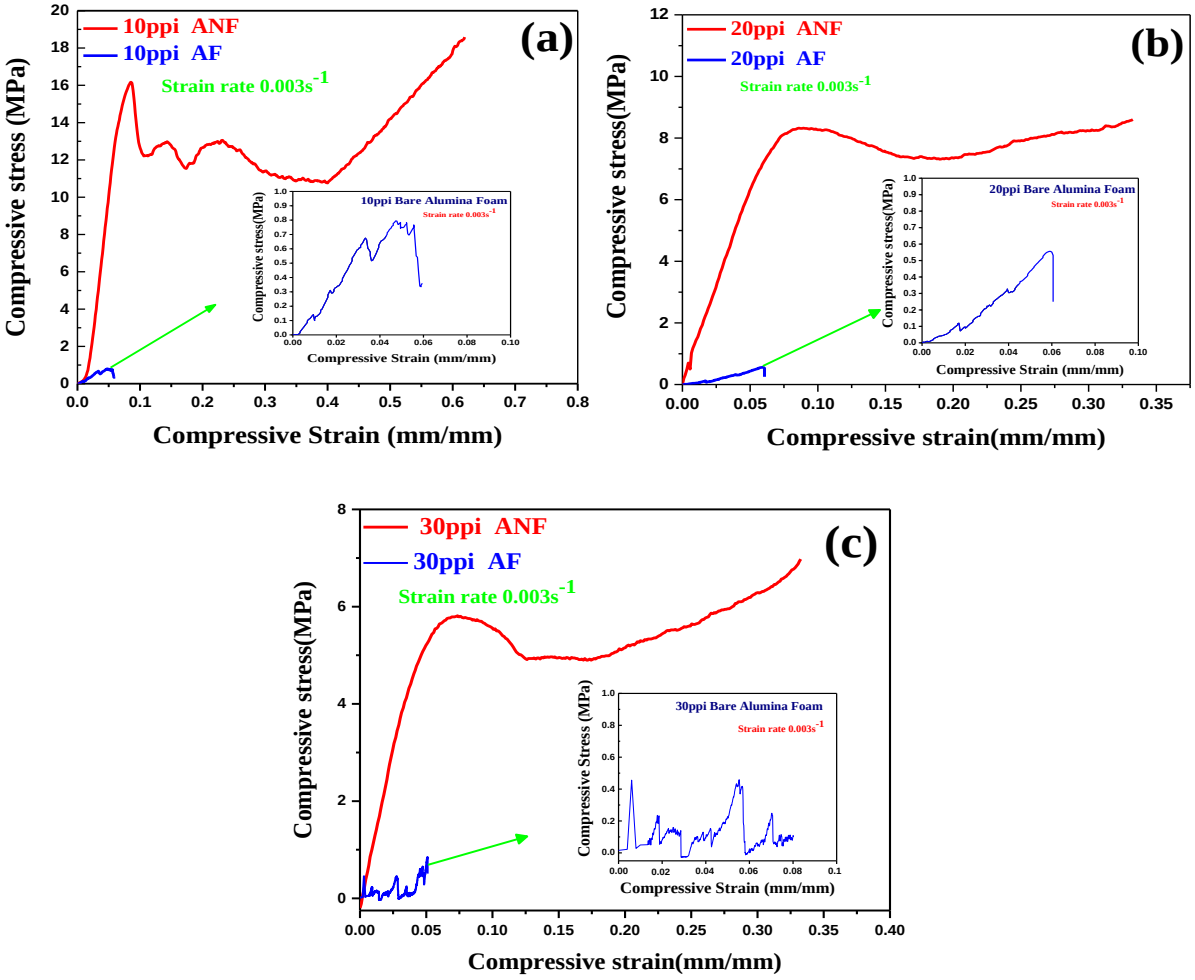

Fig. 5.6 *Compression stress-strain curves of (a) AF and ANF with 10PPI (b) AF and ANF with 20PPI (c) AF and ANF with 30PPI*

Further, there was a significant change in the mechanism of fracture in all foams, going from brittle to ductile behaviour. Additionally, higher peak compressive stress values were enhanced by inhibiting crack initiation on surface flaws on AF due to Ni coating. A plot of compressive strength as a function of coating thickness with respect to time is shown in Fig. 5.7, which exhibits a strong correlation with the compressive strength and coating thickness.

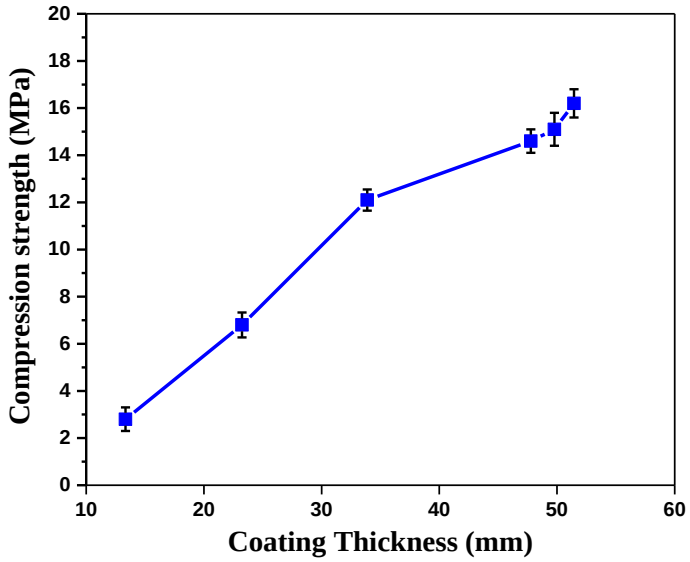

Fig. 5.7 *Relationship between the compression stress of foam with coating thickness*

Further, Plateau stress (σ_{pl})**,** energy absorption per unit volume (U_v or energy absorption density (EAD)), densification strain (ε_{cd}), and energy absorption efficiency (EAE) were estimated using the equation [231] below:

$$\sigma_{pl} = \frac{\int_{\varepsilon_y}^{\varepsilon_{cd}} \sigma d\varepsilon}{\varepsilon_{cd} - \varepsilon_y} \qquad (5.3)$$

Where σ_{pl} is plateau stress, ε_{cd} is onset densification strain and ε_y strain value at initial yield corresponding to the plateau regime [231]. These points represent the interaction between cell walls with respect to different points on stress-strain curves [32]. Table-1 represents the values of energy absorption efficiency (EAE), energy absorption density (ε_{cd}) and plateau stress (σ_{pl}). Further, the plateau region is analyzed using densification strain (εcd), representing the interaction between the cell walls at different points on the stress-strain curve and deformation modes in the plateau region. Densification strain (ε_{cd}) is calculated from the plot of energy absorption efficiency (EAE) vs compressive strain. Energy absorption efficiency (EAE) is regarded as the ratio of energy absorption at a particular strain divided by stress (σ), and is expressed as equation (2) below [232,233],

$$e = \frac{1}{\sigma} \int_0^{\varepsilon} \sigma d\varepsilon \qquad (5.4)$$

Energy absorption of the cellular structures per unit volume (U_v) was calculated from the area under the stress-strain curve up to the densification strain ε_{cd}, and it is shown by equation [234] given below:

$$U_v = \int_0^{\varepsilon} \sigma d\varepsilon \qquad (5.5)$$

Fig.5.8 shows the comparison of stress vs strain and energy absorption efficiency vs strain for ANF samples for different pore sizes. Energy absorption efficiency increases monotonically with respect to strain value, reaches a maximum value at densification strain, and decreases with respect to increased strain value, as depicted in Table-5.1.

Table-5.1 *Plateau stress (σ_{pl}), energy absorption efficiency (EAE) and energy absorption density (ε_{cd}) values of AF and ANF foams*

PPI	σ_{peak} (MPa)		ε_{cd}		σ_{pl} (MPa)		EAE (%)		EAD (MJ/m^3)	
	AF	ANF	AF	ANF	AF	ANF	AF	ANF	AF	ANF
10	0.8	16.2	0.0436	0.55	0.306	0.625	2.24	40.29	0.00045	2.03
20	0.52	8.3	0.032	0.31	0.302	0.8	1.21	26.31	0.00031	0.89
30	0.4	6	0.031	0.25	0.28	0.74	1.01	21.78	0.00023	1.24

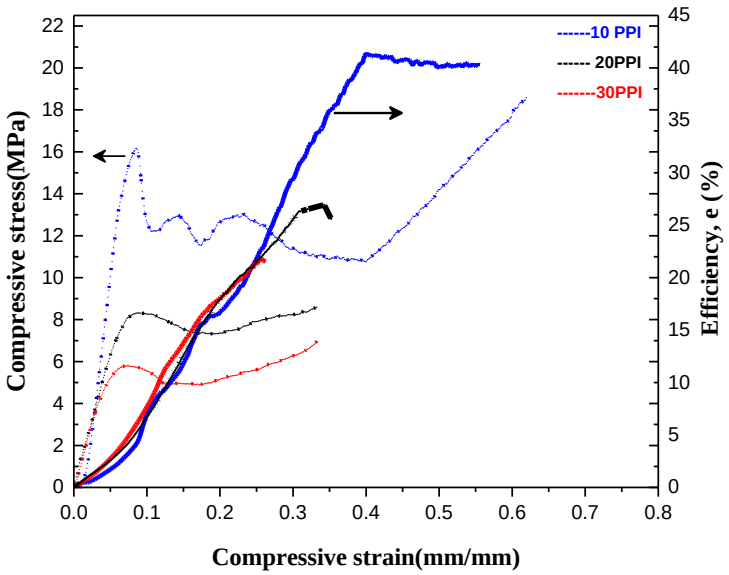

Fig.5.8 *Comparison of stress vs strain and energy absorption efficiency with strain.*

Fig. 5.9 shows specific impact energy (SIE) of AF and ANF foams. SIE values for bare Al_2O_3 were found to be 0.5, 0.4 and 0.35 Joules for different pore densities of 10, 20 and 30 PPI, respectively. In case of ANF specimens, there is a moderate enhancement of SIE, which was 8- 9 times the marginal difference based on PPI. The bonding at the heterogeneous interface of alumina and Ni results in the delamination of layers at higher stress values leading to its failure, which is also contributed by feeble bonding at the porous regions of the interface. This is probably why SIE values observed during impact tests as a result of Ni coating were relatively lower than enhancement in compressive strength values observed under lower shear rates. Fractographic analysis of SEM images depicted in Fig.5.10 indicated a mixed-mode of inter

and intragranular brittle fracture; however, the ANF fractographic analysis of Ni coatings showed ductile fracture features deformation marks and micro dimples.

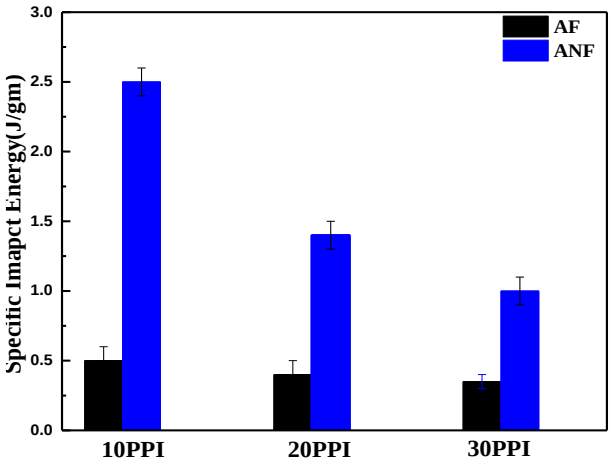

Fig. 5.9 *Specific impact energy values of different foams.*

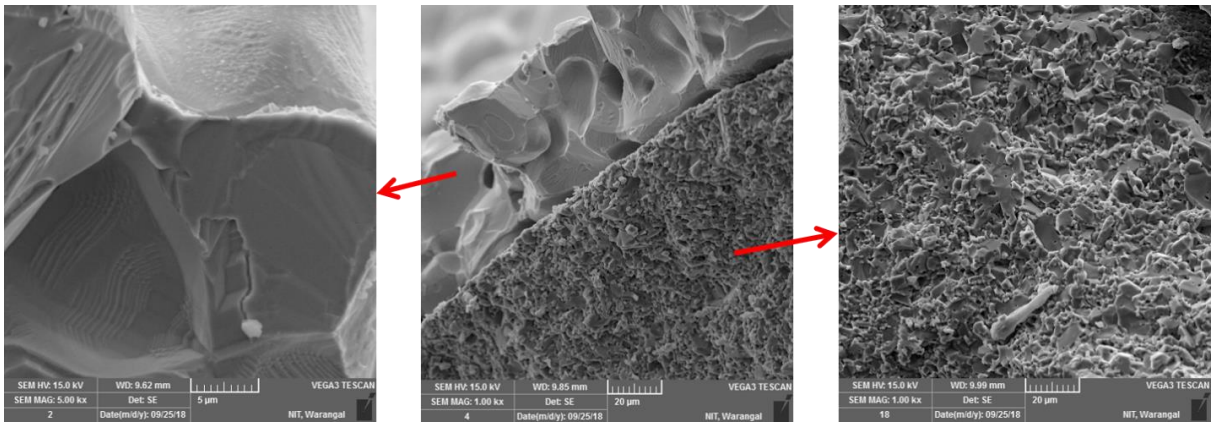

Fig. 5.10 *SEM micrographs of fracture surfaces.*

5.6 summary:

Reticulated foams with 10, 20 and 30PPI were prepared by the polymeric sponge replication process. In an attempt to improve the mechanical properties of alumina foams with their inherent brittle nature, the foams were electroplated with nickel. The effect of coating thickness on adherence and improvement in mechanical properties was evaluated. During static compression tests, Ni coating substantially enhanced compressive strength in case of all foams, irrespective of their pore density. An increase of 19 times in case of foams with 10 PPI and 14-15 times increase in case of foams with 20 and 30 PPI, respectively, was observed compared to bare foams due to Ni coating. Bare Al_2O_3, a brittle material, is a bulk structure and surface flaws play a major role in initiating crack under stress concentration. Ni coating acts as a barrier that prevents crack initiation under stress leading to higher peak compressive stress values.

Additionally, the ductile deformation of nickel also resulted in a mixed fracture behaviour. Plateau stress (σ_{pl})**,** energy absorption per unit volume (U_v or energy absorption density (EAD)), densification strain (ε_{cd}), and energy absorption efficiency (EAE) were estimated and evaluated based on comparison with foams, revealing the effect of Ni coating on the mechanical behaviour of alumina foams. Under the dynamic impact, energy absorption properties were limited to a maximum of 9 times compared to bare foams.

Open-cell Foams Prepared Through Thermo-Foaming Method

This chapter describes the fabrication of Al_2O_3 and ZTA foams through thermo-foaming method. Study the effect of different sucrose to powder weight ratios on microstructural and mechanical properties. Foaming temperature and foaming time on the porosity changes have also been discussed. The details of the characterization techniques used are described in chapter 3.

6.1 Raw materials characterization

XRD pattern for alumina powder and yttria-stabilized zirconia (YSZ) is shown in **Fig. 6.1(a)-(b)**. The XRD data confirmed phase pure alpha-alumina and YSZ.

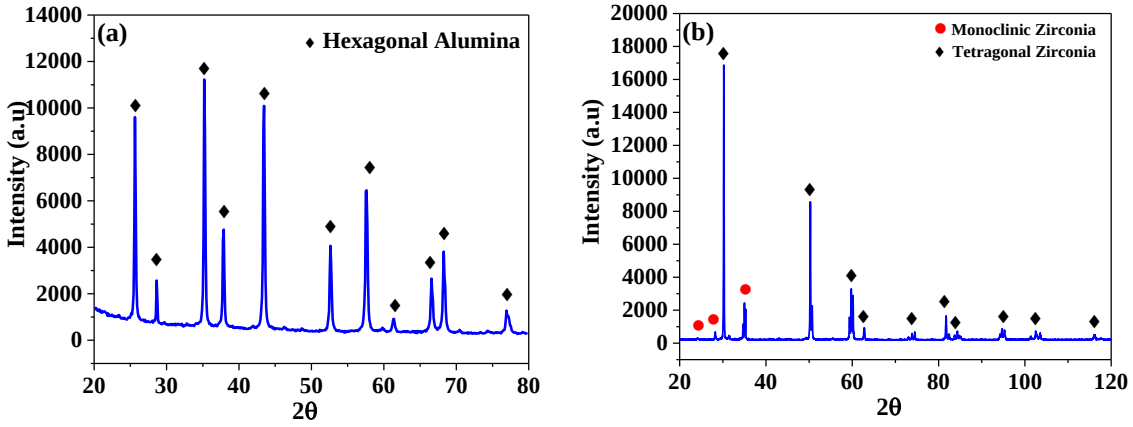

Fig. 6.1 *XRD analysis of (a) Alumina (b) yttria-stabilized zirconia (YSZ).*

Fig. 6.2 shows the TG/DTA plot of neat sucrose. It is evident from the TG plot that weight loss started around 230 °C due to dehydration of sucrose. Dehydrate sucrose, involving significant thermal exothermic reactions, is indicated in DTA peaks, leading to a complete loss at a range of 550-600 °C [235]

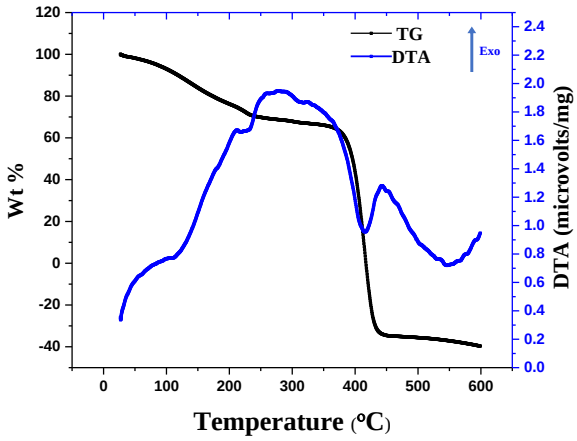

Fig. 6.2 *TG-DTA curves of pure sucrose.*

6.2 Foam fabrication

The process flow chart for the fabrication of Al_2O_3 and ZTA foams is depicted in Fig. 6.3. The Al_2O_3/ZTA powder to sucrose weight ratios ($W_{P/S}$) was mixed in planetary ball milling in acetone medium for 5h using zirconium balls as grinding media. Al_2O_3 powder to sucrose weight ratios, powder mixture to acetone, and sucrose to zirconia balls weight ratios are represented in Table .6.1.

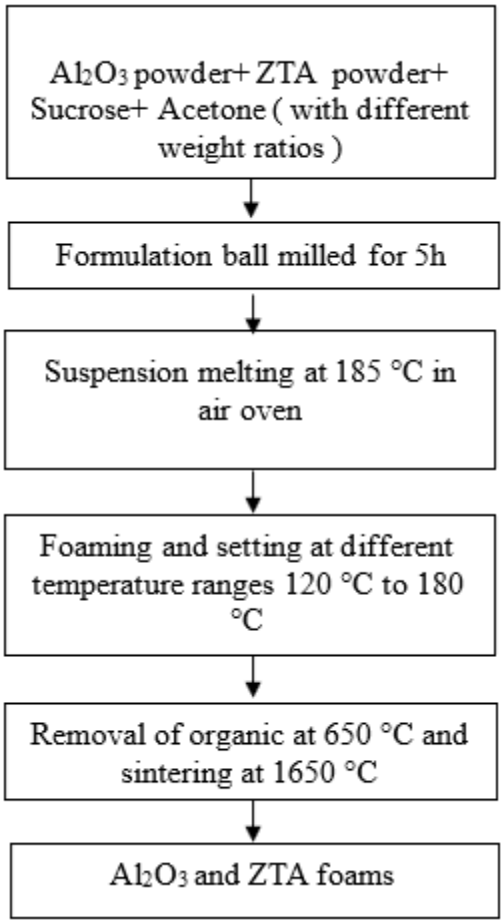

Fig. 6.3 *Preparation of Al_2O_3 and ZTA foams by the thermo-foaming method.*

Table .6.1 *represents the weight ratio values of powder to sucrose weight ratio, powder mixture to acetone and powder mixture to zirconia balls*

Details	Weight ratio
Powder to sucrose weight ratio ($W_{P/S}$)	0.6-1.4
Powder mixture to acetone	1:3
Powder mixture to zirconia balls	1:6

6.2.1 Foaming mechanism

The sucrose used in the present work melts at nearly 185 °C; further increase in temperature results in the formation of a dark brown, high viscous liquid known as caramel, which contains a complex mixture of compounds. During foaming at different temperatures, the -OH to -OH

condensations are catalyzed by H^+ generated from blowing agents, reducing the foaming time [236,237]. Al_2O_3/ZTA powder dispersed molten sucrose was heated in an oven at different temperatures ranging from 120 ºC to 180 ºC involving slow foaming and setting the mixture into solid foams without any additional blowing agent [238]. Al_2O_3/ZTA powder dispersions in molten sucrose undergo foaming when heated at different temperatures in the range of 120 ºC -180 ºC. The caramelization of sucrose involves the formation of glucose and fructose anhydride, while further condensation reactions via -OH groups to form polymeric products in different stages lead to the formation of caramelan ($C_{24}H_{36}O_{18}$), caramelen ($C_{36}H_{50}O_{25}$), and humin or caramelin ($C_{125}H_{188}O_{80}$) [236,239–241]. The bubbles are generated in molten sucrose due to water vapor produced by condensation reactions and are stabilized by viscosity. Bubble stabilization and setting in foam dispersions are attributed to improved viscosity due to continued condensation [242]. Al_2O_3/ZTA powder dispersion facilitates foaming by promoting -OH condensation. In addition, the Al_2O_3/ZTA powder particles adsorbed on the suspension/liquid-air interface provide extra bubble stability via a particle stabilization mechanism. Gas bubbles were stabilized by reducing gas-liquid/suspension interface tension using suitable surfactant or higher viscosity [243]. Fig. 6.4 (a) shows Al_2O_3/ ZTA powder dispersed in molten sucrose at 185 ºC, and Fig. 6.4 (b) shows after foaming and setting, while Fig. 6.4 (c) depicts crack free sample obtained after sintering at 1650 ºC. The foam rise value was calculated by the final foam height ratio to the initial Al_2O_3/ ZTA powder dispersion height, and Fig. 4 shows the foam rise value vs. foaming temperature. Fig. 6.5 shows the foam rise value vs foaming temperature. The foam rise value depends on the powder to sucrose weight ratio ($W_{P/S}$) and foaming temperature. The foam rise value increased with foaming temperature up to a critical foaming temperature (foam rising reaches a maximum at a particular temperature); after that, foam rise value decreased. Further increase of foaming temperature beyond the critical foaming temperature resulted in decreased foam rise value due to foam collapse. It is observed that $W_{P/S}$ influences the critical foaming temperature, and critical foaming temperature decreases when $W_{P/S}$ increases.

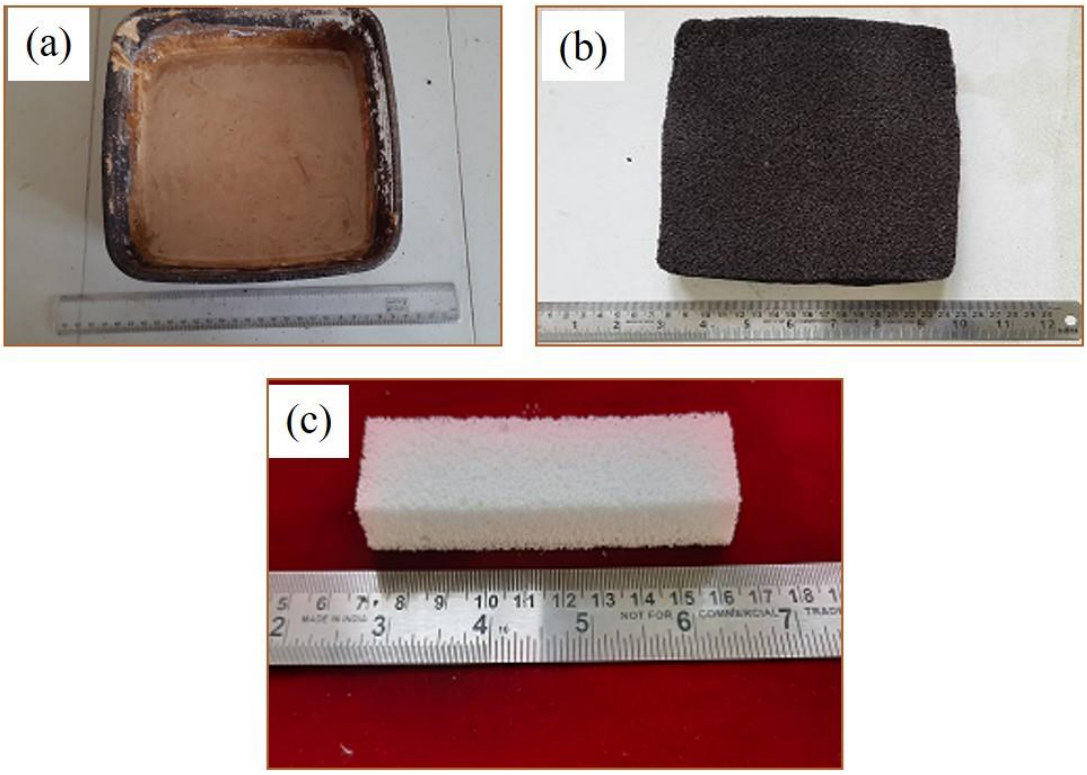

Fig. 6.4 Al_2O_3 /ZTA powders dispersion in sucrose melted at 185 ºC, (b) the foam obtained after foaming and setting, (c) after sintering at 1650 ºC.

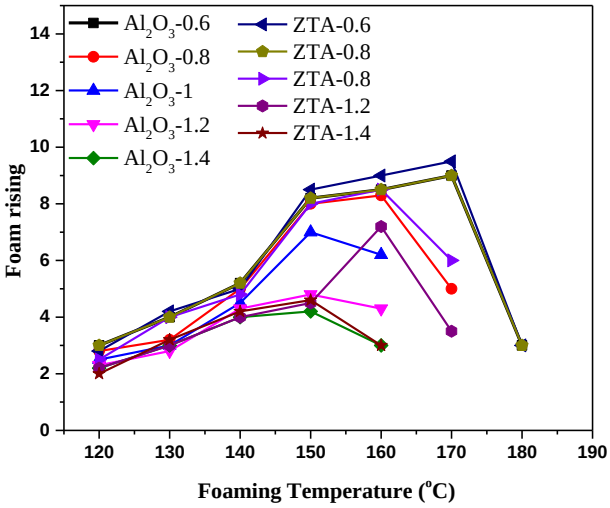

Fig. 6.5 *Foam rise value vs foaming temperature.*

Fig. 6.6 (a)-(b) represents foaming and foam setting time vs. foaming temperature ranging from 120 ºC to 180 ºC for different $W_{P/S}$ values. The foaming and foam setting time decreased with increasing $W_{P/S}$ and temperatures. The foams produced from this method had a hard layer on the top surface that had to be removed, and a sample crack-free uniform surface foam was obtained.

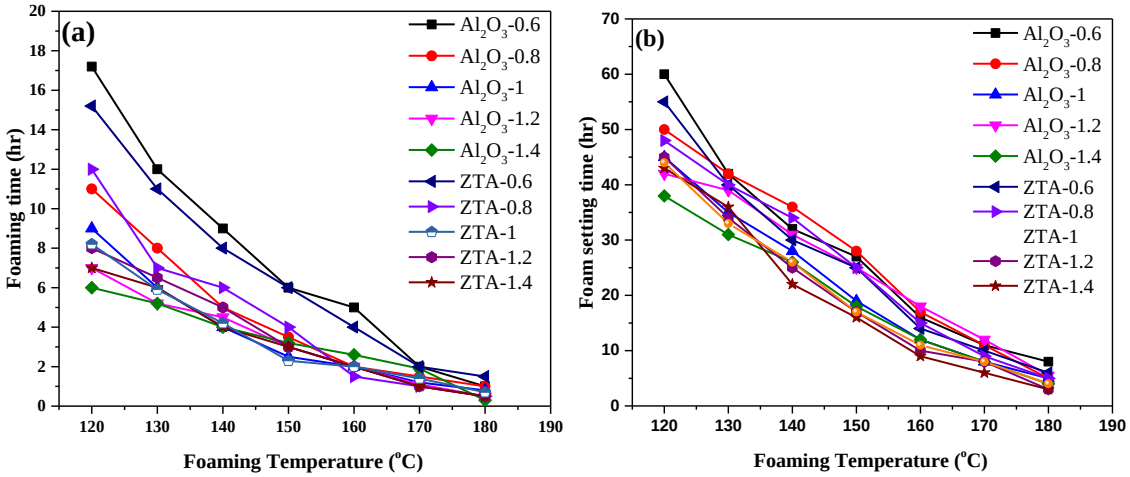

Fig. 6.6 *Relationship between (a) foaming time vs foaming temperature, (b) foam setting time vs foaming temperature.*

Fig. 6.7 shows the effect of foaming temperature on volume shrinkage with different weight ratios. Al_2O_3/ ZTA dispersed molten sucrose heated in an air oven for foaming and setting at different temperatures ranging from 120 ºC -180 ºC followed by sintering up to 1650 ºC. The volume shrinkage mainly depends on Al_2O_3/ZTA powder loading in $W_{P/S}$ composition. Foam shrinkage value decreased with an increase in $W_{P/S}$.

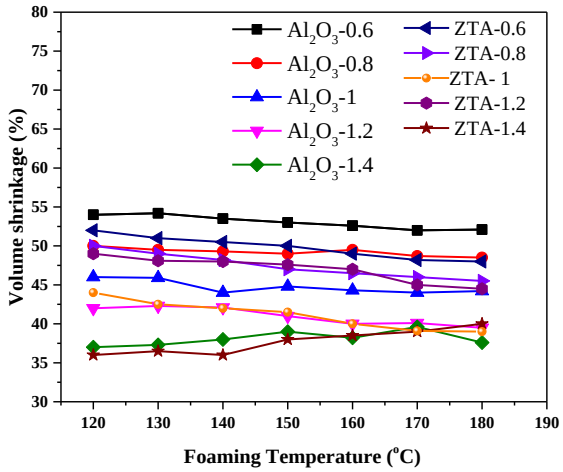

Fig. 6.7 *Effect of foaming temperature on volume shrinkage at different weight ratios.*

6.3 Phase analysis

The X-ray diffraction patterns of as-sintered Al_2O_3 and ZTA forms are presented in Fig. 6.8. The analysis of XRD patterns revealed that Al_2O_3 powders contain only α -Al_2O_3 phase (ICSD: 98–003-2923) and ZTA contains tetragonal zirconia phase (ICSD: 98–003-0698), monoclinic zirconia phase (ICSD 98-007-1839), and α -Al_2O_3 phase (ICSD: 98–003-2923) as indexed in Fig. 6.8.

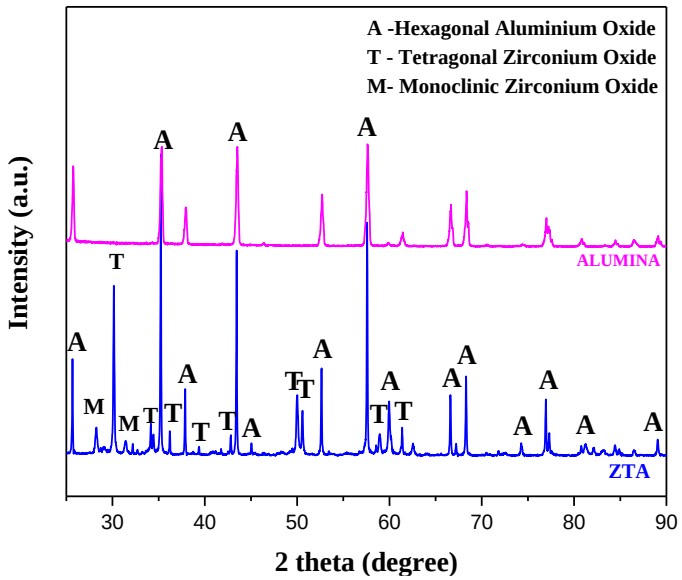

Fig. 6.8 *XRD patterns of Al_2O_3 and ZTA.*

6.4 Microstructural characterization

Al_2O_3/ZTA foams have interconnected cellular structures with solid struts represented in Fig. 6.9 (f), irrespective of $W_{P/S}$ and foaming temperature. Foams showed near-spherical-shaped cells up to $W_{P/S}$=1.2 and were interconnected through the cell window. Figs. 6.9 (a)-(f) show the SEM micrographs of various Al_2O_3 foams. When $W_{P/S}$ increased to 1.4, there was a significant distortion in the morphology. The foam cells extended in the direction of foam rise, resulting in a nearly oval form, as observed in Fig. 6.9 (e).

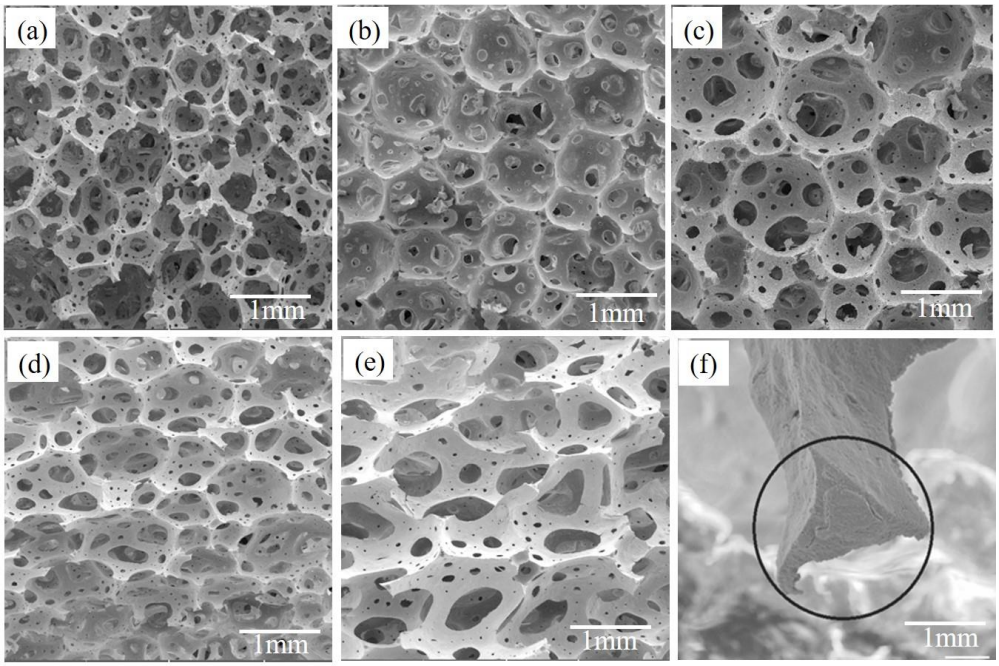

Fig. 6.9 SEM images of the Al_2O_3 foams with different weight ratios (a) $W_{P/S}$ =0.6, (b) $W_{P/S}$ =0.8, (c) $W_{P/S}$ =1, (d) $W_{P/S}$ =1.2, (e) $W_{P/S}$ =1.4 and (f) solid foam strut.

6.5 Mechanical characterization

6.5.1 Compressive Strength

Stress-strain curves recorded on Al_2O_3/ZTA foams with 1.2 weight ratios are shown in Fig. 6.10. The stress-strain curves of Al_2O_3/ZTA foams under static loading involve a linear elastic region followed by a yield point or peak stress and a plateau region. Initially, foams were deformed elastically up to the peak stress value; after reaching the maximum stress value, a sudden drop of stress due to fracture occurred on top of the cell strut and gradually transferred to the next cells. It continued with increasing load up to complete failure of the foam. All the foams showed similar failure mechanisms irrespective of cell density and size. Mechanical properties depend on the density of the foam. Table. 2 shows the foams' porosity with respect to different Al_2O_3/ZTA powder to sucrose weight ratios. The Compressive strength of Al_2O_3 and ZTA foams was 0.7, 1.2, 1.7, 1.9, 0.72 MPa respectively and 0.9, 1.3, 1.5, 1.8, 0.6 MPa respectively at different $W_{P/S}$ of 0.6, 0.8, 1, 1.2 and 1.4. Al_2O_3 and ZTA foams exhibited increased compressive strength values from 0.96 to 1.9 MPa and 0.9 to 1.8 MPa, when $W_{P/S}$ increased from 0.6 to 1.2. On further increasing Al_2O_3 and ZTA powder to sucrose weight ratio up to 1.4, a significant decrease in the compressive strength value to 0.72 and 0.7MPa occurred due to the partial collapse of cell walls during the foaming and setting in both foams.

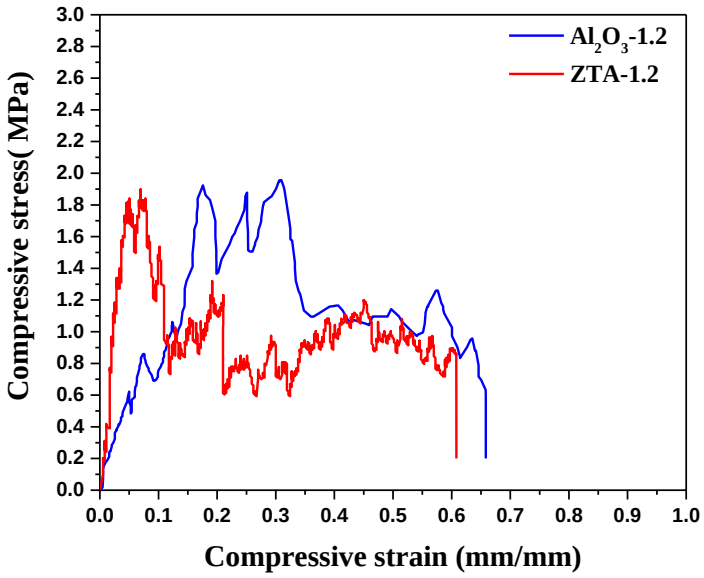

Fig. 6.10 *Stress-strain curves of the Al_2O_3 and ZTA foams at various Al_2O_3 and ZTA powder to sucrose weight ratios.*

6.5.2 3- Point Bending Test

Un-notched and notched Al_2O_3 and ZTA specimens were adopted for a 3-point bending test with different porosities ranging from 94.5% to 92% and 92% to 89.5%, respectively. Figs. 6.11 (a)-(b) show the typical load vs displacement curves of Al_2O_3 and ZTA specimens ($W_{P/S}$

=1.2), where the specimens showed a linear part followed by an abrupt drop of the applying load corresponding to a brittle failure. Un-notched specimens were used for analyzing the fracture strength using the following equation:

$$\sigma_f = \frac{3P_{max}L}{2BH^2} \quad (6.1)$$

P_{max} represents the peak load at fracture starts [244]. Notched samples were used for calculation of fracture toughness using the relation below:

$$K_{IC} = \frac{P_{max}}{BW^{0.5}} f(a/W) \quad (6.2)$$

$$f(a/W) = \frac{3}{2}(a/W)^{0.5} \frac{1.99-(a/W)(1-(a/W)[2.15-3.93(a/W)+2.7((a/W)^2}{[1+2(a/W)][1-(a/W)]^{1.5}}$$

Table .6.2 *represent the Values of Porosity, Compression (MPa), Bending stress (MPa), and Fracture toughness (MPa $m^{1/2}$)*

	Alumina					**ZTA**				
Weight ratios ($W_{P/S}$)	0.6	0.8	1	1.2	1.4	0.6	0.8	1	1.2	1.4
Compression (MPa)	0.7	1.2	1.7	1.9	0.72	0.9	1.3	1.5	1.8	0.6
Bending stress (MPa)	0.49	0.54	0.69	0.75	0.51	0.7	0.85	1.1	1.2	0.75
Fracture toughness (MPa $m^{1/2}$)	0.53	0.67	0.76	0.77	0.54	1.23	1.27	1.31	1.36	1.1
Porosity (%)	94.5	93.9	93.5	90.2	92	92	90	89.5	89.4	89.5

The bending strength and fracture toughness of Al_2O_3 and ZTA foams are listed in Table. 2. Al_2O_3 foams had lower bending strength and fracture toughness compared to ZTA foams. ZTA foams showed increased bending strength when compared to Al_2O_3 foams values and these were 42.8%, 57.4%, 59.42%, 60%, 47% respectively while fracture toughness was 131.1%, 89.5%, 72.3%, 76%,103.7% at different weight ratios ranging from 0.6-1.4 respectively. ZTA foams possess good toughness due to their unique property known as the transformation toughening mechanism. In ZTA foams, the applied load reaches a peak point; the foam starts cracking, and the crack tries to propagate through tetragonal zirconia polycrystals (TZP) grains [8]. Fig. 6.12 shows TZP grains (white colour) in the Al_2O_3 matrix. The tetragonal grains in the vicinity of crack propagation transform into the monoclinic phase through a stress-induced transformation; the volumetric expansion of transformed grains generates a compressive force on the crack which resists propagation [245,246].

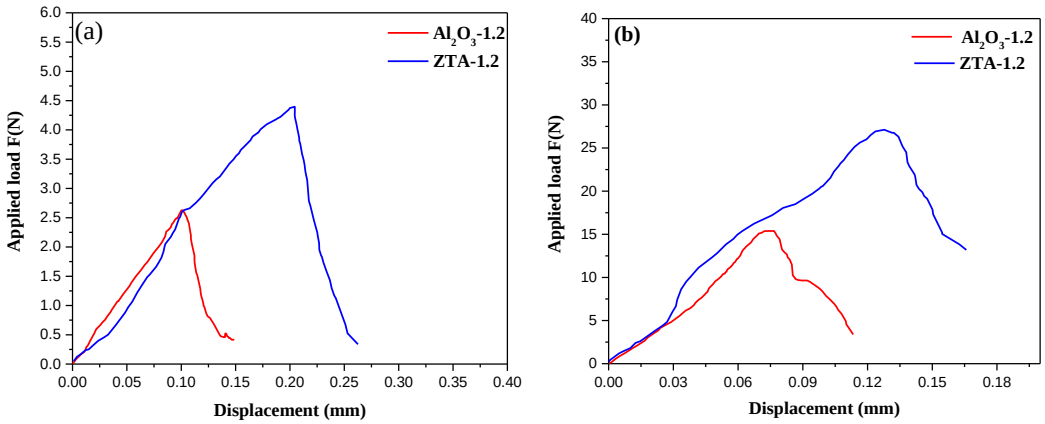

Fig. 6.11 *load-displacement curves (a) un-notched specimen and (b) notched specimen.*

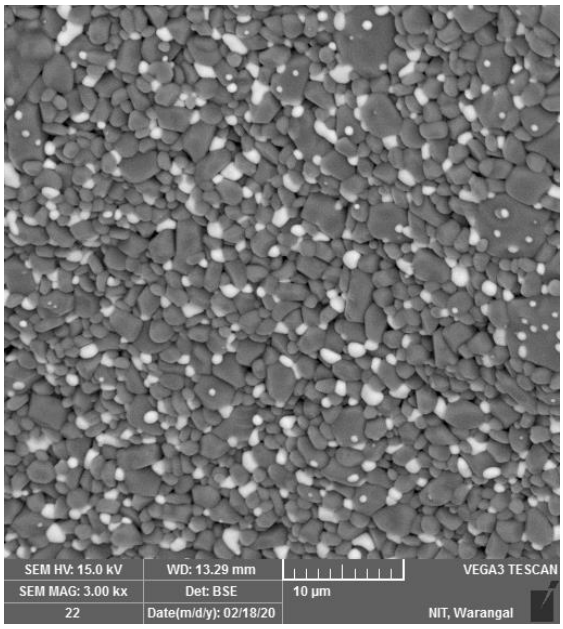

Fig. 6.12 *SEM image of strut surface of ZTA foam.*

6.6 Conclusions

Al_2O_3 and ZTA foams were successfully fabricated using the thermo-foaming method with different powder to sucrose weight ratios ($W_{P/S}$ =0.6 to 1.4). The compressive strength (σ), bending strength and fracture toughness of the foams were evaluated. Maximum compressive strength of 1.9 MPa was observed for Al_2O_3 and 1.8 MPa for ZTA at $W_{P/S}$ value 1.2. Further increase in $W_{P/S}$ value led to decreased compressive strength due to partial collapse of foams cells during foaming and setting. ZTA samples showed better bending strength and fracture toughness than Al_2O_3 foams irrespective of their $W_{P/S,}$ and the corresponding values are 1.2 MPa and 136 MPa $m^{1/2}$. The improved bending strength and fracture toughness of ZTA is attributed to the transformation toughening mechanism.

Closed-cell Foams Prepared through Sacrificial Phase Template Technique

This chapter describes the fabrication of Al_2O_3 and ZTA closed-cell foams through the space holder method. It studies the effect of pore size on the mechanical properties of Al_2O_3 and ZTA closed-cell foams. Different sizes and volume percentages of space holders (polystyrene beads) were added to the powders to obtain varying porosities. Pore size and porosity effect the mechanical properties we have discussed. The details of the characterization techniques used are described in chapter 3.

7.1 Raw materials characterization

7.1.1 Phase and microstructural analysis

XRD pattern for alumina powder and yttria-stabilized zirconia (YSZ) is shown in Fig. 7.1(a)-(b). The XRD data confirmed phase pure alpha-alumina and YSZ.

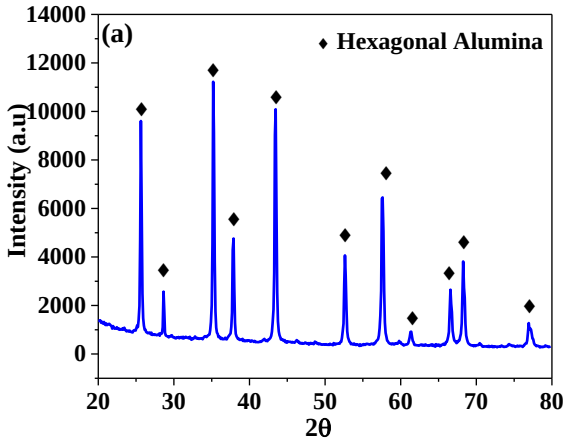

Fig. 7.1 *XRD analysis of (a) Alumina (b) yttria-stabilized zirconia (YSZ).*

Different size spherical shape polystyrene beads were used as a space holder in this study. **Fig.7.2** shows the SEM images of polystyrene beads with uniform sizes.

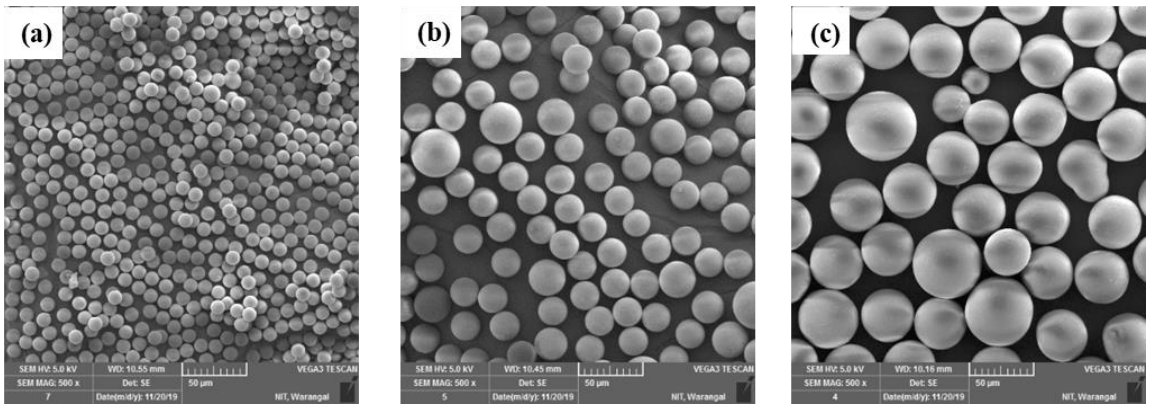

Fig. 7.2 *Polystyrene beads with different sizes a) 10µm b) 20 µm c) 40 µm.*

7.1.2 TG-DTA Analysis

Fig. 7.3 shows the TG-DTA plot of neat sucrose. It is evident from the TG plot that weight loss started around 230 °C due to dehydration of sucrose. Dehydrate sucrose, involving significant thermal exothermic reactions, is indicated in DTA peaks, leading to a complete loss at a range of 550-600 °C.

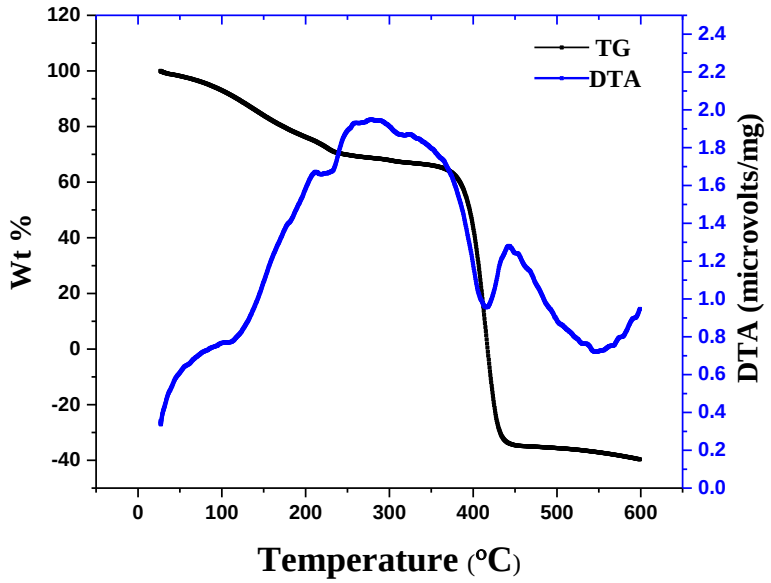

Fig.7.3 *TG-DTA curves of polystyrene beads.*

7.2 Foam fabrication

Al_2O_3 and ZTA closed-cell foam with varying porosities were fabricated. Fig. 7.4. shows the flow chart for fabrication of Al_2O_3 and ZTA closed-cell foam with varying porosities. Varying porosities were obtained by adding different volume % of beads to the powders. Different wt % (i.e 5 to 20 wt%) of YSZ were added to the zirconia powder to make ZTA, and these ZTA compositions were labeled as ZTA-5, ZTA-10, ZTA-15, and ZTA-20. Different sizes of beads were added to the Al_2O_3 and ZTA powders to obtained varying porosities described in the below Fig.7.4

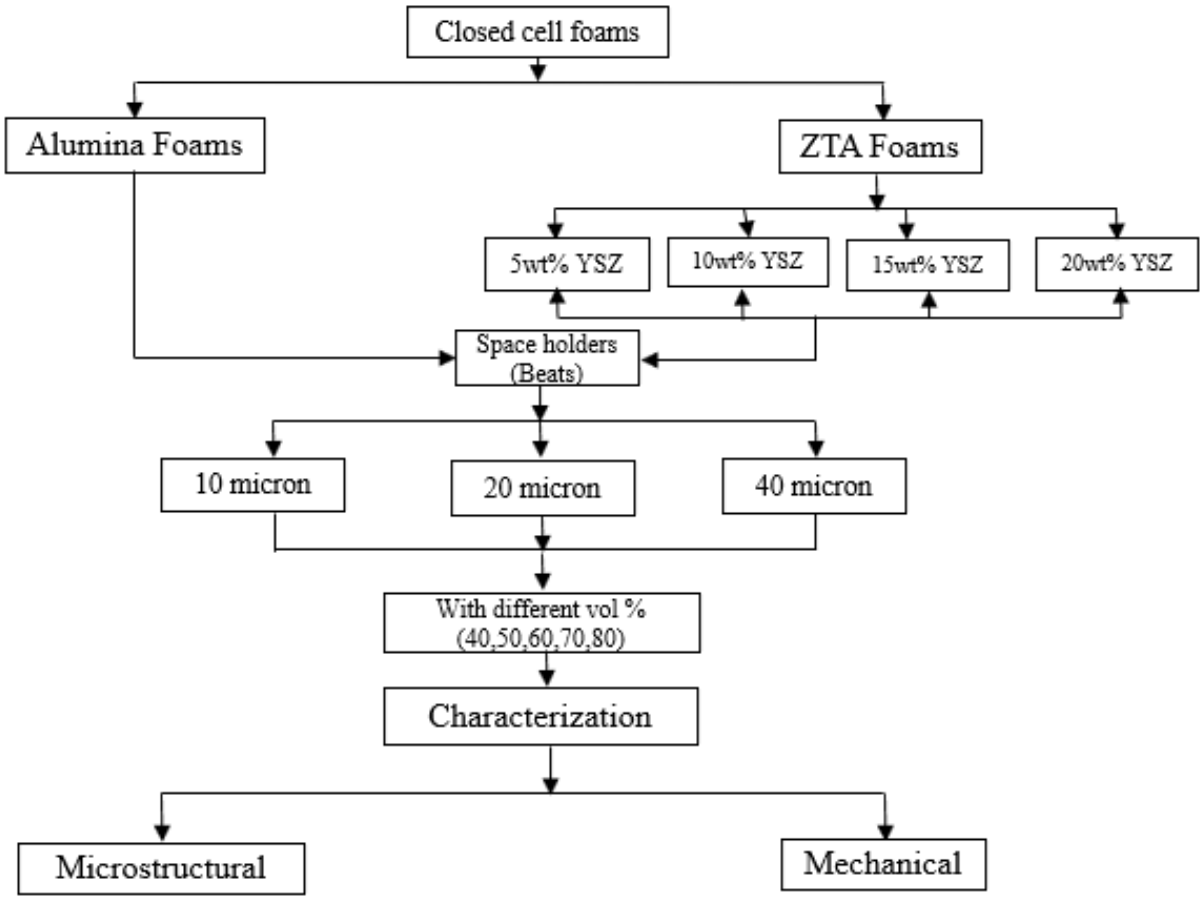

Fig.7.4 *Preparation of Al_2O_3 and ZTA foams by the space holder method.*

7.3 Optimization of sintering temperature

Based on TG/DTA study, the sintering schedule was designed and is shown in Fig 7.5. Pyrolysis of the polystyrene beads starting at 230 °C and ends at 550 °C. In this process, we used two different heating rates i.e 0.5 °C/min and 0.1 °C/min. A higher heating rate (0.5 °C/min) will result in cracks on the sample due to a higher pyrolysis rate. To reduce these cracks, we used a lower heating rate, i.e. 0.1 °C/min, and obtained a crack-free sample. Fig 7.5 shows the sintered samples at 1650 °C with a heating rate of 0.5 °C/min and 0.1 °C/min.

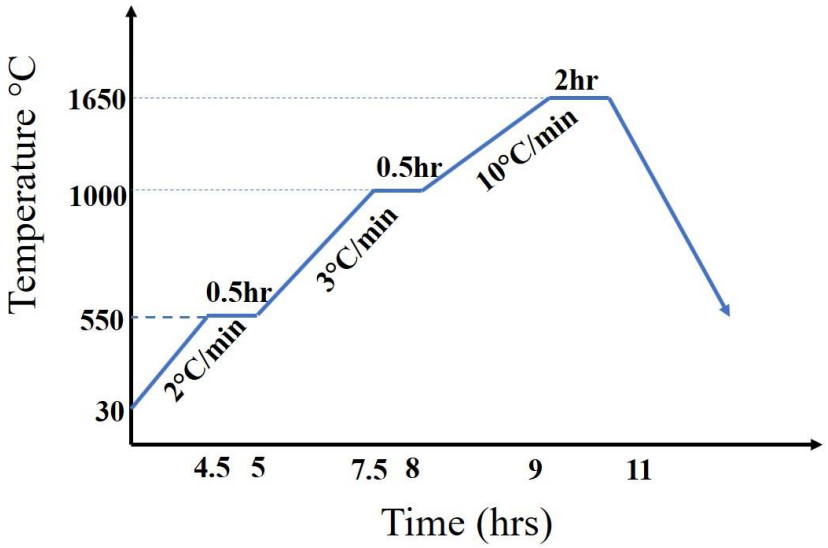

Fig.7.5 *Image of Heating schedule*

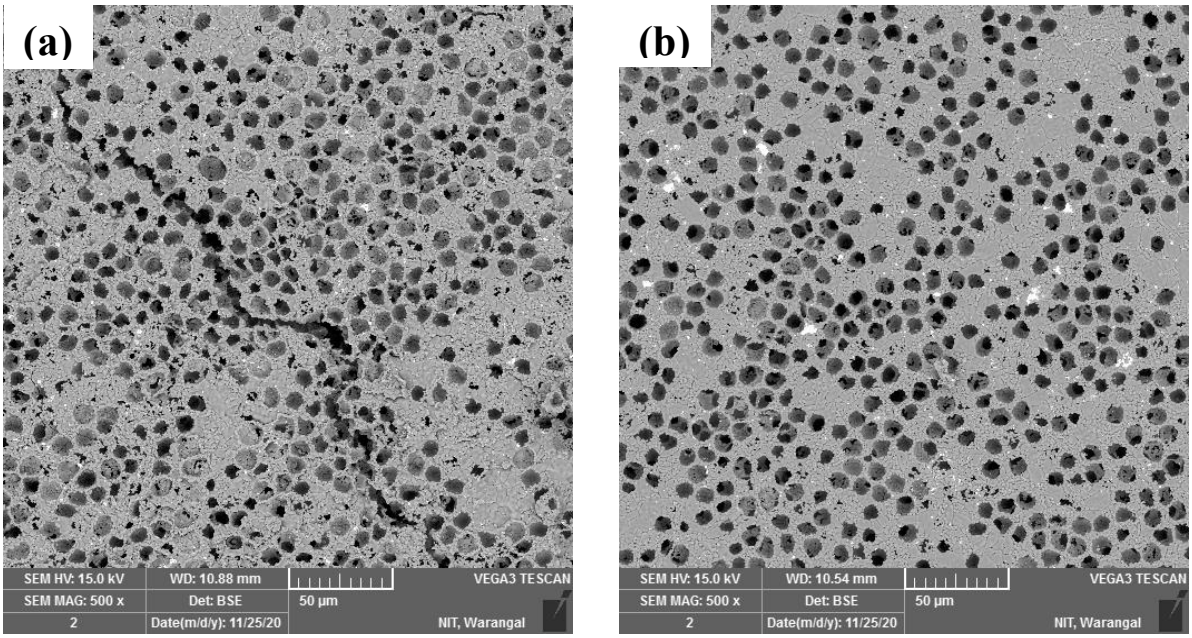

Fig. 7.6 *SEM images of sintered sample at 1650 °C a) 0.5 °C/min b) 0.1 °C/min.*

7.4 Microstructural analysis

A scanning electron microscope (SEM) was used to find the pore size and pore distribution in the sample after sintering. Fig 7.1 shows the microstructure of ZTA-20 foam with 10 µm size pore size with different volume % of beads added to the powder. The number of pores and porosity is dependent on the volume % of beads added to the powder. Fig 7.1 (a) shows the 20 vol% beads added to ZTA-20 and its low porosity and less number of pores being formed than 80 vol%. Fig. 7.2 and Fig.7.3 show the images of 20 µm and 40 µm size pores with different volume % beads added to the powder. Table 7.1 represents all the porosity values.

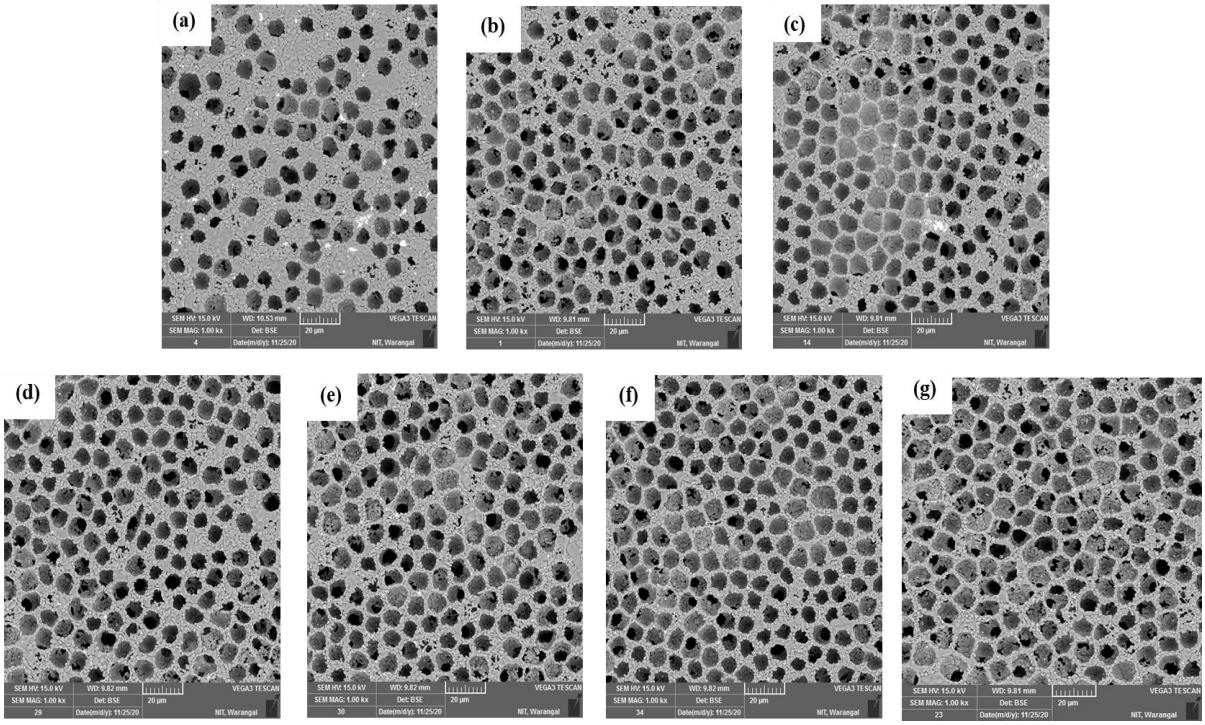

Fig 7.7 *SEM images of 10 micron size beads at different volume percentage in ZTA powder (a) 20Vol% (b) 30Vol% (c) 40Vol% (d) 50Vol% (e) 60Vol% (f) 70Vol% (g) 80Vol%.*

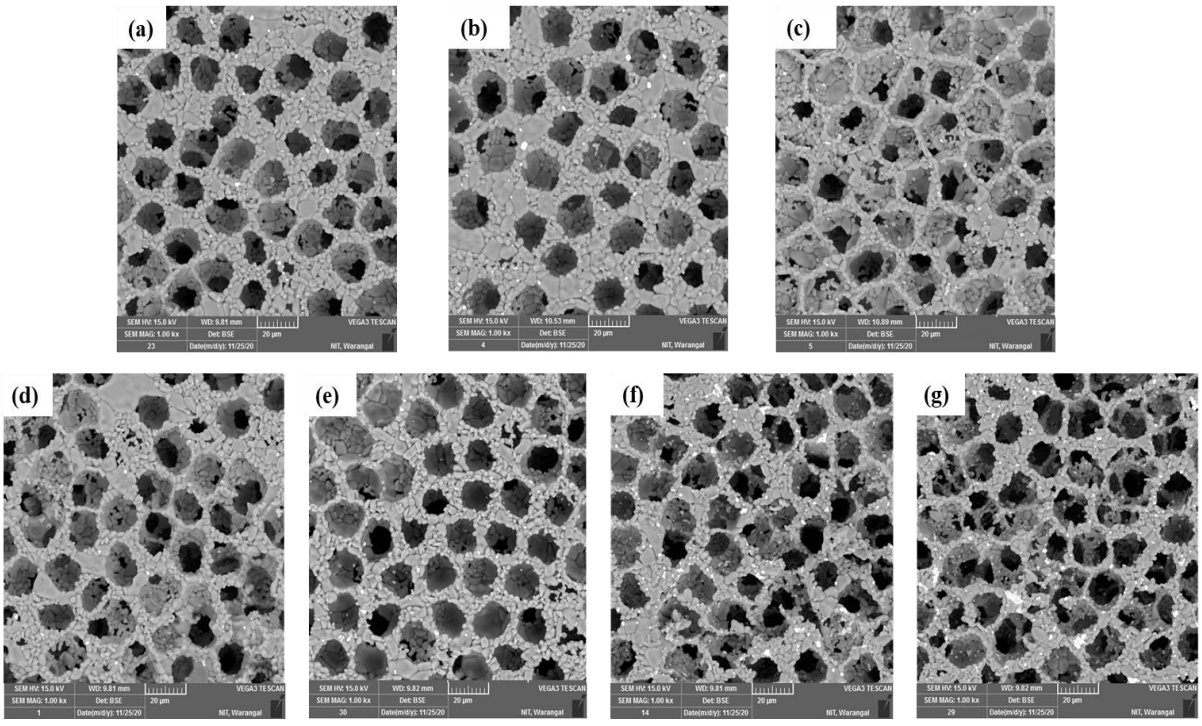

Fig 7.8 *SEM images of 20 micron size beads at different volume percentage in ZTA powder (a) 20Vol% (b) 30Vol% (c) 40Vol% (d) 50Vol% (e) 60Vol% (f) 70Vol% (g) 80Vol% .*

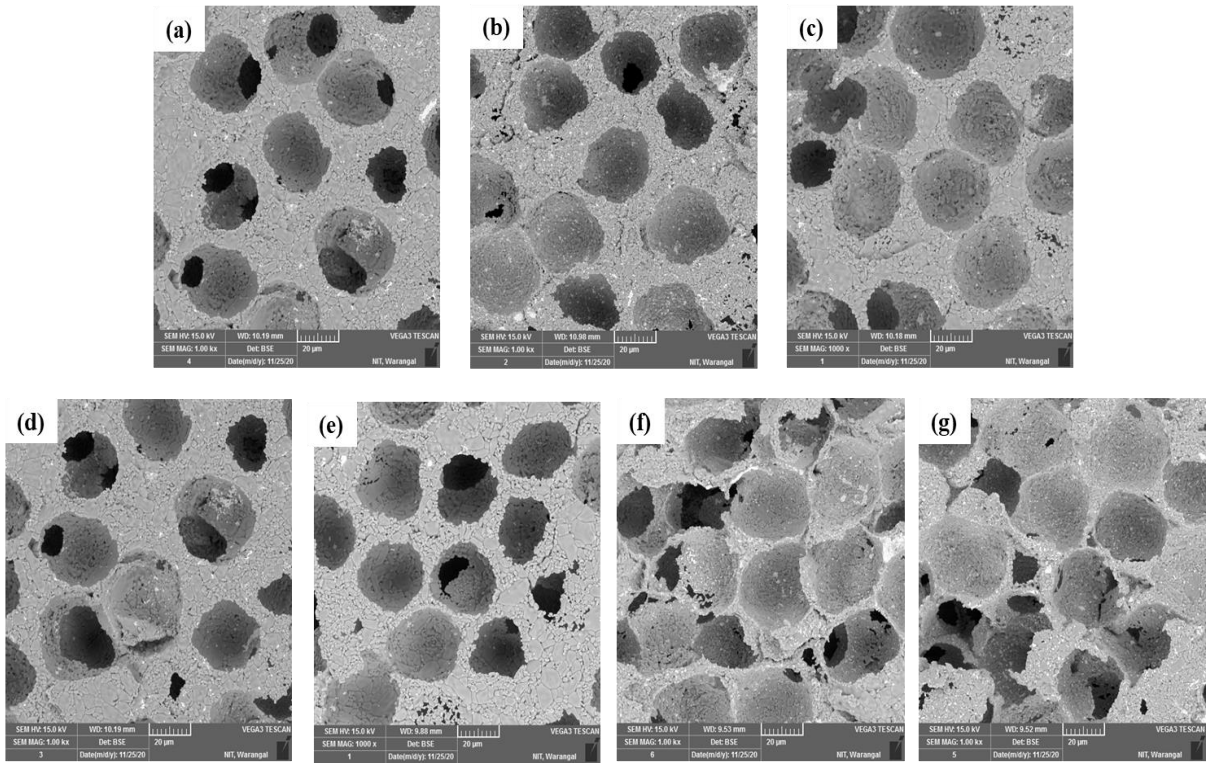

Fig 7.9 *SEM images of 40 micron size beads at different volume percentage in ZTA powder (a) 20Vol% (b) 30Vol% (c) 40Vol% (d) 50Vol% (e) 60Vol% (f) 70Vol% (g) 80Vol%.*

7.5 Mechanical properties analysis

All the fabricated Al_2O_3 and ZTA samples show similar kind of failure beahviour. Because of certain constraints, we reported limited samples of stress-strain curves. The low porosity samples stress-strain curves show an elastic behaviour up to a sudden rupture. On the other hand, the highly porous samples showed typical behavior of ceramic foams. After an initial linear phase, a plateau characterized the stress-strain curve due to a progressive collapse of the solid phase by fracturing the solid walls between pores. The load drops noted in the plateau phase can be associated with the propagation of small cracks in the ceramic, either by wall bending or buckling. The maximum load reached during the test was used to calculate the compressive strength of the porous material. The compressive values are strongly dependent on the porosity of the sample. When porosity increases, the compressive strength decreases. Fig 7.10 shows the stress-strain curves, 20 Vol% samples showed higher compressive values with complete ceramic failure. By increasing beads volume %, the compressive strength values decreased and the failure phenomena changed from ceramic to open pore cellular structure. The comparison between the compression strength values vs porosity vs % beads added to the powder is shown in Fig 7.11. When volume % of beads increased from 20 Vol% to 80 Vol%, the porosity and compressive values were 21.9, 23.5, 24.3, 31.5, 37.9, 40, 65% and 658, 480, 217, 170, 43.5, 17.5, 12.6 MPa respectively. The porosity of the samples increased based on

the pore size i.e., 40 µm pore sample had higher porosity than 20 µm and 10 µm pore size samples at similar volume %. Table. 7.1 represents the compressive values with respect to different porosities

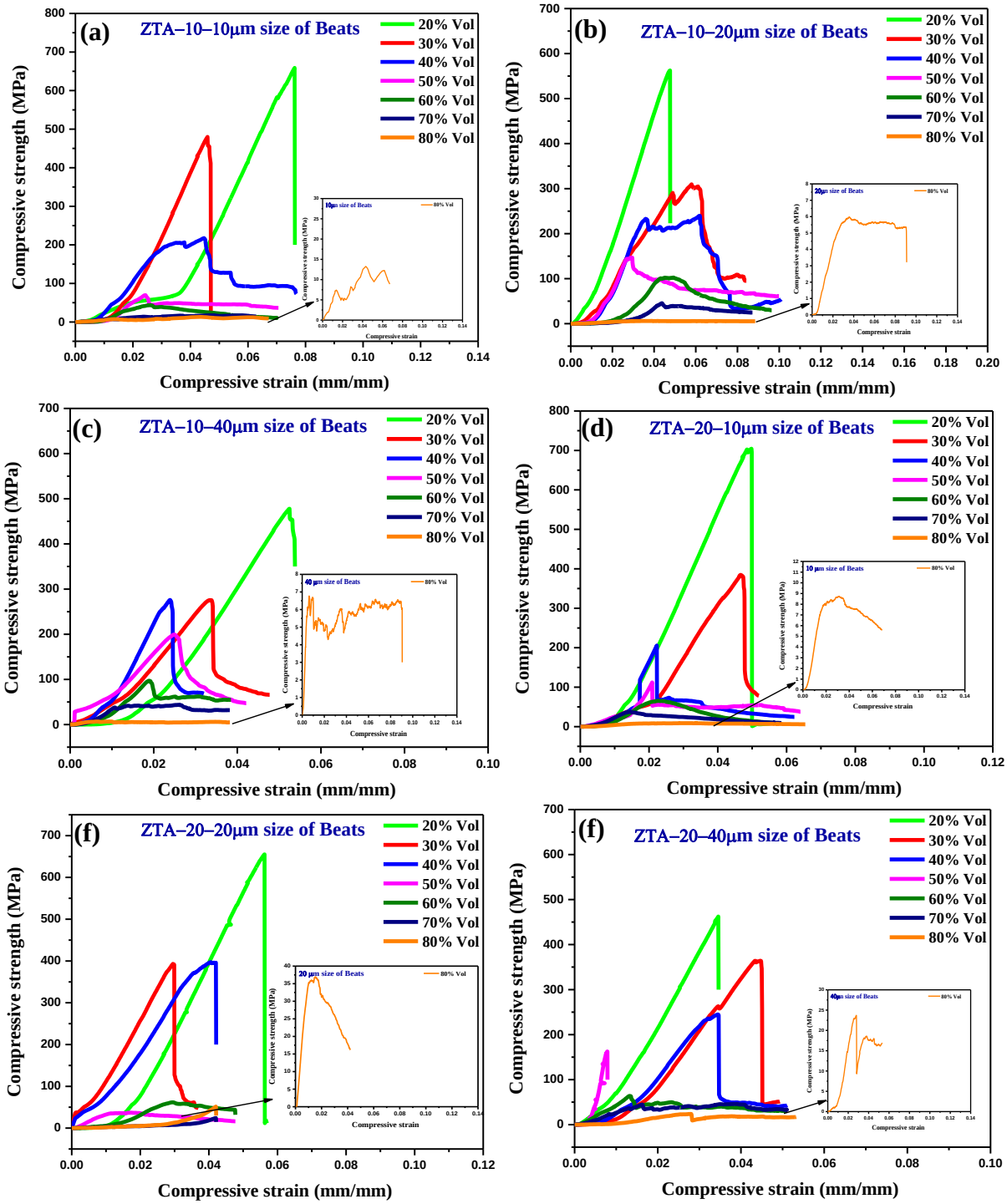

Fig.7.10 *Compressive stress vs strain curves with different %volumes (a) ZTA-10-10 µm (b) ZTA-10-20 µm and (c) ZTA-10-40 µm (d) ZTA-20-10 µm (e) ZTA-20-20 µm (f) ZTA-20-40 µm.*

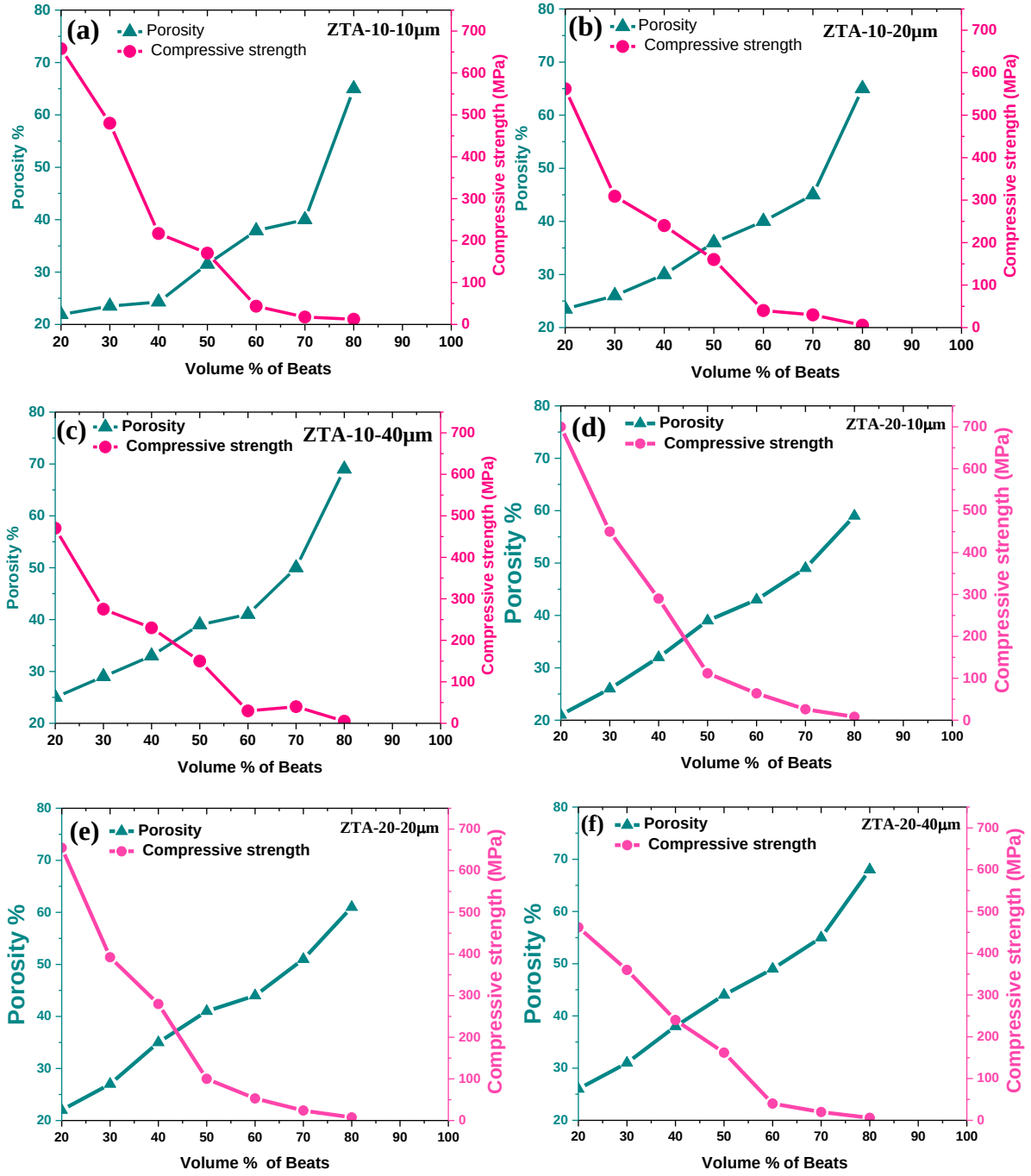

Fig. 7.11 *Compressive strength vs porosity with different %volumes (a) ZTA-10-10 µm (b) ZTA-10-20 µm and (c) ZTA-10-40 µm (d) ZTA-20-10 µm (e) ZTA-20-20 µm (f) ZTA-20-40 µm*

Table. 7.1 represents the compressive values with respect to different porosities.

		Alumina		ZTA-5		ZTA-10		ZTA-15		ZTA-20	
Beads Size (µm)	Vol (%)	Porosity (%)	Compression strenhth (MPa)	Porosity (%)	Compressi on strenhth (MPa)	Porosity (%)	Compressio n strength (MPa)	Porosity (%)	Compression strength (MPa)	Porosity (%)	Compression strength (MPa)
10	20	16.2	720	20	670	21.9	658	20	660	21	700
	30	18.1	500	22.1	490	23.5	480	22.3	470	26	450
	40	21.9	320	23.4	300	24.3	217	25.3	300	32	290
	50	23.5	250	31	200	31.5	170	30.3	180.5	39	112
	60	24.3	80	36	52	37.9	43.5	40.8	40	43	64
	70	31.5	50.2	41	20	40	17.5	43	21.2	49	26
	80	37.9	20	64.2	15.2	65	12.6	63	10.6	59	8
20	20	22.2	590	22	580	23.5	562	20.3	550	22	555
	30	26	479	25.9	460	26	309	25.2	320	27	392
	40	36.5	397	34	270	30	240	33.4	260	35	280
	50	37.5	302	35.2	180	36	160	37	150	41	100
	60	43.3	269	41.2	70	40	40	43.8	35	44	53
	70	44.2	222	43	35	45	30	49	26.5	51	24
	80	46.8	180	64	7.3	65	5.6	68	8.2	61	7.5
40	20	23	480	26	450	25	470	29	465	26	462
	30	31.8	405	32	290	29	275	25	280	31	360
	40	37.9	352	35.2	250	33	230	35	220	38	240
	50	39.9	295	40.2	170	39	150	40	140.5	44	162
	60	44	243	45.8	49	41	50	51	48	49	40
	70	45	201	46	35	50	40	55	35	55	20
	80	48.5	185	47.2	8	69	5	70	5.2	68	6

7.6 Summary:

The compressive strength values of Al_2O_3 and ZTA samples with varying porosity from 20% to 70% were investigated by control of porosity and micropore size. The micropore size 10µm to 40µm can be easily fabricated by the control of the size of polystyrene beads. A sample with small micropores shows higher compressive strength than those with large micropores. Alumina foams showing higher compressive values compare to ZTA foams. Al_2O_3, ZTA-5, ZTA-10, ZTA-15, and ZTA-20 foam with 10µm micropores sample showed higher compressive strength values when compared to 20µm and 40µm micropores samples. The compressive strength values at 20Vol% to 80Vol% are 720MPa, 670MPa, 658MPa, 660MPa, 680MPa & 590MPa, 580MPa, 562MPa, 550MPa, 555MPa and 480 MPa,450 MPa,470 MPa,465 MPa, 462MPa for 10µm, 20µm and 40µm, respectively.

Chapter- 8

Deformation study through simulation

This chapter describes the deformation study of the open-cell ceramic foam through simulation. In this process, we discussed the design of a CAD model of open-cell foam for simulation using mimics software. These simulation results were compared with experimental results. The details of the CAD model design steps are discussed in chapter 3.

8.1 Experimental and Numerical validation of ceramic foam

X-ray and 2D computed tomography are conventional methods for observing ceramic bone geometry. Therefore, these conventional methods are not much informative. Advances in imaging technology such as computed tomography (CT) and Magnetic resonance imaging (MRI) play a vital role in visualizing and analyzing the scanned data. The CT data is useful for constructing CAD models with advanced imaging software such as MIMICS, Invesalius, and 3D slicer.

Mimics is adequate software for processing medical images to 3D CAD models. Mimics works on image processing algorithms that convert the computed tomography (CT) and magnetic resonance imaging (MRI) to CAD data. The CAD data is further processed for producing functional prototypes with 3D printing technologies, and this data can be used in advanced engineering analysis such as Ansys and Abaqus.

In academic and research fields, Mimics plays a vital role to process image data into 3D models and link the models to rapid prototyping (RP), computer-aided engineering (CAE), computer-aided design (CAD), and surgery planning.

In mimics, a stack of images like x-ray data is imported, and the image consists of three planes XY, YZ, and ZX. These planes are named Axial, Coronal, and Sagittal planes. The process of conversion of image data into 3d models is called segmentation. The region of interest can be sliced from the image data during segmentation. This data is further processed to develop a 3D model that can be represented in STL file format. The STL file format is the most common in rapid prototyping. The STL format allows describing the most complex geometries accurately in triangular data. The STL is a tessellation of triangles, and each triangle contains three nodes and one normal direction.

In the process of CAD modeling, STL data is exported to computer-aided design and computer-aided manufacturing (CAD/CAM) systems for preoperative processes such as wrapping, fitting errors, and shape. The integration of computer-aided design (CAD) and medical images allows to development of CAD models.

8.2 Materials and methods

The total work is discussed in six steps: scanning the specimen in Micro-CT, reading DICOM images, thresholding, converting to STL file, STL to CAD model, and finite element analysis. The total workflow is represented in Fig. 8.1.

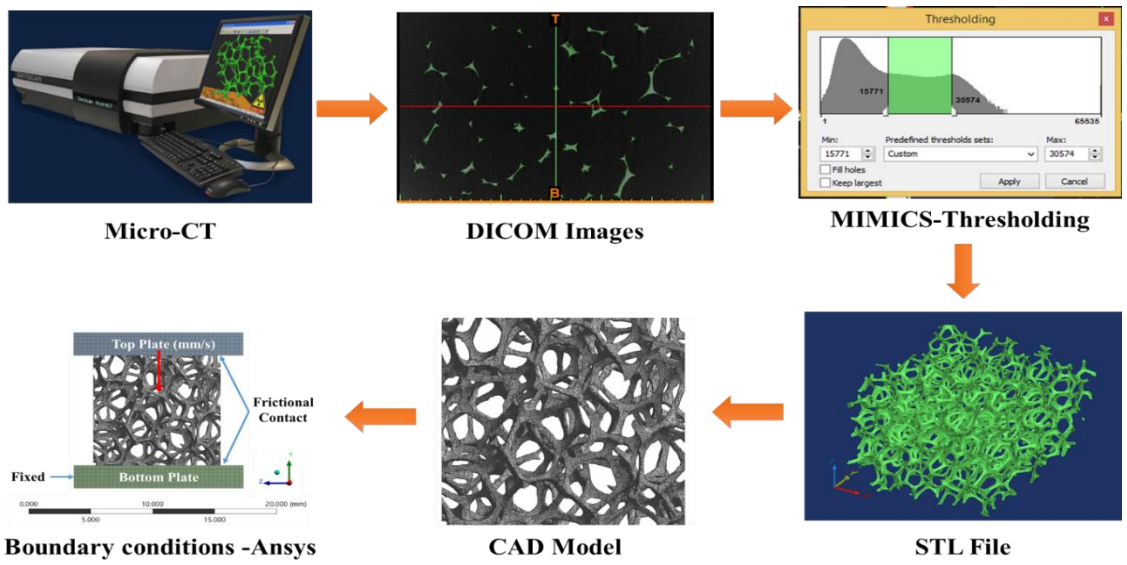

Fig.8.1 *Procedure to manufacture medical models.*

8.2.1 Scanning the foam in Micro-CT

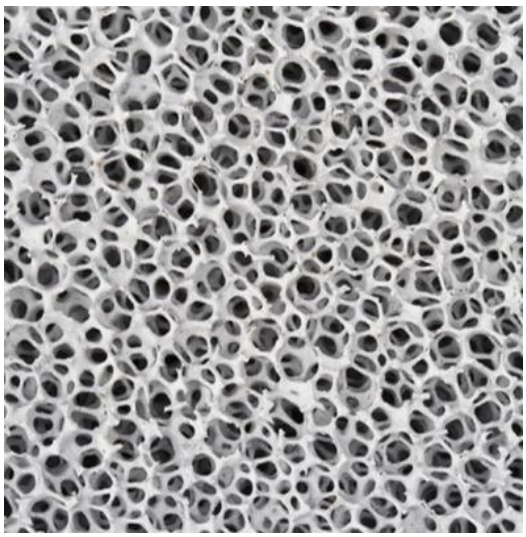

Fig. 8.2 *Alumina ceramic foam.*

Fig. 8.2 shows the 10 PPI alumina ceramic foam scanned under a micro CT-scan with several slices was 605, and the thickness of each slice was 0.05 mm. The scanned data was imported to MIMICS software to convert the image data into an STL file.

8.2.2 CT image processing through MIMICS software

Advances in computer graphics such as image processing are revolutionizing medical imaging technology. The image processing is to convert the CT data to 3D Models. They are visualized at different views/orientations with varying colours, lighting, and surface properties, as shown in Fig. 8.3. In this research, the medical imaging software MIMICS was used for processing CT scan data. The MIMICS software can handle DICOM and other image formats, including TIFF, JPEG, PNG, GIF, and BMP. The software is extensively capable of working with CT, MRI. 3D image processing, image resizing, and image reslicing are the essential features of this software. Other essential features such as thresholding/segmentation, region growing, rotation, scaling, reslicing, measurements, editing, examining three-dimensional volumetric data, assigning different object names for various tissues, and the capability of visualizing the objects either individually or together. The software can export 3D digital object in a compatible format, i.e. STL format. 3D reconstruction of foam-MIMICS. Converting scanned data from 2D CT images to 3D models is called segmentation. This segmentation consists of:

- Creation of an image data set
- Thresholding and 3D reconstruction

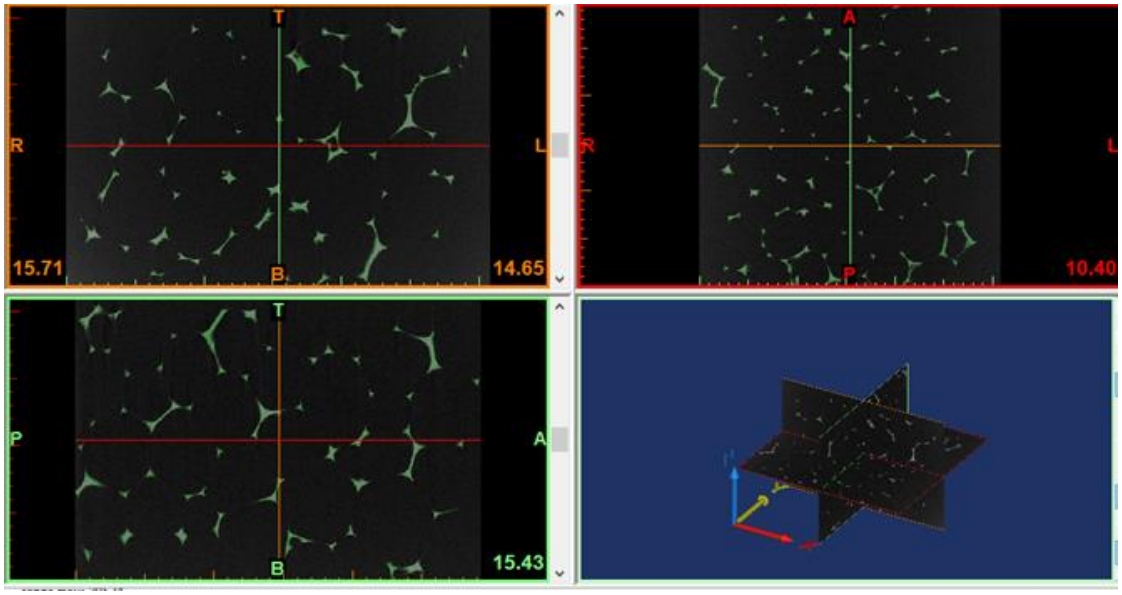

Fig. 8.3 *CT image processing and various views.*

8.2.3 Creation of image datasets

A list is created with the relevant image slices pertaining to the pathology from the files' DICOM directory. Fig.8.4 shows images in three orientations: axial, sagittal, and coronal with a space to display the reconstructed 3D image. The images have a 512 X 512-pixel resolution.

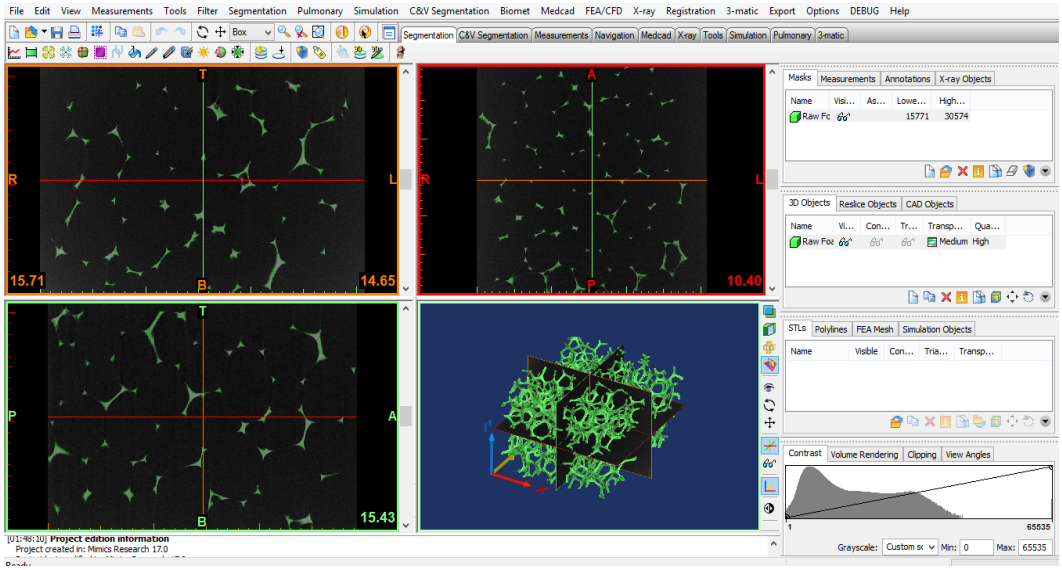

Fig. 8.4 *3D Reconstruction of foam.*

8.2.4 Thresholding and 3D reconstruction

To analyze objects in an image, it is essential to distinguish between the objects of interest from "the rest". The techniques used to find the objects of interest are segmenting the foreground from the background. Segmentation of CT 2D slice images is done by selecting specific image intensities (Hounsfield units) within the range. The use of Hounsfield units indicates the nature of the ceramic foams being imaged.

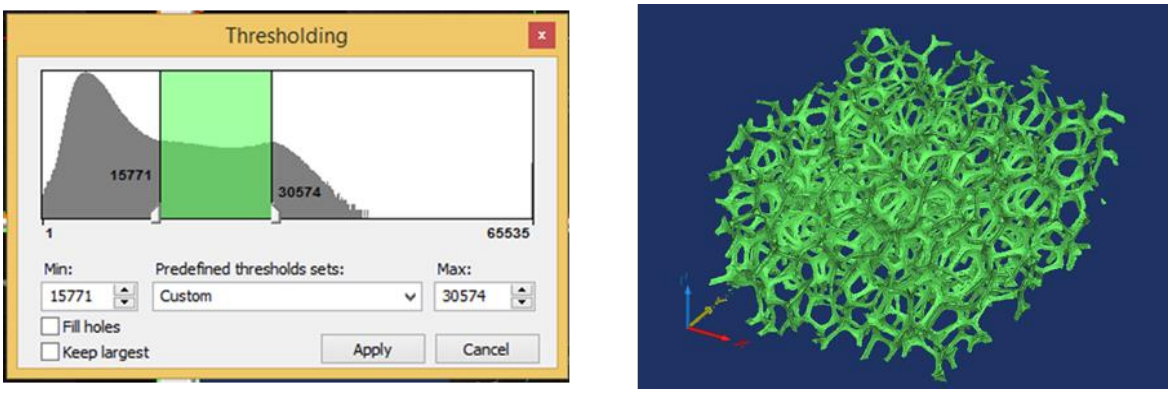

Fig. 8.5 *a) Thresholding toolbar for different biological materials b) 3D reconstruction.*

Thresholding is done by selecting the upper and lower threshold values of image intensities. The scanned objects are identified by Hounsfield units (HU), a system to measure the attenuation coefficient of scanned objects in CT images. The strut of foam has a higher Hounsfield value because it absorbs most of the radiation. The thresholding toolbar has a predefined scale for observing scanned images such as ceramics, bone, soft tissue, etc. In this work, the threshold value of ceramic foam is 15771 min to 30574 max is selected, as shown in

Fig. 8.5a. Calculate 3D tool convert 2D CT image data to 3D model as shown in Fig.8.5b. The sharp edges and foam pieces are erased at different CT images layers through successive steps.

8.2.5 STL to CAD model conversion

The alumina specimen was scanned through the micro-CT (X-ray computed tomography) to get the x-ray data in a layer-by-layer fashion. The Computed tomography (CT) gives pixel data in an image format like jpeg and png etc. The CT data were processed through the MIMICS software, converting CT data to voxel data. This voxel data helps to develop the 3D CAD model. MIMICS can convert CT data to STL file. The STL stands for standard tessellation language, and it contains triangular data. STL file (Standard Tessellation Language) is edited in Ansys Space Claim software for correcting errors such as removing intersection triangles and smoothening the sharp edges. For numerical analysis, STL file is cropped to 20*20*20 mm. The final STL file was converted to CAD model, i.e. a solid model for structural analysis, as shown in Fig. 8.6.

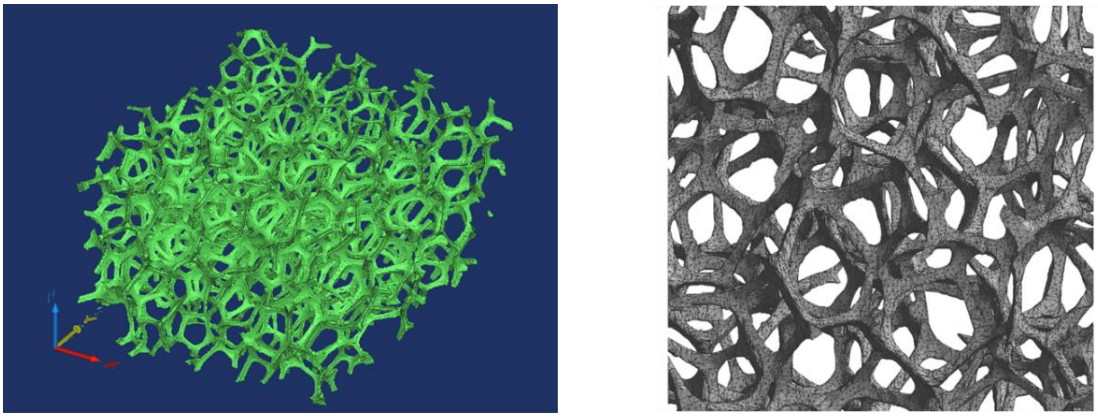

Fig. 8.6 *a) STL file b) CAD model.*

8.2.6 Meshing AND Mechanical Properties

The foam model is placed between rigid plates, the top one is movable with a velocity of 0.1 mm/s, while the bottom is fixed. The model is considered isotropic, homogeneous, and elastic. The foam was fine-meshed with 10-node tetrahedral elements until appropriate mesh size; however, the mesh consists of 393687 elements. The adequate mesh size and 10-node tetrahedral elements can effectively mesh the sharp and curved edges, as shown in Fig. 8.7.

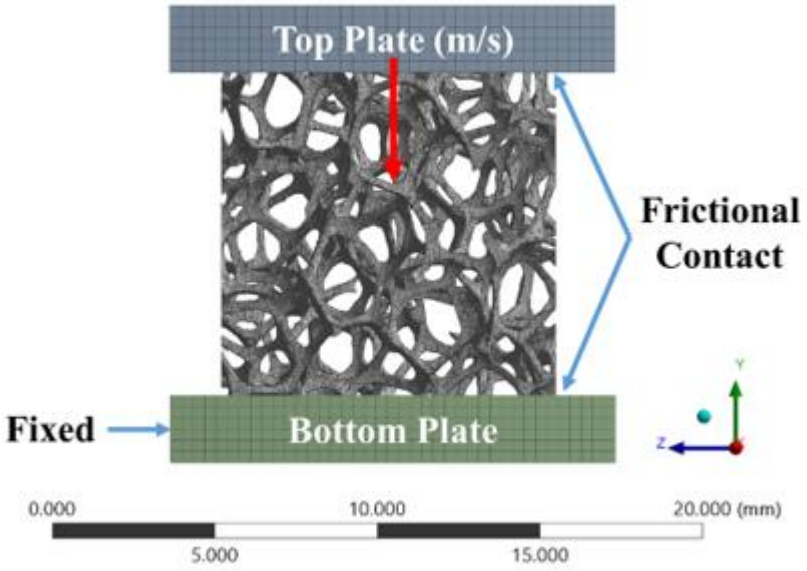

Fig. 8.7 *Meshing and boundary conditions of foam in Ansys.*

The foam's mechanical properties were considered to conduct numerical analysis with density ρ = 3650 kg/m3, Young's modulus E = 350 GPa, Poisson's ratio ν = 0.21, and compressive ultimate strength 2100 MPa.

8.3 Deformation of the Foam

The foam is compressed between two plates, which results in foam failed as brittle, and strut failures are shown in the figure. Due to the top plate's incremental velocity, the stress propagates from the top surface to the plate's bottom. The red colour indicates a high amount of stress is concentrated, which leads to the strut's failure. Initially, the failure started from the foam's top surface, which is the contact portion between the foam's top plate and surface.

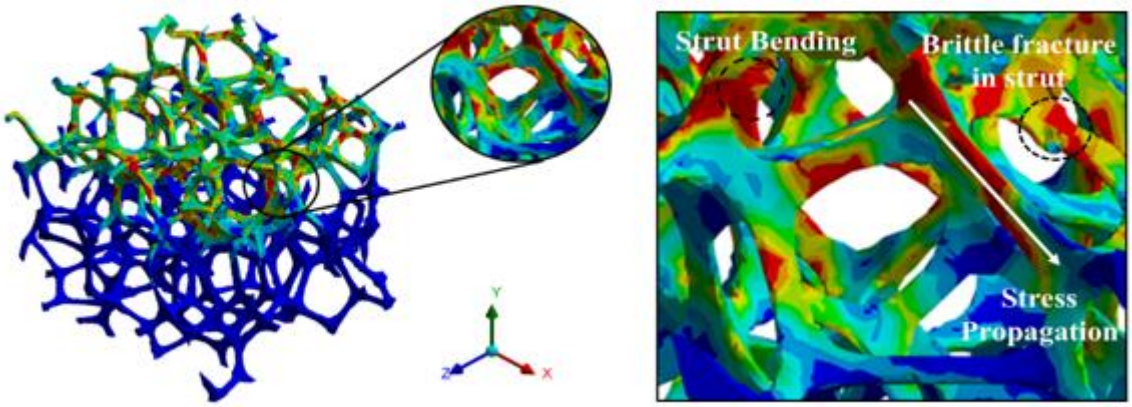

Fig.8. 8 *a) Sample failure b) microscopical view of stress propagation, strut bending and fracture.*

The foam is gradually deformed under the loading conditions shown in Fig. 8.8a. The ceramic foams are brittle; the capturing of failure is done microscopically. The microscopical view shows the strut bending, stress propagation, and fracturing, as shown in Fig. 8.8b. From the figure, most of the struts are failed as brittle materials, and few are taking max bending stress like bending dominated structures. The strut is bending then failure has occurred as a brittle material from the figure. The line shows that the stress propagation along the strut.

8.4 Experimental vs Numerical results

The foam model's deformation behaviour was analyzed through computational simulation and the experimental and numerical results of the specimen were compared as shown in Fig. 8.9. The numerical analysis model is considered isotropic, homogeneous, and elastic. Due to that, the numerical data shows linearity. The experimental line shows the non-linearity. The simulation and experimental results are not consistent because the specimen is not isotropic. The experimental stress-strain curve is divided into region A (≤ 0.4 strain) and region B (≥ 0.4 strain). Region A represents strut bending and region B represents slight densification of the foam. Initially, the numerical simulation slope is higher than the experimental and the resulting values of numerical simulation are slightly higher than that of the experiment. However, the failure point of experimental and numerical values are met at 0.0611 strain and 0.656679 MPa, as shown in Fig.8.9 and Table 1. Finally, the experimental and numerical results indicate that cracks more easily form in the struts' weak region during the compression process.

Table 8.1 *Experimental and numerical simulation results*

Experimental		**Numerical**	
Strain	**Stress**	**Strain**	**Stress**
0	0	0.00000	0
0.00888	0.02509	0.00233	0.025579
0.01295	0.051143	0.00472	0.051118
0.02043	0.102587	0.00944	0.102312
0.02799	0.15349	0.01415	0.153646
0.03528	0.205355	0.01885	0.205056
0.04217	0.256438	0.02354	0.256368
0.04484	0.305776	0.02823	0.307776
0.04744	0.361492	0.03293	0.36184
0.04983	0.414681	0.03779	0.4144
0.05193	0.465704	0.04253	0.46608
0.05432	0.518532	0.04726	0.519008
0.05581	0.555054	0.05201	0.555792
0.0589	**0.606558**	**0.05675**	**0.607792**
0.0611	**0.656679**	**0.06148**	**0.657232**
0.06249	0.676173	0.06626	0.723984

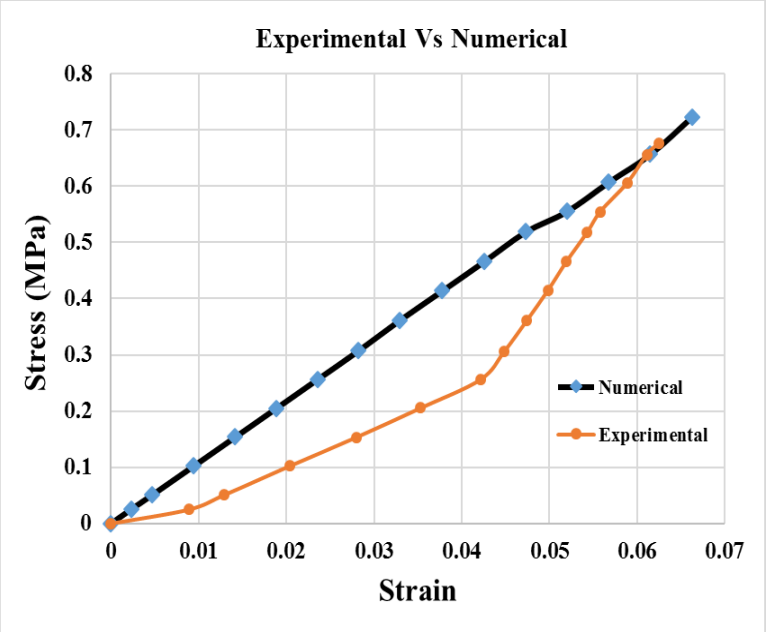

Fig.8.9 *Experimental and numerical simulation graph.*

8.5 Summary

The mechanical properties such as compressive strength and young's modulus depend on the alumina foams' pore size and porosity. However, the strut thickness plays a role in the foams' strength. The alumina foam is collapsed layer-by-layer fashion and the stress is highly concentrated at weak struts. The experimental results are divided into strut bending and slight densification. Finally, the numerical simulation results are slightly higher than the experimental results; however, the failure point is matched at 0.0611 strain.

Chapter 9

Conclusions and future scope

This chapter summarizes the significant findings, concludes the outcomes of the research work carried out, and presents the scope for future work.

- The sponge replication technique was used to fabricate an open-cell Al_2O_3 and ZTA foams (10PPI, 20PPI, 30PPI). The fabricated samples were subjected to infiltration with molten aluminium, encapsulated, and then infiltrated with polymer to make a metal and polymer composite. 10PPI metal infiltrated foam showed better mechanical properties compared to all other foams.
- Al_2O_3 and ZTA foams were successfully fabricated using the thermo-foaming method with different powder to sucrose weight ratios ($W_{P/S}$ =0.6 to 1.4). The compressive strength (σ), bending strength, and fracture toughness of the foams were then evaluated. Maximum compressive strength of 1.9 MPa was observed for Al_2O_3 foam while it was 1.8 MPa in case of ZTA at $W_{P/S}$ value of 1.2.
- ZTA samples showed better bending strength and fracture toughness than Al_2O_3 foams irrespective of $W_{P/S,}$ and the corresponding values are 1.2 MPa and 136 MPa $m^{1/2}$. The improved bending strength and fracture toughness of ZTA is attributed to the transformation toughening mechanism.
- Closed-cell foams were fabricated successfully by space holder technique. The compressive strength values of Al_2O_3 and ZTA samples of varying porosity from 20% to 70% were investigated by controlling porosity and micropore size. The samples with smaller micropores showed higher compressive strength than those with larger micropores.
- The simulation study was used to understand the failure behaviour of alumina foam at quasistatic conditions. The alumina foam was collapsed layer-by-layer, and the stress was highly concentrated at weak struts. The experimental results were divided into strut bending and slight densification categories. Finally, the numerical simulation results were found to be slightly higher than the experimental results; however, the failure point matched well at 0.0611 strain.

9.1 Future scope

As discussed in the previous chapters, Al_2O_3 and ZTA porous ceramics are developed, physical and mechanical properties are evaluated. However, to use these materials for commercial applications, further analysis/development is required as discussed below.

1) Fabrication and property evaluation of different pore sizes i.e. 50PPI to 80PPI foams.
2) A thermal conductivity study is required to analyze the heat loss effect with respect to the pore size and porosity.
3) Water or gas permeability measurements for these macroporous ceramics need to be studied in order to ascertain their interconnectivity.
4) To develop ZTA porous structures to understand biocompatibility more precisely.
5) *In vitro* and *In vivo* studies of developed porous structures used as scaffolds for tissue engineering can be done.

References:

[1] L.J. Gibson, M.F. Ashby, Cellular Solids: Structure and Properties, 2nd ed., Cambridge University Press, Cambridge, 1997. doi:DOI: 10.1017/CBO9781139878326.

[2] M.F. Ashby, D.R.H. Jones, The light alloys, 1998. doi:10.1016/b978-0-08-054565-3.50013-7.

[3] I.J. McColm, Ceramic Science for Materials Technologists, Hill, 1983. https://books.google.co.in/books?id=CeuTzQEACAAJ.

[4] J.-F. Li, R. Watanabe, Fracture Toughness of Al2O_3-Particle-Dispersed Y_2O_3-Partially Stabilized Zirconia, J. Am. Ceram. Soc. 78 (1995) 1079–1082. doi:https://doi.org/10.1111/j.1151-2916.1995.tb08441.x.

[5] F. Kern, P. Palmero, Microstructure and mechanical properties of alumina 5 vol% zirconia nanocomposites prepared by powder coating and powder mixing routes, Ceram. Int. 39 (2013) 673–682. doi:10.1016/j.ceramint.2012.06.078.

[6] R.C. GARVIE, R.H. HANNINK, R.T. PASCOE, Ceramic steel?, Nature. 258 (1975) 703–704. doi:10.1038/258703a0.

[7] O.S. Abd El-Ghany, A.H. Sherief, Zirconia based ceramics, some clinical and biological aspects: Review, Futur. Dent. J. 2 (2016) 55–64. doi:10.1016/j.fdj.2016.10.002.

[8] R.H.J. Hannink, P.M. Kelly, B.C. Muddle, Transformation toughening in zirconia-containing ceramics, J. Am. Ceram. Soc. 83 (2000) 461–487. doi:10.1111/j.1151-2916.2000.tb01221.x.

[9] E.C. Subbarao, H.S. Maiti, K.K. Srivastava, Martensitic transformation in zirconia, Phys. Status Solidi. 21 (1974) 9–40. doi:10.1002/pssa.2210210102.

[10] G. Teufer, The crystal structure of tetragonal ZrO_2, Acta Crystallogr. 15 (1962) 1187. doi:10.1107/S0365110X62003114.

[11] P.O.L. Duwez, F. Odell, F.H. Brown Jr., Stabilization of Zirconia with Calcia and Magnesia, J. Am. Ceram. Soc. 35 (1952) 107–113. doi:10.1111/j.1151-2916.1952.tb13081.x.

[12] R.C. Garvie, P.S. Nicholson, Phase Analysis in Zirconia Systems, J. Am. Ceram. Soc. 55 (1972) 303–305. doi:10.1111/j.1151-2916.1972.tb11290.x.

[13] P. Li, I.W.W. Chen, J.E. Penner Hahn, Effect of Dopants on Zirconia Stabilization—An X-ray Absorption Study: I, Trivalent dopants, J. Am. Ceram. Soc. 77 (1994) 1289–1295. doi:10.1111/j.1151-2916.1994.tb05404.x.

[14] A. Navrotsky, Thermochemical insights into refractory ceramic materials based on oxides with large tetravalent cations, J. Mater. Chem. 15 (2005) 1883–1890. doi:10.1039/b417143h.

[15] F.F. Lange, Transformation toughening - Part 1 Size effects associated with the thermodynamics of constrained transformations, J. Mater. Sci. 17 (1982) 225–234. doi:10.1007/BF00809057.

[16] C. Piconi, G. Maccauro, Zirconia as a ceramic biomaterial, Biomaterials. 20 (1999) 1–25. doi:10.1016/S0142-9612(98)00010-6.

[17] A.R. Studart, U.T. Gonzenbach, E. Tervoort, L.J. Gauckler, Processing Routes to Macroporous Ceramics: A Review, J. Am. Ceram. Soc. 89 (2006) 1771–1789. doi:https://doi.org/10.1111/j.1551-2916.2006.01044.x.

[18] D. Kuang, A. Xu, J. Zhu, H. Liu, B. Kang, Fabrication of ordered macroporous rutile titania at low temperature, New J. Chem. 26 (2002) 819–821. doi:10.1039/b201245f.

[19] N. Paşayev, S. Kocatepe, N. Maraş, M. Soylak, M. Erol, Investigation some characteristics of chicken feather's rachis, IOP Conf. Ser. Mater. Sci. Eng. 254 (2017). doi:10.1088/1757-899X/254/19/192013.

[20] G. Qiao, R. Ma, N. Cai, C. Zhang, Z. Jin, Mechanical properties and microstructure of Si/SiC materials derived from native wood, Mater. Sci. Eng. A. 323 (2002) 301–305.

[21] L.J. Gibson, The hierarchical structure and mechanics of plant materials, J. R. Soc. Interface. 9 (2012) 2749–2766. doi:10.1098/rsif.2012.0341.
[22] I. Miranda, J. Gominho, H. Pereira, Cellular structure and chemical composition of cork from the Chinese cork oak (Quercus variabilis), J. Wood Sci. 59 (2013) 1–9. doi:10.1007/s10086-012-1300-8.
[23] Y. Bienvenu, Application and future of solid foams, Comptes Rendus Phys. 15 (2014) 719–730. doi:10.1016/j.crhy.2014.09.006.
[24] X. Liu, C.L. Martin, D. Bouvard, S. Di Iorio, J. Laurencin, G. Delette, Strength of Highly Porous Ceramic Electrodes, J. Am. Ceram. Soc. 94 (2011) 3500–3508. doi:https://doi.org/10.1111/j.1551-2916.2011.04669.x.
[25] L. Salvo, G. Martin, M. Suard, A. Marmottant, R. Dendievel, J.J. Blandin, Processing and structures of solids foams, Comptes Rendus Phys. 15 (2014) 662–673. doi:10.1016/j.crhy.2014.10.006.
[26] J. Binner, Ceramics Foams, Cell. Ceram. (2005) 31–56. doi:https://doi.org/10.1002/3527606696.ch2a.
[27] A.R. Studart, U.T. Gonzenbach, E. Tervoort, L.J. Gauckler, Processing routes to macroporous ceramics: A review, J. Am. Ceram. Soc. 89 (2006) 1771–1789. doi:10.1111/j.1551-2916.2006.01044.x.
[28] Q.Z. Chen, I.D. Thompson, A.R. Boccaccini, 45S5 Bioglass®-derived glass–ceramic scaffolds for bone tissue engineering, Biomaterials. 27 (2006) 2414–2425. doi:https://doi.org/10.1016/j.biomaterials.2005.11.025.
[29] M. Scheffler, P. Colombo, Cellular Ceramics: Structure, Manufacturing, Properties and Applications, 2005. doi:10.1002/3527606696.
[30] W.D. Callister, Materials science and engineering: An introduction (2nd edition), Mater. Des. 12 (1991) 59. doi:10.1016/0261-3069(91)90101-9.
[31] G. Liu, Fabrication of porous ceramics and composites by a novel freeze casting process, Measurement. (2011) 247.
[32] L.J. Gibson, M.F. Ashby, Lorna J. Gibson, Michael F. Ashby-Cellular Solids_ Structure and Properties (Cambridge Solid State Science Series) -Cambridge University Press (1999).pdf, (1999).
[33] J. Banhart, Manufacture, characterisation and application of cellular metals and metal foams, Prog. Mater. Sci. 46 (2001) 559–632. doi:10.1016/S0079-6425(00)00002-5.
[34] D. King, C. Carey, O. Inderwildi, Advanced aerospace materials : past , present and future Since Orville and Wilbur Wright first decided to power their Flyer with a, Aviat. Environ. (2009) 22–27.
[35] J. Rouquerol, D. Avnir, D.H. Everett, C. Fairbridge, M. Haynes, N. Pernicone, J.D.F. Ramsay, K.S.W. Sing, K.K. Unger, Guidelines for the Characterization of Porous Solids, in: J. Rouquerol, F. Rodríguez-Reinoso, K.S.W. Sing, K.K.B.T.-S. in S.S. and C. Unger (Eds.), Charact. Porous Solids III, Elsevier, 1994: pp. 1–9. doi:https://doi.org/10.1016/S0167-2991(08)63059-1.
[36] R. Brezny, D.J. Green, Uniaxial Strength Behavior of Brittle Cellular Materials, J. Am. Ceram. Soc. 76 (1993) 2185–2192. doi:10.1111/j.1151-2916.1993.tb07753.x.
[37] M.F. Ashby, R.F.M. Medalist, The mechanical properties of cellular solids, Metall. Trans. A. 14 (1983) 1755–1769. doi:10.1007/BF02645546.
[38] R.F.S. C. Korner, Metal Matrix Composites and Metallic Foams.Pdf, 2000. doi:10.1002/adem.201200217.
[39] L. Sarkisov, Accessible Surface Area of Porous Materials: Understanding Theoretical Limits, Adv. Mater. 24 (2012) 3130–3133. doi:https://doi.org/10.1002/adma.201104708.
[40] X. Liang, A.W. Weimer, An overview of highly porous oxide films with tunable thickness prepared by molecular layer deposition, Curr. Opin. Solid State Mater. Sci. 19

(2015) 115–125. doi:10.1016/j.cossms.2014.08.002.
[41] W. Liu, J. Xu, Y. Wang, H. Xu, X. Xi, J. Yang, Processing and properties of porous PZT ceramics from particle-stabilized foams via gel casting, J. Am. Ceram. Soc. 96 (2013) 1827–1831. doi:10.1111/jace.12250.
[42] S. Ackermann, J.R. Scheffe, J. Duss, A. Steinfeld, Morphological Characterization and Effective Thermal Conductivity of Dual-Scale Reticulated Porous Structures., Mater. (Basel, Switzerland). 7 (2014) 7173–7195. doi:10.3390/ma7117173.
[43] M. Song, R. Viskanta, Flow characteristics of anisotropic structures constructed with porous layers, Transp. Porous Media. 15 (1994) 151–173.
[44] D.F. Heaney, J.D. Gurosik, C. Binet, Isotropic forming of porous structures via metal injection molding, J. Mater. Sci. 40 (2005) 973–981. doi:10.1007/s10853-005-6516-1.
[45] H. Nakajima, T. Ikeda, S.K. Hyun, Fabrication of Lotus-type Porous Metals and their Physical Properties, Adv. Eng. Mater. 6 (2004) 377–384. doi:https://doi.org/10.1002/adem.200405149.
[46] A. Wiest, C.A. Macdougall, R.D. Conner, Optimization of cellular solids for energy absorption, Scr. Mater. 84–85 (2014) 7–10. doi:10.1016/j.scriptamat.2014.02.013.
[47] D. Mousanezhad, R. Ghosh, A. Ajdari, A.M.S. Hamouda, H. Nayeb-Hashemi, A. Vaziri, Impact resistance and energy absorption of regular and functionally graded hexagonal honeycombs with cell wall material strain hardening, Int. J. Mech. Sci. 89 (2014) 413–422. doi:10.1016/j.ijmecsci.2014.10.012.
[48] E.C. Hammel, O.L.R. Ighodaro, O.I. Okoli, Processing and properties of advanced porous ceramics: An application based review, Ceram. Int. 40 (2014) 15351–15370. doi:10.1016/j.ceramint.2014.06.095.
[49] M. Scheffler, P. Colombo, 'Cellular ceramics: Structure, manufacturing, properties and applications', weinheim, wiley-vch, verlag gmbh & co, Kgaa. (2005).
[50] X. Liu, Y. Huang, J. Yang, Effect of rheological properties of the suspension on the mechanical strength of Al_2O_3-ZrO_2 composites prepared by gelcasting, Ceram. Int. 28 (2002) 159–164. doi:10.1016/S0272-8842(01)00072-4.
[51] A. Demir, Fabrication of alumina ceramic filters and performance tests for aluminium castings, Acta Phys. Pol. A. 134 (2018) 332–334. doi:10.12693/APhysPolA.134.332.
[52] J.T. Richardson, Y. Peng, D. Remue, Properties of ceramic foam catalyst supports: Pressure drop, Appl. Catal. A Gen. 204 (2000) 19–32. doi:10.1016/S0926-860X(00)00508-1.
[53] S. Lopez-Orozco, A. Inayat, A. Schwab, T. Selvam, W. Schwieger, Zeolitic Materials with Hierarchical Porous Structures, Adv. Mater. 23 (2011) 2602–2615. doi:https://doi.org/10.1002/adma.201100462.
[54] E.C. Hammel, O.L.-R. Ighodaro, O.I. Okoli, Processing and properties of advanced porous ceramics: An application based review, Ceram. Int. 40 (2014) 15351–15370. doi:https://doi.org/10.1016/j.ceramint.2014.06.095.
[55] A. Tampieri, G. Celotti, S. Sprio, A. Delcogliano, S. Franzese, Porosity-graded hydroxyapatite ceramics to replace natural bone., Biomaterials. 22 (2001) 1365–1370. doi:10.1016/s0142-9612(00)00290-8.
[56] J.J. Harrigan, S.R. Reid, A. Seyed Yaghoubi, The correct analysis of shocks in a cellular material, Int. J. Impact Eng. 37 (2010) 918–927. doi:10.1016/j.ijimpeng.2009.03.011.
[57] D. Karagiozova, M. Alves, Propagation of compaction waves in cellular materials with continuously varying density, Int. J. Solids Struct. 71 (2015) 323–337. doi:10.1016/j.ijsolstr.2015.07.005.
[58] M. Aleyaasin, J.J. Harrigan, S.R. Reid, Air-blast response of cellular material with a face plate: An analytical-numerical approach, Int. J. Mech. Sci. 91 (2015) 64–70. doi:10.1016/j.ijmecsci.2014.03.027.
[59] K. Schwartzwalder, A.W. Somers, Method of Making Porous Ceramic Articles, U.S.

Pat. (1963) 4.
[60] P. Colombo, E. Bernardo, L. Biasetto, Novel Microcellular Ceramics from a Silicone Resin, J. Am. Ceram. Soc. 87 (2004) 152–154. doi:https://doi.org/10.1111/j.1551-2916.2004.00152.x.
[61] J.-M. Bouler, M. Trécant, J. Delécrin, J. Royer, N. Passuti, G. Daculsi, Macroporous biphasic calcium phosphate ceramics: Influence of five synthesis parameters on compressive strength, J. Biomed. Mater. Res. 32 (1996) 603–609. doi:https://doi.org/10.1002/(SICI)1097-4636(199612)32:4<603::AID-JBM13>3.0.CO;2-E.
[62] J. Luyten, S. Mullens, J. Cooymans, A.M. De Wilde, I. Thijs, R. Kemps, Different methods to synthesize ceramic foams, J. Eur. Ceram. Soc. 29 (2009) 829–832. doi:10.1016/j.jeurceramsoc.2008.07.039.
[63] J.A. Lewis, Binder removal from ceramics, Annu. Rev. Mater. Sci. 27 (1997) 147–173. doi:10.1146/annurev.matsci.27.1.147.
[64] G. Han, K. Gable, K. SD, F. Beaudoin, N. JA, D. TM, The Saccharomyces cerevisiae YBR159w gene encodes the 3-ketoreductase of the microsomal fatty acid elongase., J. Biol. Chem. 277 (2002) 35440–35449.
[65] T. EJ, C. SG, G. CD, R. PJ, S. JW, H. RJ, S. PF, P. GD, D. Delneri, A. MP, Fusel alcohols regulate translation initiation by inhibiting eIF2B to reduce ternary complex in a mechanism that may involve altering the integrity and dynamics of the eIF2B body., Mol. Biol. Cell. 21 (2010) 2202–2216.
[66] X. Zhu, D. Jiang, S. Tan, Improvement in the strength of reticulated porous ceramics by vacuum degassing, Mater. Lett. 51 (2001) 363–367. doi:10.1016/S0167-577X(01)00322-6.
[67] J. Saggio-Woyansky, C.E. Scott, W.P. Minnear, Processing of porous ceramics, Am. Ceram. Soc. Bull. 71 (1992) 1674–1682. https://www.tib.eu/de/suchen/id/tema%3ATEMAC93013079479.
[68] H.R. Ramay, M. Zhang, Preparation of porous hydroxyapatite scaffolds by combination of the gel-casting and polymer sponge methods, Biomaterials. 24 (2003) 3293–3302. doi:10.1016/S0142-9612(03)00171-6.
[69] D.J. Green, P. Colombo, Cellular ceramics: Intriguing structures, novel properties, and innovative applications, MRS Bull. 28 (2003) 296–300. doi:10.1557/mrs2003.84.
[70] K.S.W. Sing, Reporting physisorption data for gas/solid systems with special reference to the determination of surface area and porosity (Recommendations 1984), Pure Appl. Chem. 57 (1985) 603–619. doi:doi:10.1351/pac198557040603.
[71] X. Yao, S. Tan, Z. Huang, D. Jiang, Effect of Recoating Slurry Viscosity on the Properties of Reticulated Porous Silicon Carbide Ceramics, Ceram. Int. 32 (2006) 137–142. doi:10.1016/j.ceramint.2005.01.008.
[72] I. Sopyan, J. Kaur, Preparation and characterization of porous hydroxyapatite through polymeric sponge method, Ceram. Int. 35 (2009) 3161–3168. doi:10.1016/j.ceramint.2009.05.012.
[73] Z. Zivcová, E. Gregorová, W. Pabst, Alumina ceramics prepared with new pore-forming agents, Process. Appl. Ceram. 2 (2008) 1–8. doi:10.2298/pac0801001z.
[74] T.J. Fitzgerald, V.J. Michaud, A. Mortensen, Processing of microcellular SiC foams - Part II Ceramic foam production, J. Mater. Sci. 30 (1995) 1037–1045. doi:10.1007/BF01178442.
[75] R.A. White, J.N. Weber, E.W. White, Replamineform: a new process for preparing porous ceramic, metal, and polymer prosthetic materials., Science. 176 (1972) 922–924. doi:10.1126/science.176.4037.922.
[76] J. Luyten, I. Thijs, W. Vandermeulen, S. Mullens, B. Wallaeys, R. Mortelmans, Strong ceramic foams from polyurethane templates, Adv. Appl. Ceram. 104 (2005) 4–8.

doi:10.1179/174367605225010990.
[77] A.E.M. Paiva, P. Sepulveda, V.C. Pandolfelli, Processing and thermomechanical evaluation of fibre-reinforced alumina filters, J. Mater. Sci. 34 (1999) 2641–2649. doi:10.1023/A:1004613102358.
[78] T. Mizrah, A. Maurer, L. Gauckler, J.P. Gabathuler, Open-pore ceramic foam as diesel particulate filter, SAE Tech. Pap. (1989) 19–28. doi:10.4271/890172.
[79] X. Pu, X. Liu, F. Qiu, L. Huang, Novel method to optimize the structure of reticulated porous ceramics, J. Am. Ceram. Soc. 87 (2004) 1392–1394. doi:10.1111/j.1151-2916.2004.tb07745.x.
[80] F.F. LANGE, K.T. MILLER, Open-Cell, Low-Density Ceramics Fabricated from Reticulated Polymer Substrates, Adv. Ceram. Mater. 2 (1987) 827–831. doi:10.1111/j.1551-2916.1987.tb00156.x.
[81] S. Barg, E.G. de Moraes, D. Koch, G. Grathwohl, New cellular ceramics from high alkane phase emulsified suspensions (HAPES), J. Eur. Ceram. Soc. 29 (2009) 2439–2446. doi:10.1016/j.jeurceramsoc.2009.02.003.
[82] J.M. Tulliani, L. Montanaro, T.J. Bell, M. V. Swain, Semiclosed-cell mullite foams: Preparation and macro- and micromechanical characterization, J. Am. Ceram. Soc. 82 (1999) 961–968. doi:10.1111/j.1151-2916.1999.tb01860.x.
[83] E. Roncari, C. Galassi, C. Bassarello, Mullite suspensions for reticulate ceramic preparation, J. Am. Ceram. Soc. 83 (2000) 2993–2998. doi:10.1111/j.1151-2916.2000.tb01672.x.
[84] E. Sousa, C.B. Silveira, T. Fey, P. Greil, D. Hotza, A.P. Novaes de Oliveira, LZSA glass ceramic foams prepared by replication process, Adv. Appl. Ceram. 104 (2005) 22–29. doi:10.1179/174367605225011043.
[85] X. Liang, Y. Li, J. Liu, S. Sang, Y. Chen, B. Li, C.G. Aneziris, Fabrication of SiC reticulated porous ceramics with multi-layered struts for porous media combustion, Ceram. Int. 42 (2016) 13091–13097. doi:10.1016/j.ceramint.2016.05.093.
[86] L. Dean-Mo, J.J. Brown, Lightweight (Ca1-x, Mgx)Zr4(PO4)6 ceramics, Mater. Chem. Phys. 32 (1992) 161–167. doi:10.1016/0254-0584(92)90272-A.
[87] J. Will, Ceramic Foams as Current Collectors in Solide Oxide Fuel Cells (SOFC): Electrical Conductivity and Mechanical Behaviour, ECS Proc. Vol. 1997–40 (1997) 757–764. doi:10.1149/199740.0757pv.
[88] A. Sherman, R. Tuffias, R. Kaplan, Refractory ceramic foams : a novel, new high-temperature structure, Am. Ceram. Soc. Bull. 70 (1991) 1025–1029.
[89] Z. Liu, T. Fan, W. Zhang, D. Zhang, The synthesis of hierarchical porous iron oxide with wood templates, Microporous Mesoporous Mater. 85 (2005) 82–88. doi:10.1016/j.micromeso.2005.06.021.
[90] M. Mizutani, H. Takase, N. Adachi, T. Ota, K. Daimon, Y. Hikichi, Porous ceramics prepared by mimicking silicified wood, Sci. Technol. Adv. Mater. 6 (2005) 76–83. doi:10.1016/j.stam.2004.08.004.
[91] J. Cao, C.R. Rambo, H. Sieber, Manufacturing of microcellular, biomorphous oxide ceramics from native pine wood, Ceram. Int. 30 (2004) 1967–1970. doi:10.1016/j.ceramint.2003.12.181.
[92] J. Cao, O. Rusina, H. Sieber, Processing of porous TiO_2-ceramics from biological preforms, Ceram. Int. 30 (2004) 1971–1974. doi:10.1016/j.ceramint.2003.12.180.
[93] Biomimetic Process.Pdf, (n.d.).
[94] H. Sieber, C. Hoffmann, A. Kaindl, P. Greil, Biomorphic Cellular Ceramics, Adv. Eng. Mater. 2 (2000) 105–109. doi:10.1002/(sici)1527-2648(200003)2:3<105::aid-adem105>3.3.co;2-g.
[95] C.R. Rambo, J. Cao, O. Rusina, H. Sieber, Manufacturing of biomorphic (Si, Ti, Zr)-carbide ceramics by sol-gel processing, Carbon N. Y. 43 (2005) 1174–1183.

doi:10.1016/j.carbon.2004.12.009.
[96] J.M. Qian, J.P. Wang, Z.H. Jin, Preparation of biomorphic SiC-ceramics by the reactive infiltration of Si into carbon template derived from basswood, Xiyou Jinshu Cailiao Yu Gongcheng/Rare Met. Mater. Eng. 33 (2004) 1065–1068.
[97] F.M. Varela-Feria, J. Martínez-Fernández, A.R. De Arellano-López, M. Singh, Low density biomorphic silicon carbide: Microstructure and mechanical properties, J. Eur. Ceram. Soc. 22 (2002) 2719–2725. doi:10.1016/S0955-2219(02)00137-1.
[98] P. Greil, T. Lifka, A. Kaindl, Biomorphic cellular silicon carbide ceramics from wood: I. Processing and microstructure, J. Eur. Ceram. Soc. 18 (1998) 1961–1973. doi:10.1016/S0955-2219(98)00156-3.
[99] A. Zampieri, H. Sieber, T. Selvam, G.T.P. Mabande, W. Schwieger, F. Scheffler, M. Scheffler, P. Greil, Biomorphic cellular SiSiC/zeolite ceramic composites: From rattan palm to bioinspired structured monoliths for catalysis and sorption, Adv. Mater. 17 (2005) 344–349. doi:10.1002/adma.200400672.
[100] E. Vogli, H. Sieber, P. Greil, Biomorphic SiC-ceramic prepared by Si-vapor phase infiltration of wood, J. Eur. Ceram. Soc. 22 (2002) 2663–2668. doi:10.1016/S0955-2219(02)00131-0.
[101] C.R. Rambo, H. Sieber, Novel synthetic route to biomorphic Al_2O_3 ceramics, Adv. Mater. 17 (2005) 1088–1091. doi:10.1002/adma.200401049.
[102] N. Popovska, D.A. Streitwieser, C. Xu, H. Gerhard, Paper derived biomorphic porous titanium carbide and titanium oxide ceramics produced by chemical vapor infiltration and reaction (CVI-R), J. Eur. Ceram. Soc. 25 (2005) 829–836. doi:10.1016/j.jeurceramsoc.2004.04.007.
[103] N. Popovska, D. Almeida-Streitwieser, C. Xu, H. Gerhard, H. Sieber, Kinetic analysis of the processing of porous biomorphic titanium carbide ceramics by chemical vapor infiltration, Chem. Vap. Depos. 11 (2005) 153–158. doi:10.1002/cvde.200306319.
[104] A. Herzog, R. Klingner, U. Vogt, T. Graule, Wood-derived porous SiC ceramics by sol infiltration and carbothermal reduction, J. Am. Ceram. Soc. 87 (2004) 784–793. doi:10.1111/j.1551-2916.2004.00784.x.
[105] C. Zollfrank, R. Kladny, H. Sieber, P. Greil, Biomorphous SiOC/C-ceramic composites from chemically modified wood templates, J. Eur. Ceram. Soc. 24 (2004) 479–487. doi:10.1016/S0955-2219(03)00202-4.
[106] A. Dong, Y. Wang, Y. Tang, N. Ren, Y. Zhang, Y. Yue, Z. Gao, Zeolitic tissue through wood cell templating, Adv. Mater. 14 (2002) 926–929. doi:10.1002/1521-4095(20020618)14:12<926::AID-ADMA926>3.0.CO;2-1.
[107] L.M. Rodríguez-Lorenzo, K.A. Gross, Calcium Phosphate Porous Scaffolds from Natural Materials, Key Eng. Mater. 254–256 (2004) 957–960. doi:10.4028/www.scientific.net/kem.254-256.957.
[108] A. SAFARI, A. HALLIYAL, L.J. BOWEN, R.E. NEWNHAM, Flexible Composite Transducers, J. Am. Ceram. Soc. 65 (1982) 207–209. doi:10.1111/j.1151-2916.1982.tb10405.x.
[109] P.S. Liss, P.G. Slater, © 1974 Nature Publishing Group, (1974).
[110] J. Hu, J.J. Russell, B. Ben-Nissan, R. Vago, Production and analysis of hydroxyapatite from Australian corals via hydrothermal process, J. Mater. Sci. Lett. 20 (2001) 85–87. doi:10.1023/A:1006735319725.
[111] V.R. Salvini, B.A. Sandurkov, R.F.K. Gunnewlek, D.S. Rosa, V.C. Pandolfelli, Porous ceramics with tailored properties, Am. Ceram. Soc. Bull. 86 (2007) 9401–9405.
[112] J.H. Eom, Y.W. Kim, S. Raju, Processing and properties of macroporous silicon carbide ceramics: A review, J. Asian Ceram. Soc. 1 (2013) 220–242. doi:10.1016/j.jascer.2013.07.003.
[113] C. Gu, C. Guo, X. Dong, Z. Hu, P. Wu, Z. Su, Y. Lu, B. Xu, Z. Yu, A. Liu, Core-shell

structured iron-containing ceramic nanoparticles: Facile fabrication and excellent electromagnetic absorption properties, J. Am. Ceram. Soc. 102 (2019) 7098–7107. doi:10.1111/jace.16619.

[114] A. Imhof, D.J. Pine, Preparation of Titania Foams, Adv. Mater. 11 (1999) 311–314. doi:https://doi.org/10.1002/(SICI)1521-4095(199903)11:4<311::AID-ADMA311>3.0.CO;2-Q.

[115] Y. Hotta, P.C.A. Alberius, L. Bergström, Coated polystyrene particles as templates for ordered macroporous silica structures with controlled wall thickness, J. Mater. Chem. 13 (2003) 496–501. doi:10.1039/b208795m.

[116] S.R. Mukai, H. Nishihara, H. Tamon, Formation of monolithic silica gel microhoneycombs (SMHs) using pseudosteady state growth of microstructural ice crystals, Chem. Commun. 4 (2004) 874–875. doi:10.1039/b316597c.

[117] K. Araki, J.W. Halloran, Porous ceramic bodies with interconnected pore channels by a novel freeze casting technique, J. Am. Ceram. Soc. 88 (2005) 1108–1114. doi:10.1111/j.1551-2916.2005.00176.x.

[118] L.M. Rodríguez-Lorenzo, M. Vallet-Regí, J.M.F. Ferreira, Fabrication of porous hydroxyapatite bodies by a new direct consolidation method: Starch consolidation, J. Biomed. Mater. Res. 60 (2002) 232–240. doi:10.1002/jbm.10036.

[119] Y. Li, F. Chen, L. Li, W. Zhang, H. Yu, Y. Shan, Q. Shen, H. Jiang, Gas Pressure Sintering of Arbitrary Porous Silicon Nitride Ceramics with High Mechanical Strength, J. Am. Ceram. Soc. 93 (2010) 1565–1568. doi:https://doi.org/10.1111/j.1551-2916.2010.03603.x.

[120] A. Díaz, S. Hampshire, Characterisation of porous silicon nitride materials produced with starch, J. Eur. Ceram. Soc. 24 (2004) 413–419. doi:https://doi.org/10.1016/S0955-2219(03)00212-7.

[121] Q. Shen, F. Yan, L. Zhang, Pressureless Sintering of α-Si3N4 Porous Ceramics Using a H3PO4 Pore-forming Agent, J. Am. Ceram. Soc. 90 (2007) 2379–2383. doi:10.1111/j.1551-2916.2007.01800.x.

[122] J. Yang, G.-J. Zhang, T. Ohji, Fabrication of Low-Shrinkage, Porous Silicon Nitride Ceramics by Addition of a Small Amount of Carbon, J. Am. Ceram. Soc. 84 (2004) 1639–1641. doi:10.1111/j.1151-2916.2001.tb00890.x.

[123] Y. Hotta, Silica honeycomb-crystal structure prepared by fabrication of silica-coated particles, Mater. Sci. Forum. 439 (2003) 186–191. doi:10.4028/www.scientific.net/msf.439.186.

[124] D. Wang, R.A. Caruso, F. Caruso, Synthesis of macroporous titania and inorganic composite materials from coated colloidal spheres - A novel route to tune pore morphology, Chem. Mater. 13 (2001) 364–371. doi:10.1021/cm001184j.

[125] S.A. Davis, M. Breulmann, K.H. Rhodes, B. Zhang, S. Mann, Template-directed assembly using nanoparticle building blocks: A nanotectonic approach to organized materials, Chem. Mater. 13 (2001) 3218–3226. doi:10.1021/cm011068w.

[126] J. Luyten, S. Mullens, J. Cooymans, A.M. De Wilde, I. Thijs, New Processing Techniques of Ceramic Foams, Adv. Eng. Mater. 5 (2003) 715–718. doi:10.1002/adem.200300381.

[127] D.M. Liu, Influence of porosity and pore size on the compressive strength of porous hydroxyapatite ceramic, Ceram. Int. 23 (1997) 135–139. doi:10.1016/S0272-8842(96)00009-0.

[128] B.P. Kumar, H.H. Kumar, D.K. Kharat, Study on pore-forming agents in processing of porous piezoceramics, J. Mater. Sci. Mater. Electron. 16 (2005) 681–686. doi:10.1007/s10854-005-3746-6.

[129] Y.W. Kim, S.H. Kim, I.H. Song, H.D. Kim, C.B. Park, Fabrication of open-cell, microcellular silicon carbide ceramics by carbothermal reduction, J. Am. Ceram. Soc.

88 (2005) 2949–2951. doi:10.1111/j.1551-2916.2005.00509.x.
[130] P. Colombo, E. Bernardo, Macro- and micro-cellular porous ceramics from preceramic polymers, Compos. Sci. Technol. 63 (2003) 2353–2359. doi:10.1016/S0266-3538(03)00268-9.
[131] Y.W. Kim, S.H. Kim, H.D. Kim, C.B. Park, Processing of closed-cell silicon oxycarbide foams from a preceramic polymer, J. Mater. Sci. 39 (2004) 5647–5652. doi:10.1023/B:JMSC.0000040071.55240.85.
[132] Y.W. Kim, Y.J. Jin, Y.S. Chun, I.H. Song, H.D. Kim, A simple pressing route to closed-cell microcellular ceramics, Scr. Mater. 53 (2005) 921–925. doi:10.1016/j.scriptamat.2005.06.032.
[133] S.H. Li, J.R. De Wijn, P. Layrolle, K. De Groot, Novel method to manufacture porous hydroxyapatite by dual-phase mixing, J. Am. Ceram. Soc. 86 (2003) 65–72. doi:10.1111/j.1151-2916.2003.tb03279.x.
[134] S.H. Li, J.R. De Wijn, P. Layrolle, K. De Groot, Synthesis of macroporous hydroxyapatite scaffolds for bone tissue engineering, J. Biomed. Mater. Res. 61 (2002) 109–120. doi:10.1002/jbm.10163.
[135] J.-F. Yang, G.-J. Zhang, N. Kondo, T. Ohji, S. Kanzaki, Synthesis of Porous Si3N4 Ceramics with Rod-Shaped Pore Structure, J. Am. Ceram. Soc. 88 (2005) 1030–1032. doi:https://doi.org/10.1111/j.1551-2916.2005.00199.x.
[136] H. Wang, I. Sung, L.I. Xiaodong, D. Kim, Fabrication of porous SiC ceramics with special morphologies by sacrificing template method, J. Porous Mater. 11 (2004) 265–271. doi:10.1023/B:JOPO.0000046353.24308.86.
[137] S.A. Davis, M. Breulmann, K.H. Rhodes, B. Zhang, S. Mann, Template-Directed Assembly Using Nanoparticle Building Blocks: A Nanotectonic Approach to Organized Materials, Chem. Mater. 13 (2001) 3218–3226. doi:10.1021/cm011068w.
[138] G.J. Zhang, J.F. Yang, T. Ohji, Fabrication of Porous Ceramics with Unidirectionally Aligned Continuous Pores, J. Am. Ceram. Soc. 84 (2001) 1395–1397. doi:10.1111/j.1151-2916.2001.tb00849.x.
[139] C. Wang, T. Kasuga, M. Nogami, Macroporous calcium phosphate glass-ceramic prepared by two-step pressing technique and using sucrose as a pore former, J. Mater. Sci. Mater. Med. 16 (2005) 739–744. doi:10.1007/s10856-005-2611-8.
[140] M.H. Prado Da Silva, A.F. Lemos, I.R. Gibson, J.M.F. Ferreira, J.D. Santos, Porous glass reinforced hydroxyapatite materials produced with different organic additives, J. Non. Cryst. Solids. 304 (2002) 286–292. doi:10.1016/S0022-3093(02)01036-0.
[141] H. Katsuki, A. Kawahara, H. Ichinose, Preparation and some properties of porous alumina ceramics obtained by the gelatination of ammonium alginate, J. Mater. Sci. 27 (1992) 6067–6070. doi:10.1007/BF01133751.
[142] O. Lyckfeldt, J.M.F. Ferreira, Processing of Porous Ceramics by "Starch Consolidation," J. Eur. Ceram. Soc. 18 (1998) 131–140. doi:10.1016/s0955-2219(97)00101-5.
[143] M.E. Bowden, M.S. Rippey, Porous Ceramics Formed Using Starch Consolidation, Key Eng. Mater. 206–213 (2001) 1957–1960. doi:10.4028/www.scientific.net/KEM.206-213.1957.
[144] J. Luyten, J.F.C. Cooymans, A. De Wilde, I. Thijs, Porous Materials, Synthesis and Charaterization, Key Eng. Mater. 206–213 (2001) 1937–1940. doi:10.4028/www.scientific.net/KEM.206-213.1937.
[145] C. Galassi, C. Capiani, F. Craciun, E. Roncari, Water-based technique to produce porous PZT materials, J. Phys. IV JP. 128 (2005) 27–31. doi:10.1051/jp4:2005128005.
[146] L. Yang, X.-S. Ning, K.-X. Chen, Q.-F. Xiao, H. Zhou, Preparation of porous hydroxyapatite ceramics with starch additives, Trans. Nonferrous Met. Soc. China. 15 (2005) 257–260.

[147] R. Barea, M.I. Osendi, P. Miranzo, J.M.F. Ferreira, Fabrication of highly porous mullite materials, J. Am. Ceram. Soc. 88 (2005) 777–779. doi:10.1111/j.1551-2916.2005.00092.x.
[148] A. Díaz, S. Hampshire, Characterisation of porous silicon nitride materials produced with starch, J. Eur. Ceram. Soc. 24 (2004) 413–419. doi:10.1016/S0955-2219(03)00212-7.
[149] A.F. Lemos, J.M.F. Ferreira, Porous bioactive calcium carbonate implants processed by starch consolidation, Mater. Sci. Eng. C. 11 (2000) 35–40. doi:10.1016/S0928-4931(00)00134-X.
[150] P. V. Vasconcelos, J.A. Labrincha, J.M.F. Ferreira, Permeability of diatomite layers processed by different colloidal techniques, J. Eur. Ceram. Soc. 20 (2000) 201–207. doi:10.1016/S0955-2219(99)00139-9.
[151] H.M. Alves, G. Tarì, A.T. Fonseca, J.M.F. Ferreira, Processing of porous cordierite bodies by starch consolidation, Mater. Res. Bull. 33 (1998) 1439–1448. doi:10.1016/S0025-5408(98)00131-7.
[152] O. Lyckfeldt, E. Liden, R. [Swedish C.I. Carlsson Goeteborg (Switzerland)], Processing of thermal insulation materials with controlled porosity, in: American Ceramic Society, Westerville, OH (United States), United States, 1995. https://www.osti.gov/biblio/86599.
[153] D. Walsh, S. Mann, Synthesis of cellular inorganic films from self-organized Media, Adv. Mater. 9 (1997) 658–662. doi:https://doi.org/10.1002/adma.19970090816.
[154] A. Imhof, D.J. Pine, Ordered macroporous materials by emulsion templating, Nature. 389 (1997) 948–951. doi:10.1038/40105.
[155] A. Imhof, D.J. Pine, Preparation of titania foams, Adv. Mater. 11 (1999) 311–314. doi:10.1002/(SICI)1521-4095(199903)11:4<311::AID-ADMA311>3.0.CO;2-Q.
[156] B.P. Binks, Macroporous Silica From Solid-Stabilized Emulsion Templates, Adv. Mater. 14 (2002) 1824–1827. doi:https://doi.org/10.1002/adma.200290010.
[157] Y. Beppu, M. Ando, T. Ohji, Control of porosity and pore size for porous alumina prepared from α-alumina, BaSO4 and/or SrSO4, (2001) 209–214.
[158] E.S. Toberer, J.C. Weaver, K. Ramesha, R. Seshadri, Macroporous Monoliths of Functional Perovskite Materials through Assisted Metathesis, Chem. Mater. 16 (2004) 2194–2200. doi:10.1021/cm0303540.
[159] H. Kim, C. da Rosa, M. Boaro, J.M. Vohs, R.J. Gorte, Fabrication of Highly Porous Yttria-Stabilized Zirconia by Acid Leaching Nickel from a Nickel-Yttria-Stabilized Zirconia Cermet, J. Am. Ceram. Soc. 85 (2002) 1473–1476. doi:https://doi.org/10.1111/j.1151-2916.2002.tb00299.x.
[160] J.H. She, J.F. Yang, T. Ohji, Reaction Bonding of Porous Mullite Ceramics, Key Eng. Mater. 247 (2003) 223–226. doi:10.4028/www.scientific.net/KEM.247.223.
[161] S. Deville, E. Saiz, R.K. Nalla, A.P. Tomsia, Freezing as a path to build complex composites., Science. 311 (2006) 515–518. doi:10.1126/science.1120937.
[162] S. Deville, Freeze-Casting of Porous Ceramics: A Review of Current Achievements and Issues, Adv. Eng. Mater. 10 (2008) 155–169. doi:https://doi.org/10.1002/adem.200700270.
[163] P. Colombo, J.R. Hellmann, Ceramic foams from preceramic polymers, Mater. Res. Innov. 6 (2002) 260–272. doi:10.1007/s10019-002-0209-z.
[164] M.D.M. Innocentini, P. Sepulveda, V.R. Salvini, V.C. Pandolfelli, J.R. Coury, Permeability and structure of cellular ceramics: A comparison between two preparation techniques, J. Am. Ceram. Soc. 81 (1998) 3349–3352. doi:10.1111/j.1151-2916.1998.tb02782.x.
[165] P. Sepulveda, Gelcasting foams for porous ceramics, Am. Ceram. Soc. Bull. 76 (1997) 61–65.

[166] Y. Han, J. Choi, H.-S. Kim, H. Kim, J. Park, Control of pore and window size of ceramic foams with tri-modal pore structure: Influence of agar concentration, Mater. Lett. 110 (2013) 256–259. doi:https://doi.org/10.1016/j.matlet.2013.05.100.
[167] C.G. Aneziris, W. Schärfl, B. Ullrich, Microstructure evaluation of Al_2O_3 ceramics with Mg-PSZ- and TiO_2-additions, J. Eur. Ceram. Soc. 27 (2007) 3191–3199. doi:https://doi.org/10.1016/j.jeurceramsoc.2007.01.006.
[168] B.Y. Tay, J.R.G. Evans, M.J. Edirisinghe, Solid freeform fabrication of ceramics, Int. Mater. Rev. 48 (2003) 341–370. doi:10.1179/095066003225010263.
[169] H. Seitz, W. Rieder, S. Irsen, B. Leukers, C. Tille, Three-dimensional printing of porous ceramic scaffolds for bone tissue engineering., J. Biomed. Mater. Res. B. Appl. Biomater. 74 (2005) 782–788. doi:10.1002/jbm.b.30291.
[170] C. Deckard, SLS Patent, (1986). https://patents.google.com/patent/US4863538.
[171] J. Butt, H. Mebrahtu, H. Shirvani, Rapid prototyping by heat diffusion of metal foil and related mechanical testing, Int. J. Adv. Manuf. Technol. 84 (2016) 2357–2366. doi:10.1007/s00170-015-7882-8.
[172] A. Tsouknidas, M. Pantazopoulos, I. Katsoulis, D. Fasnakis, S. Maropoulos, N. Michailidis, Impact absorption capacity of 3D-printed components fabricated by fused deposition modelling, Mater. Des. 102 (2016) 41–44. doi:https://doi.org/10.1016/j.matdes.2016.03.154.
[173] G. McKerricher, D. Titterington, A. Shamim, A Fully Inkjet-Printed 3-D Honeycomb-Inspired Patch Antenna, IEEE Antennas Wirel. Propag. Lett. 15 (2016) 544–547.
[174] M.J. Statham, F. Hammett, B. Harris, R.G. Cooke, R.M. Jordan, A. Roche, Net-Shape Manufacture of Low-Cost Ceramic Shapes by Freeze-Gelation, J. Sol-Gel Sci. Technol. 13 (1998) 171–175. doi:10.1023/a:1008696531687.
[175] H. Yang, S. Yang, X. Chi, J.R.G. Evans, Fine ceramic lattices prepared by extrusion freeforming., J. Biomed. Mater. Res. B. Appl. Biomater. 79 (2006) 116–121. doi:10.1002/jbm.b.30520.
[176] N. Ni, S. Barg, E. Garcia-Tunon, F. MacUl Perez, M. Miranda, C. Lu, C. Mattevi, E. Saiz, Understanding Mechanical Response of Elastomeric Graphene Networks, Sci. Rep. 5 (2015) 1–14. doi:10.1038/srep13712.
[177] P. Colombo, Conventional and novel processing methods for cellular ceramics, Philos. Trans. R. Soc. A Math. Phys. Eng. Sci. 364 (2006) 109–124. doi:10.1098/rsta.2005.1683.
[178] A. Vahidifar, S.N. Khorasani, C.B. Park, H.A. Khonakdar, U. Reuter, H.E. Naguib, E. Esmizadeh, Towards the development of uniform closed cell nanocomposite foams using natural rubber containing pristine and organo-modified nanoclays, RSC Adv. 6 (2016) 53981–53990. doi:10.1039/c6ra08168a.
[179] J. Luyten, S. Mullens, J. Cooymans, A.M. De Wilde, I. Thijs, R. Kemps, Different methods to synthesize ceramic foams, J. Eur. Ceram. Soc. 29 (2009) 829–832. doi:https://doi.org/10.1016/j.jeurceramsoc.2008.07.039.
[180] J. Luyten, S. Mullens, J. Cooymans, A.-M. De Wilde, I. Thijs, New Processing Techniques of Ceramic Foams, Adv. Eng. Mater. 5 (2003) 715–718. doi:https://doi.org/10.1002/adem.200300381.
[181] S. Sharafat, N. Ghoniem, M. Sawan, A. Ying, B. Williams, Breeder foam: An innovative low porosity solid breeder material, Fusion Eng. Des. 81 A (2006) 455–460. doi:10.1016/j.fusengdes.2005.06.374.
[182] S. Dhara, P. Bhargava, A Simple Direct Casting Route to Ceramic Foams, J. Am. Ceram. Soc. 86 (2004) 1645–1650. doi:10.1111/j.1151-2916.2003.tb03534.x.
[183] S. Ahmad, M.A. Latif, H. Taib, A.F. Ismail, Short review: Ceramic foam fabrication techniques for wastewater treatment application, Adv. Mater. Res. 795 (2013) 5–8. doi:10.4028/www.scientific.net/AMR.795.5.

[184] M.F. Ashby, The properties of foams and lattices, Philos. Trans. R. Soc. A Math. Phys. Eng. Sci. 364 (2006) 15 LP – 30. http://rsta.royalsocietypublishing.org/content/364/1838/15.abstract.
[185] R. Bouix, P. Viot, J.-L. Lataillade, Polypropylene foam behaviour under dynamic loadings: Strain rate, density and microstructure effects, Int. J. Impact Eng. 36 (2009) 329–342. doi:https://doi.org/10.1016/j.ijimpeng.2007.11.007.
[186] J.L. Yu, J.R. Li, S.S. Hu, Strain-rate effect and micro-structural optimization of cellular metals, Mech. Mater. 38 (2006) 160–170. doi:10.1016/j.mechmat.2005.05.018.
[187] M. Vural, G. Ravichandran, Dynamic response and energy dissipation characteristics of balsa wood: experiment and analysis, Int. J. Solids Struct. 40 (2003) 2147–2170. doi:https://doi.org/10.1016/S0020-7683(03)00057-X.
[188] G. Subhash, Q. Liu, X.-L. Gao, Quasistatic and high strain rate uniaxial compressive response of polymeric structural foams, Int. J. Impact Eng. 32 (2006) 1113–1126. doi:https://doi.org/10.1016/j.ijimpeng.2004.11.006.
[189] M. Vural, G. Ravichandran, Dynamic response and energy dissipation characteristics of balsa wood: Experiment and analysis, Int. J. Solids Struct. 40 (2003) 2147–2170. doi:10.1016/S0020-7683(03)00057-X.
[190] S.K. Maiti, L.J. Gibson, M.F. Ashby, Deformation and energy absorption diagrams for cellular solids, Acta Metall. 32 (1984) 1963–1975. doi:https://doi.org/10.1016/0001-6160(84)90177-9.
[191] F. Zhu, L. Dong, H. Ma, C.C. Chou, K.H. Yang, International Journal of Mechanical Sciences Parameterized optimal design of a novel cellular energy absorber, Int. J. Mech. Sci. 86 (2014) 60–68. doi:10.1016/j.ijmecsci.2013.09.021.
[192] M.A.A. Muhamad Nor, L.C. Hong, Z. Arifin Ahmad, H. Md Akil, Preparation and characterization of ceramic foam produced via polymeric foam replication method, J. Mater. Process. Technol. 207 (2008) 235–239. doi:10.1016/j.jmatprotec.2007.12.099.
[193] J.Y. Zhang, Y.M. Fu, X.M. Zeng, Compressive properties of open-cell ceramic foams, Trans. Nonferrous Met. Soc. China (English Ed. 16 (2006) 78–81. doi:10.1016/S1003-6326(06)60232-X.
[194] Y.S. Han, J.B. Li, Q.M. Wei, K. Tang, The effect of sintering temperatures on alumina foam strength, Ceram. Int. 28 (2002) 755–759. doi:10.1016/S0272-8842(02)00039-1.
[195] Y.S. Han, J.B. Li, Y.J. Chen, Fabrication of bimodal porous alumina ceramics, Mater. Res. Bull. 38 (2003) 373–379. doi:10.1016/S0025-5408(02)01026-7.
[196] A. Hadi, R. Emadi, S. Baghshahi, S.H. Naghavi, Different pore size alumina foams and study of their mechanical properties DIFFERENT PORE SIZE ALUMINA FOAMS AND STUDY OF THEIR MECHANICAL PROPERTIES, (2015).
[197] S. Dhara, P. Bhargava, Influence of Slurry Characteristics on Porosity and Mechanical Properties of Alumina Foams, Int. J. Appl. Ceram. Technol. 3 (2006) 382–392. doi:https://doi.org/10.1111/j.1744-7402.2006.02098.x.
[198] K. Konopka, A. Boczkowska, K. Batorski, M. Szafran, K.J. Kurzydłowski, Microstructure and properties of novel ceramic-polymer composites, Mater. Lett. 58 (2004) 3857–3862. doi:10.1016/j.matlet.2004.07.025.
[199] J. Bauer, S. Hengsbach, I. Tesari, R. Schwaiger, O. Kraft, High-strength cellular ceramic composites with 3D microarchitecture, Proc. Natl. Acad. Sci. U. S. A. 111 (2014) 2453–2458. doi:10.1073/pnas.1315147111.
[200] P. Colombo, F. Zordan, E. Medvedovski, Ceramic-polymer composites for ballistic protection, Adv. Appl. Ceram. 105 (2006) 78–83. doi:10.1179/174367606X84440.
[201] Y. Liu, X.L. Gong, Compressive behavior and energy absorption of metal porous polymer composite with interpenetrating network structure, Trans. Nonferrous Met. Soc. China (English Ed. 16 (2006). doi:10.1016/S1003-6326(06)60229-X.
[202] D. Cree, M. Pugh, Production and characterization of a three-dimensional cellular metal-

filled ceramic composite, J. Mater. Process. Technol. 210 (2010) 1905–1917. doi:10.1016/j.jmatprotec.2010.07.002.
[203] V. Jain, R. Johnson, I. Ganesh, B.P. Saha, Y.R. Mahajan, Effect of rubber encapsulation on the comparative mechanical behaviour of ceramic honeycomb and foam, Mater. Sci. Eng. A. 347 (2003) 109–122. doi:https://doi.org/10.1016/S0921-5093(02)00587-7.
[204] M. Peroglio, L. Gremillard, J. Chevalier, L. Chazeau, C. Gauthier, T. Hamaide, Toughening of bio-ceramics scaffolds by polymer coating, 27 (2007) 2679–2685. doi:10.1016/j.jeurceramsoc.2006.10.016.
[205] FGM, Proceedings - 3rd International Symposium on Structural and Functional Gradient Materials, [FGM '94], 10-12 October 1994, Swiss Federal Institute of Technology of Lausanne, Switzerland. Ed. by B. Ilschner ..., in: B. Ilschner (Ed.), Int. Symp. Struct. Funct. Gradient Mater. FGM ; 3, 1. éd., Presses Polytechniques et Univ. Romandes; , Lausanne, Suisse, Lausanne, 1995. https://www.tib.eu/de/suchen/id/TIBKAT%3A184513049.
[206] J. Aboudi, M.-J. Pindera, S.M. Arnold, A coupled higher-order theory for functionally graded composites with partial homogenization, Compos. Eng. 5 (1995) 771–792. doi:https://doi.org/10.1016/0961-9526(95)00032-I.
[207] H. Nayeb-hashemi, P.K. Canavan, IMECE2008-66206, (2019) 1–5.
[208] I.J. Maknun, I. Katili, O. Millet, A. Hamdouni, Application of DKMQ24 shell element for twist of thin-walled beams: Comparison with Vlassov theory, Int. J. Comput. Methods Eng. Sci. Mech. 17 (2016) 391–400. doi:10.1080/15502287.2016.1231240.
[209] F. Watari, A. Yokoyama, F. Saso, M. Uo, T. Kawasaki, Fabrication and properties of functionally graded dental implant, Compos. Part B Eng. 28 (1997) 5–11. doi:https://doi.org/10.1016/S1359-8368(96)00021-2.
[210] S. Amada, Y. Ichikawa, T. Munekata, Y. Nagase, H. Shimizu, Fiber texture and mechanical graded structure of bamboo, Compos. Part B Eng. 28 (1997) 13–20. doi:https://doi.org/10.1016/S1359-8368(96)00020-0.
[211] A. Ajdari, H. Nayeb-Hashemi, P. Canavan, G. Warner, Effect of defects on elastic-plastic behavior of cellular materials, Mater. Sci. Eng. A. 487 (2008) 558–567. doi:10.1016/j.msea.2007.10.050.
[212] H.X. Zhu, S.M. Thorpe, A.H. Windle, The effect of cell irregularity on the high strain compression of 2D Voronoi honeycombs, Int. J. Solids Struct. 43 (2006) 1061–1078. doi:10.1016/j.ijsolstr.2005.05.008.
[213] H. Harders, K. Hupfer, J. Rösler, Influence of cell wall shape and density on the mechanical behaviour of 2D foam structures, Acta Mater. 53 (2005) 1335–1345. doi:10.1016/j.actamat.2004.11.025.
[214] A.-J. Wang, D.L. McDowell, Effects of defects on in-plane properties of periodic metal honeycombs, Int. J. Mech. Sci. 45 (2003) 1799–1813. doi:https://doi.org/10.1016/j.ijmecsci.2003.12.007.
[215] W. Deqing, S. Ziyuan, Effect of ceramic particles on cell size and wall thickness of aluminum foam, Mater. Sci. Eng. A. 361 (2003) 45–49. doi:10.1016/S0921-5093(03)00557-4.
[216] F. Nogata, H. Takahashi, Intelligent functionally graded material: Bamboo, Compos. Eng. 5 (1995) 743–751. doi:https://doi.org/10.1016/0961-9526(95)00037-N.
[217] J.-S. Huang, L.J. Gibson, Creep of open-cell Voronoi foams, Mater. Sci. Eng. A. 339 (2003) 220–226. doi:10.1016/S0921-5093(02)00152-1.
[218] H.X. Zhu, J.R. Hobdell, A.H. Windle, Effects of cell irregularity on the elastic properties of 2D Voronoi honeycombs, J. Mech. Phys. Solids. 49 (2001) 857–870. doi:https://doi.org/10.1016/S0022-5096(00)00046-6.
[219] E. Andrews, L. Gibson, The influence of cracks, notches and holes on the tensile strength of cellular solids, Acta Mater. - ACTA MATER. 49 (2001) 2975–2979.

doi:10.1016/S1359-6454(01)00203-8.
[220] C. Chen, T.J. Lu, N.A. Fleck, Effect of imperfections on the yielding of two-dimensional foams, J. Mech. Phys. Solids. 47 (1999) 2235–2272. doi:10.1016/S0022-5096(99)00030-7.
[221] J.L. Grenestedt, F. Bassinet, Influence of cell wall thickness variations on elastic stiffness of closed-cell cellular solids, Int. J. Mech. Sci. 42 (2000) 1327–1338. doi:https://doi.org/10.1016/S0020-7403(99)00054-5.
[222] M.J. Silva, L. Gibson, The effects of non-periodic microstructure and defects on the compressive strength of two-dimensional cellular solids, Int. J. Mech. Sci. 39 (1997) 549–563.
[223] T.P. Harrigan, R.W. Mann, Characterization of microstructural anisotropy in orthotropic materials using a second rank tensor, J. Mater. Sci. 19 (1984) 761–767. doi:10.1007/BF00540446.
[224] S. V Kanakkanatt, Mechanical Anisotropy of Open-Cell Foams, J. Cell. Plast. 9 (1973) 50–53. doi:10.1177/0021955X7300900109.
[225] A. Cunningham, Modulus anisotropy of low-density cellular plastics: an aggregate model, Polymer (Guildf). 22 (1981) 882–885. doi:https://doi.org/10.1016/0032-3861(81)90261-5.
[226] D. Feldman, Mechanics of cellular plastics, N. C. Hilyard, Ed., Macmillan, New York, 1982, 401 pp. Price: 81.95 canadian dollars, J. Polym. Sci. Polym. Lett. Ed. 20 (1982) 604–605. doi:https://doi.org/10.1002/pol.1982.130201114.
[227] A.T. Huber, L.J. Gibson, Anisotropy of foams, J. Mater. Sci. 23 (1988) 3031–3040. doi:10.1007/BF00547486.
[228] N. Triantafyllidis, M.W. Schraad, Onset of failure in aluminum honeycombs under general in-plane loading, J. Mech. Phys. Solids. 46 (1998) 1089–1124. doi:https://doi.org/10.1016/S0022-5096(97)00060-4.
[229] M.C. Shaw, T. Sata, The plastic behavior of cellular materials, Int. J. Mech. Sci. 8 (1966) 469–478. doi:https://doi.org/10.1016/0020-7403(66)90019-1.
[230] R. Parkinson, Nickel plating and electroforming: Essential industries for today and the future, Nickel Dev. Inst. (2001) 30. http://www.nickelinstitute.org/~/Media/Files/TechnicalLiterature/PlatingandElectroforming_EssentialIndustriesforTodayandtheFuture_10088_.pdf.
[231] D. Ghosh, A. Wiest, R.D. Conner, Uniaxial quasistatic and dynamic compressive response of foams made from hollow glass microspheres, J. Eur. Ceram. Soc. 36 (2016) 781–789. doi:10.1016/j.jeurceramsoc.2015.10.018.
[232] R.A. Voz, R.A. Volz, P. Park, United States Patent Office, J. Am. Soc. Nav. Eng. 39 (2009) 620–622. doi:10.1111/j.1559-3584.1927.tb04229.x.
[233] M. Avalle, G. Belingardi, R. Montanini, Characterization of polymeric structural foams under compressive impact loading by means of energy-absorption diagram, Int. J. Impact Eng. 25 (2001) 455–472. doi:https://doi.org/10.1016/S0734-743X(00)00060-9.
[234] Q.M. Li, I. Magkiriadis, J.J. Harrigan, Compressive Strain at the Onset of Densification of Cellular Solids, J. Cell. Plast. 42 (2006) 371–392. doi:10.1177/0021955X06063519.
[235] M.A. Garrido, R. Font, Pyrolysis and combustion study of flexible polyurethane foam, J. Anal. Appl. Pyrolysis. 113 (2015) 202–215. doi:10.1016/j.jaap.2014.12.017.
[236] R. Narasimman, K. Prabhakaran, Preparation of carbon foams with enhanced oxidation resistance by foaming molten sucrose using a boric acid blowing agent, Carbon N. Y. 55 (2013) 305–312. doi:10.1016/j.carbon.2012.12.068.
[237] R. Narasimman, K. Prabhakaran, Preparation of low density carbon foams by foaming molten sucrose using an aluminium nitrate blowing agent, Carbon N. Y. 50 (2012) 1999–2009. doi:10.1016/j.carbon.2011.12.058.
[238] S. Vijayan, R. Narasimman, C. Prudvi, K. Prabhakaran, Preparation of alumina foams

by the thermo-foaming of powder dispersions in molten sucrose, J. Eur. Ceram. Soc. 34 (2014) 425–433. doi:10.1016/j.jeurceramsoc.2013.08.023.
[239] S. Vijayan, P. Wilson, K. Prabhakaran, Porosity and cell size control in alumina foam preparation by thermo-foaming of powder dispersions in molten sucrose, J. Asian Ceram. Soc. 4 (2016) 344–350. doi:10.1016/j.jascer.2016.06.007.
[240] L. Gurnani, A. Mukhopadhyay, Development of Carbon Nanotube-Reinforced Ceramic Matrix Nanocomposites for Advanced Structural Applications, 2020. doi:10.1007/978-3-030-16347-1_30.
[241] M. Darder, E. Ruiz-Hitzky, Caramel-clay nanocomposites, J. Mater. Chem. 15 (2005) 3913–3918. doi:10.1039/b505958e.
[242] C. Moulis, G. Joucla, D. Harrison, E. Fabre, G. Potocki-Veronese, P. Monsan, M. Remaud-Simeon, Understanding the Polymerization Mechanism of Glycoside-Hydrolase Family 70 Glucansucrases, J. Biol. Chem. 281 (2006) 31254–31267. doi:10.1016/s0021-9258(19)84038-3.
[243] G. Rosebrock, A. Elgafy, T. Beechem, K. Lafdi, Study of the growth and motion of graphitic foam bubbles, Carbon N. Y. 43 (2005) 3075–3087. doi:10.1016/j.carbon.2005.06.044.
[244] ASTM Standard E1820, Standard Test Method for Measurement of Fracture Toughness, ASTM B. Stand. (2013) 1–54. doi:10.1520/E1820-13.Copyright.
[245] A.H. HEUER, Transformation Toughening in ZrO_2-Containing Ceramics, J. Am. Ceram. Soc. 70 (1987) 689–698. doi:10.1111/j.1151-2916.1987.tb04865.x.
[246] S. Bejugama, A.K. Pandey, Effect of Nb2O5 on sintering and mechanical properties of ceria stabilized zirconia, J. Alloys Compd. 765 (2018) 1049–1054. doi:10.1016/j.jallcom.2018.06.280.

Publications from the Present Work

Journal papers published:

1. **Vemoori Raju**, Asit Kumar Khanra "Microstructural and Mechanical Properties of Al_2O_3 and ZTA Foams Prepared by Thermo-foaming Technique" **Ceramic International,** 21 (1) 29881-29887 (2021)
2. **Vemoori Raju**, Roy Johnson, Asit Kumar Khanra, Effect of Nickel Coating on the Mechanical behaviour of Polymer Replicated Al_2O_3 Foams**, Ceramic International,** 5 (1), 6871-6877(2020).
3. **Vemoori Raju**, Roy Johnson, Asit Kumar Khanra, Preparation and comparative evolution of mechanical behaviour of Fe and Fe_eO_3 foams and their polymer composition, **Journal of Alloy and Compounds**, 750 (2018) 71-76.
4. **Vemoori Raju**, Roy Johnson, Asit Kumar Khanra, Fabrication and Properties Evaluation of Alumina-Based Open-Cell Foams, **Transaction of Indian Institute of Metal.**72(6), 1679–1682 (2019).

About the author

The author was born in Yellandu, a town in Telangana State, India on 8th August 1990. After completion of his B. Tech in Mechanical engineering in the year 2012 from Sri Raja Rajeshwari Engineering College (SRREC), Karepally, Telangana; he joined for his M. Tech in Materials Technology discipline at National Institute of Technology, Warangal (NITW), Telangana, India in the year 2013. After completing his M. Tech in 2015, the author joined the National Institute of Technology Warangal, Telangana, India, to pursue his doctoral program. The author published several papers in international journals and presented his research work at international conferences.